Multiangle multiscale characterization of seismic reflection data

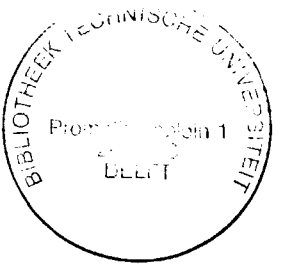

Proefschrift

ter verkrijging van de graad van doctor
aan de Technische Universiteit Delft,
op gezag van de Rector Magnificus Prof. ir. K.F. Wakker,
voorzitter van het College voor Promoties,
in het openbaar te verdedigen op maandag 3 december 2001 om 10.30 uur

door Jeroen Christiaan Martijn GOUDSWAARD

doctorandus in de geofysica
geboren te Utrecht.

Dit proefschrift is goedgekeurd door de promotoren:
Prof. dr. ir. C.P.A. Wapenaar
Prof. dr. ir. J.T. Fokkema

Samenstelling Promotiecommissie:

Rector Magnificus, voorzitter	
Prof. dr. ir. C.P.A. Wapenaar	Technische Universiteit Delft, promotor
Prof. dr. ir. J.T. Fokkema	Technische Universiteit Delft, promotor
Prof. dr. ir. P.M. van den Berg	Technische Universiteit Delft
Prof. dr. ir. F.B.J. Barends	Technische Universiteit Delft
Prof. dr. ir. A. Gisolf	Technische Universiteit Delft
Dr. F.J. Dessing	Shell Rijswijk
D. Wilkinson, Ph.D.	Chevron Corporation

ISBN 90-9015280-6

SUPPORT
The research for this thesis has been financially supported by the Dutch Science Foundation STW, grant nr. DTN 44.3547

Aan mijn ouders

Contents

Chapter 1

Introduction

This chapter provides an introduction to the seismic reflection method. Further, the use of well-logs of the velocity field, as measured in a borehole, is discussed. The notion that sharp outliers in these well-logs are consistent over lateral distance, leads to a further analysis of these outliers and their effect on seismic reflection data. Finally an outline of this thesis is given.

1.1 The seismic reflection method

The seismic reflection method is the dominant method world-wide for the exploration of oil and gas. The pioneering work was performed in earthquake studies in the mid-to-late nineteenth century. An important step was taken by Robert Mallet in 1846, who was the first to use an artificial source in a reflection experiment. A further step was taken in 1888 by August Schmidt, who devised traveltime-distance graphs for the determination of seismic velocities. Effectively, the seismic reflection method was developed. Yet it took more than 30 years, before the first seismic reflection surveys for the detection of hydrocarbons were carried out by K.C. Karcher in Oklahoma, USA (1919-1921). At the dawn of World War II however, the method had almost fully replaced all other exploration methods. Ever since, the method has been the topic of extensive studies and has been improved upon considerably, but still the basic principle remains the same: a source is ignited at or near the surface, and detectors (either geophones for land surveys or hydrophones for marine surveys) measure the Earth's response, to determine the depth, shape and nature of sub-surface layers. By the application of extensive data processing and detailed analyses of the seismic wave forms, images of the subsurface structure are developed. Further analysis of the (angle-dependent) amplitudes of a seismic event can subsequently recover some of the physi-

cal properties of the materials, like elastic moduli, anisotropy and porosity. The results of these analyses are the constraints for decisions concerning the actual development of a site.

1.2 Motivation for this research

Only after drilling an appraisal well at a certain site, detailed knowledge of the physical properties of the materials can be acquired. A commonly used property is the velocity function of the Earth as a function of depth, which can be acquired by measuring a so-called well-log of the P- and S-velocities. The local velocities can be used to distinguish between different materials. Further, as seismic reflection strength is, among others, dependent on the velocity contrast, the correlation between seismic reflection data and the well-log is useful for interpretation purposes. If this correlation is performed properly, seismic horizons away from the borehole can be matched in depth with reflecting boundaries in the well-log.

As an example, we consider a field experiment in the Nimr field in Oman [Goudswaard *et al.* (1998)]. Two boreholes were drilled, where the lateral distance between the wells was 130 m. From the recovered cores (i.e. the actual lithology), it was found that the geology was laterally continuous for the depth range of 800 to 890 m. From 860 to 890 m depth, the layers are however slightly dipping. Beyond this depth, borehole #1 reached porous oil-producing sands, where borehole #2 reached (non-producing) glacial deposits.

Fig. 1.1 shows a modified version of Fig. 8 of Goudswaard *et al.* (1998). It shows the well-logs of the P-wave velocities, as measured in both boreholes. We observe a strong correlation in the well-logs in Fig. 1.1, in the range of 800 to 890 m depth. Further, we note that the well-logs loose their correlation below 890 m depth. In Log #2, we note a stepfunction boundary at 892 m, where this boundary is not present in Log #1, which can be attributed to the change in geology mentioned earlier. Therefore, both lateral continuity and lateral discontinuity can be recovered from interpreting the well-logs.

One of the most striking features of the well-logs in Fig. 1.1 is the presence of sharp outliers in the velocity, e.g. around 840 m depth. As these outliers correlate over 130 m this can not be attributed to noise in the data. Actually, these outliers can result in strong reflections in the seismic measurements.

Intrigued by this behavior of well-logs, Herrmann (1997) applied a mul-

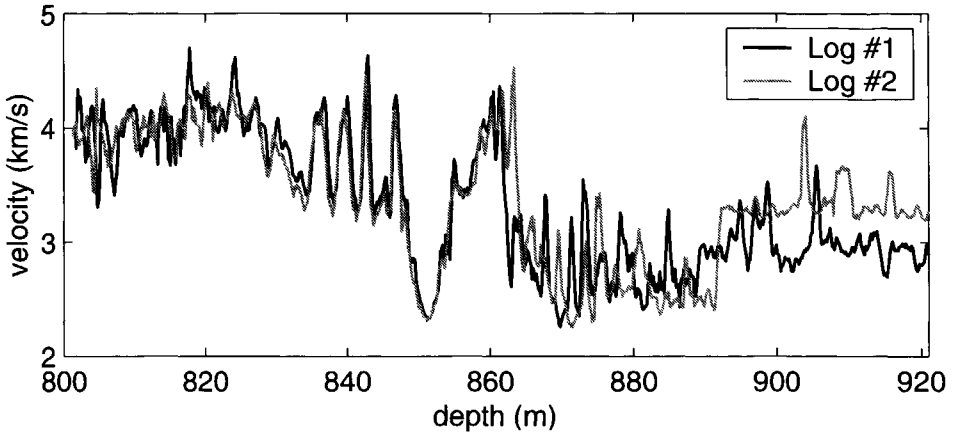

Figure 1.1: *P-wave velocity profiles for two neighboring wells in the Nimr field in Oman.*

tiscale analysis to multiple well-logs. This analysis recovered the fact that well-logs exhibit multifractal behavior over a large scale range. This behavior is characterized by a singularity parameter, that quantifies the local fractal dimension of the well-log. Accordingly, when the velocity function behaves in a multifractal way, the seismic reflection data should contain some footprint of this behavior.

This thesis is focused on the recovery of the multifractal behavior of well-logs from seismic reflection data. To this end, a simplified velocity model that accounts for the local self-simlar behavior of well-logs is given. Following, analytical expressions for the reflectivity of this model are derived. Based on this, two distinct techniques are developed to estimate the local scaling behavior of a reflector from rayparameter-dependent seismic reflection data. The thesis concludes with the analysis of two field data sets.

A topic that is not covered by this thesis is a solid physical explanation for the presence of sharp outliers in well-logs, such as in Fig. 1.1. The sharp increase or decrease of seismic velocities within several decimeters (sometimes over 1000 m/s) is difficult to reconcile with geological outcrop analyses that normally show almost homogeneous layers of several meters thickness. Throughout the years, different explanations have been proposed for these velocity fluctuations within these seemingly homogeneous layers. Voigt

(1910) and Reuss (1929) discuss that a slight change in the fractions of the rock components can drastically chang the elastic moduli of a rock. From the theory of porous rocks, I mention the influence of packing of the rock constituents on the strength properties of a rock [e.g. Mindlin (1949)]. Similarly, the presence of inclusions in the rock matrix can strongly influence the strength properties [e.g. Eshelby (1957)]. Finally, I mention the proposition of Spangenberg (1998) who discusses the influence of fractal behavior of rocks, showing that repetition of micro-structure of rocks can analytically be shown to determine the seismic velocities. The similarity of the above explanations is that only small changes in sedimentation and lithification processes can strongly influence the elastic properties of rocks. Therefore, the local scaling behavior of well-logs might be a measure of petrophysical importance, but until further research is performed, this is not known.

1.3 Outline of the thesis

Chapter 2 gives a general description of transformations as they are applied to signals. Among others, the Fourier transformation and the continuous wavelet transformation are treated. The continuous wavelet transformation is used to extract local self-similar behavior from well-logs. As a consequence of this analysis, a velocity model is presented that describes interfaces in the subsurface such that it can effectively represent the local self-similar behavior, as found in real well-logs.
Chapter 3 presents an implicit relation for the rayparameter-dependent reflectivity of the self-similar velocity functions from Chapter 2. Synthetic seismic reflection data are modeled in velocity functions, containing self-similar reflectors. Using this implicit relation, these reflection data are inverted for the singularity parameter. Further analysis of the reflection coefficient of the self-similar velocity function, gives an explicit expression for the instantaneous phase of a normal incident reflected wave. Instantaneous phase and scale dependent amplitudes of a seismic event are used to invert for both a velocity contrast ratio and the singularity parameter.
Chapter 4 presents a method that uses Linearized Zoeppritz Inversion to invert for the local seismic velocity contrasts from seismic reflection data. A multiscale analysis is used to recover, from the resulting velocity contrast functions, a singularity parameter profile. The results are compared with the singularity parameter profile that is recovered from the well-log.
Chapter 5 treats the multiscale analysis of walk-away VSP data. An imaging

approach for walk-away VSP data is given that reduces internal multiples in the final image by combining the images for all receiver depths. Both synthetic and real data examples are given. Velocity contrast functions, derived from results of conventional imaging and from the updated imaging are the input of the multiscale analysis. The correlation with the result of multiscale analysis of the velocity function is performed.

Chapter 6 gives an application of the multiscale analysis for shallow S-wave data. The singularity parameter profiles are correlated with singularity parameter profiles from CPT q_c data, which is a measurement of the strength of soil with depth. Attention is paid to the lateral continuity of the estimated singularity parameter.

Chapter 2

Transformations and multiscale analysis

Signal processing is often performed by transforming data to a different domain, after which certain aspects of the data can be better analyzed than in the domain in which they were measured. Therefore many different transformations have been proposed, each with their own advantages and disadvantages. The most common transformations are Fourier transformations, windowed Fourier transformations and wavelet transformations. This chapter gives an overview of these transformations and explains their similarities and differences. Some applications of these transformations will be treated, in which modulus maxima analysis by the wavelet transformation will receive most attention. This chapter concludes with the proposal of a generalized parameterization of reflectors in the subsurface, based on results acquired by applying the latter technique to well-logs.

2.1 Hilbert spaces

In this chapter, transformations are introduced as operations that map a function onto a different basis. Before I can introduce these transformations, a mathematical description of the space in which these transformations are valid is given.

To this end, I introduce a special form of a linear space[1]: the Hilbert space. A Hilbert space is an inner product space: a linear space in which an

[1]The linear combination of two vectors or functions in a linear space, is in the linear space as well.

inner product $\langle .,. \rangle$ is defined. The inner product satisfies the following three properties [Friedberg *et al.* (1989)]:

1. The inner product of f and g is the complex conjugate of the inner product of g and f, i. e.

$$\langle f, g \rangle = \langle g, f \rangle^*. \tag{2.1}$$

   Note that this will reduce to $\langle f, g \rangle = \langle g, f \rangle$ when the functions f and g are real.

2. The inner product is a linear operation with respect to the first argument, according to

$$\langle a_1 f_1 + a_2 f_2, g \rangle = a_1 \langle f_1, g \rangle + a_2 \langle f_2, g \rangle. \tag{2.2}$$

3. The norm of a function f is real and non-negative, according to

$$||f|| = \langle f, f \rangle^{\frac{1}{2}} \geq 0, \tag{2.3}$$

   where $\langle f, f \rangle = 0$, if and only if $f = 0$.

For an inner product space to be a Hilbert space, it is required that for any function f in the space $\langle f, f \rangle < \infty$. The second requirement for the Hilbert space is completeness; every convergent sequence (Cauchy sequence) converges to an element in the Hilbert space. The final requirement is separability; every finite dimensional Hilbert space has a countable dense subset.

The standard definition of an inner product of functions f and g in a Hilbert space is given by

$$\langle f, g \rangle = \int_{t \in \mathbb{D}_t} f(t) g^*(t) dt, \tag{2.4}$$

where $\mathbb{D}_t$ is the domain in which the functions $f(t)$ and $g(t)$ are defined. Unless otherwise stated, for functions with only real arguments, $\mathbb{D}_t$ is the set of real numbers $\mathbb{R}$ and for functions with complex arguments, $\mathbb{D}_t$ is the set of complex numbers $\mathbb{C}$. Friedberg *et al.* (1989) prove that this definition is consistent with the properties of the inner product given in eqs. (2.1)-(2.3).

Transformations are mathematical operations that map a function $f(t)$, that is defined on a basis $\{b_t\}$ to a function $\hat{f}(\xi)$ that is defined on a different basis $\{b_\xi\}$. The transformations in this chapter can be described by the inner

product of a function $f(t)$ with a transformation basis $\{b_\xi(t)\}$. The transformation basis $\{b_\xi(t)\}$ maps a function from the basis $\{b_t\}$ to a basis $\{b_\xi\}$. The general transformation operator is denoted by the symbol $\mathcal{T}$, the general transform is denoted by $\hat{f}$.

$$\begin{aligned} \{\mathcal{T}f\}(\xi) = \hat{f}(\xi) &= \langle f, b_\xi(t)\rangle \\ &= \int_{t\in\mathbb{D}_t} f(t) b_\xi^*(t) dt. \end{aligned} \tag{2.5}$$

The differences between the transformations lie in the definition of the transformation basis $\{b_\xi(t)\}$ to arrive at the desired transformation. The inverse transformation, which maps the transformed data $\hat{f}(\xi)$ back onto the original basis $\{b_t\}$ is then given by

$$\begin{aligned} \{\mathcal{T}^{-1}\hat{f}\}(t) = f(t) &= \frac{1}{S}\int_{\xi\in\mathbb{D}_\xi} \langle f, b_\xi(t)\rangle b_t(\xi) d\xi \\ &= \frac{1}{S}\int_{\xi\in\mathbb{D}_\xi} \hat{f}(\xi) b_t(\xi) d\xi, \end{aligned} \tag{2.6}$$

in which $\{b_t(\xi)\}$ is the function or vector that maps a function from the basis $\{b_\xi\}$ to a basis $\{b_t\}$. S is a normalization factor to make the transformation pair energy conserving.

2.2 The Fourier transformation

When we apply the Fourier transformation to a time-signal we arrive at its Fourier counterpart: the frequency spectrum. The physical concept of frequency spectrum is most easily appreciated with the acoustic analogon; our ears hear spectra (pitch), the brains act like an inverse Fourier transformation to arrive at the time-signal. Band-pass filtering and deconvolution are common signal processing techniques which are performed by applying Fourier transformations to the input signal and applying a filter in the Fourier domain. The need for Fourier transformations in seismic processing is therefore evident.

The Fourier transformation is a transformation that expands data on a transformation basis of complex exponentials; the prevalent convention for this transformation basis is defined by $\{b_\omega(t)\} = e^{j\omega t}$, where j is the imaginary unit, such that $j^2 = -1$. Note that the transformation basis $\{b_\omega(t)\}$ is

orthogonal, such that the transformation with respect to this basis is unique. An orthonormal transformation basis would be taking $\{b_\omega(t)\} = (2\pi)^{-\frac{1}{2}} e^{j\omega t}$. In these equations t is the time, the basis on which f is measured, and ω is the angular frequency, the basis on which F, the Fourier transform of f, is defined. Making use of eq. (2.5), we arrive at the definition of the temporal Fourier transformation $\mathcal{F}$ of a function $f(t)$

$$\begin{aligned} \{\mathcal{F}f\}(\omega) = F(\omega) &= \langle f, e^{j\omega t} \rangle \\ &= \int_{-\infty}^{\infty} f(t) e^{-j\omega t} dt. \end{aligned} \tag{2.7}$$

The inverse temporal Fourier transformation $\mathcal{F}^{-1}$ on the function $F(\omega)$ in eq. (2.7) is defined by

$$\begin{aligned} \{\mathcal{F}^{-1}F\}(t) = f(t) &= \frac{1}{2\pi} \int_{-\infty}^{\infty} \langle f, e^{j\omega t} \rangle e^{j\omega t} d\omega \\ &= \frac{1}{2\pi} \int_{-\infty}^{\infty} F(\omega) e^{j\omega t} d\omega. \end{aligned} \tag{2.8}$$

The normalization by a factor 2π makes the transformation pair energy conserving, or more explicitly: applying the inverse Fourier transformation to the Fourier transform of a function f, will result in f

$$\{\mathcal{F}^{-1}\{\mathcal{F}f\}\}(t) = f(t). \tag{2.9}$$

Equation (2.9) is generally referred to as the *Fourier integral theorem*. The definition of the Fourier transformation in eq. (2.7) requires that the functions $f(t)$ and $F(\omega)$ are contained in an appropriate Hilbert space. However, this requirement is not strong enough. For eqs. (2.7) and (2.8) to be valid, the following requirements must be met:

1. The function $f(t)$ satisfies the Dirichlet conditions on every finite interval: applying the inverse Fourier transformation to $F(\omega)$ (the Fourier transform of $f(t)$) converges to $f(t)$ at all points where $f(t)$ is continuous; at jumps it converges to the midpoint of the jump.

2. The integral over the amplitudes of $f(t)$ is finite:

$$\int_{-\infty}^{\infty} |f(t)| dt < \infty. \tag{2.10}$$

In practice, these conditions can be interpreted as follows:
As long as we have a finite registration of any time-signal $f(t)$, with finite amplitudes $|f(t)|$ everywhere, then we can compute the Fourier transform and analyze the data in the frequency domain.

2.2.1 The derivative theorem of the Fourier transformation

One important property of the Fourier transformation is introduced now, for further use in this thesis. The map of the time derivative of $f(t)$ to the Fourier domain is given by the following integration by parts

$$\begin{aligned}\left\{\mathcal{F}\frac{\partial f}{\partial t}\right\}(\omega) &= \int_{-\infty}^{\infty} \frac{\partial f(t)}{\partial t} e^{-j\omega t} dt \\ &= \left[f(t)e^{-j\omega t}\right]_{-\infty}^{\infty} + j\omega \int_{-\infty}^{\infty} f(t)e^{-j\omega t} dt. \end{aligned} \tag{2.11}$$

Due to the requirement on $f(t)$ expressed by eq. (2.10) $\lim_{t\to\pm\infty} f(t) = 0$, therefore eq. (2.11) reduces to

$$\left\{\mathcal{F}\frac{\partial f}{\partial t}\right\}(\omega) = j\omega F(\omega). \tag{2.12}$$

Equation (2.11) shows that differentiation in the time domain is equivalent to multiplication with $j\omega$ in the frequency domain. Some authors refer to this identity as the 'derivative theorem' of the Fourier transformation. This identity is used e.g. in Fourier transforming the time-domain wave equation.

2.2.2 Fourier transform of real-valued functions

Another important result can be found by noting that every function $f(t)$ can be written into an even and an odd part, according to

$$f(t) = f_e(t) + f_o(t) = \overbrace{\frac{1}{2}\left[f(t) + f(-t)\right]}^{\text{even}} + \overbrace{\frac{1}{2}\left[f(t) - f(-t)\right]}^{\text{odd}}. \tag{2.13}$$

Obviously, its Fourier transform $F(\omega)$ can be written in an even and an odd part, in the same way

$$F(\omega) = F_e(\omega) + F_o(\omega) = \frac{1}{2}[F(\omega) + F(-\omega)] + \frac{1}{2}[F(\omega) - F(-\omega)]. \quad (2.14)$$

We now write the Fourier transform as

$$F(\omega) = \int_{-\infty}^{\infty} f(t)(\cos\omega t - j\sin\omega t)dt \quad (2.15)$$

We note that the cosine is an even function and the sine an odd function. This means that for real-valued functions $f(t)$, $F_e(\omega)$ is real valued and $F_o(\omega)$ is imaginary valued. Further, the following relation for the Fourier spectrum holds

$$F(\omega) = F^*(-\omega). \quad (2.16)$$

Using the fact that the Fourier transformation and its inverse are symmetrical operators in the t and ω-domain, respectively, we can write [e.g. Fokkema and Van den Berg (1993)]

$$f_e(t) = \frac{1}{\pi}\int_0^{\infty} \chi(\omega)F_e(\omega)\cos\omega t d\omega \quad (2.17)$$

$$f_o(t) = \frac{1}{\pi}\int_0^{\infty} \chi(\omega)F_o(\omega)j\sin\omega t d\omega, \quad (2.18)$$

where $\chi(\omega)$ is the Heaviside stepfunction, defined as

$$\chi(\omega) = \begin{cases} 0 & \text{for} \quad \omega < 0 \\ \frac{1}{2} & \text{for} \quad \omega = 0 \\ 1 & \text{for} \quad \omega > 0. \end{cases} \quad (2.19)$$

Summing eqs. (2.17) and (2.18) yields

$$f(t) = \frac{1}{\pi}\Re\left[\int_0^{\infty} \chi(\omega)F(\omega)e^{j\omega t}d\omega\right]. \quad (2.20)$$

Equation (2.20) shows that for real-valued functions $f(t)$, the spectrum $F(\omega)$ for $\omega \geq 0$ is sufficient to reconstruct the full signal $f(t)$.

2.2.3 The spatial Fourier transformation

For signals that are space and time dependent, a spatial Fourier transformation is defined. The spatial Fourier transformation with respect to all spatial coordinates $\boldsymbol{x}$ is given by

$$\{\mathcal{F}f\}(\boldsymbol{k},t) = \tilde{f}(\boldsymbol{k},t) = \int_{\boldsymbol{k}\in\mathbb{D}_{\boldsymbol{x}}} f(\boldsymbol{x},t)e^{j\boldsymbol{k}\cdot\boldsymbol{x}}d\boldsymbol{x}. \tag{2.21}$$

Hence, the inverse spatial Fourier transformation is given by

$$\{\mathcal{F}^{-1}\tilde{f}\}(\boldsymbol{x},t) = f(\boldsymbol{x},t) = (2\pi)^{-N}\int_{\boldsymbol{k}\in\mathbb{D}_{\boldsymbol{k}}} \tilde{f}(\boldsymbol{k},t)e^{-j\boldsymbol{k}\cdot\boldsymbol{x}}d\boldsymbol{k}, \tag{2.22}$$

where N is the number of spatial coordinates. A full mathematical treatment of the Fourier transformations and its properties is given by Sneddon (1951).

2.2.4 The Hilbert transformation

Section 2.2 has shown that for real-valued signals $f(t)$ special properties for the Fourier transformation can be acquired. Measurements of seismic reflection data (in the time domain) are always real-valued and causal (no arrivals before time t_0, the time of source detonation). I will therefore take any function $f(t)$ to be real-valued and causal in the remainder of this section.

However, in signal processing it is often advantageous to define a complex signal $z(t)$ that relates to the real-valued signal $f(t)$ in the following way

$$\begin{aligned} z(t) &= f(t) + jg(t) \\ &= a(t)e^{j\theta(t)} \\ &= a(t)\cos\theta(t) + ja(t)\sin\theta(t). \end{aligned} \tag{2.23}$$

In the above representation there are infinite numbers of ways to define a complex signal $z(t)$ for which $a(t)\cos\theta(t) = f(t)$.

To give this representation significance, Gabor (1946) introduced the analytic signal $f_a(t)$. The analytic signal $f_a(t)$ is a complex signal which has a spectrum identical to twice the spectrum of the signal $f(t)$ for the positive frequencies and which is zero for the negative frequencies. With reference to eq. (2.20) in Subsection 2.2.2, the analytical signal is described by

$$f_a(t) = \frac{1}{\pi}\int_0^{\infty} \chi(\omega)F(\omega)e^{j\omega t}d\omega. \tag{2.24}$$

With the above definition of the analytic signal the following relation can be derived [Bracewell (2000)]

$$f_a(t) = f(t) + j\,\{\mathcal{H}f\}(t). \tag{2.25}$$

In eq. (2.25) the Hilbert transformation, denoted by $\{\mathcal{H}\ .\}$, is used to write the imaginary part of the analytic signal $f_a(t)$. The Hilbert transform of a function $f(t)$ is given by the inner product with the transformation basis $\{[\pi(t'-t)]^{-1}\}$, according to

$$\begin{aligned} \{\mathcal{H}f\}(t) &= \langle f, \frac{1}{\pi(t-t')}\rangle \\ &= \frac{1}{\pi}\int_{-\infty}^{\infty} \frac{f(t')}{t-t'}dt'. \end{aligned} \tag{2.26}$$

In the integral in eq. (2.26), at $t' = t$ the Cauchy principal value [see e.g. Butkov (1968)] is taken.

The Hilbert transformation is a type of filtering that passes the amplitudes of the spectral components of the signal unchanged, but it alters the phase

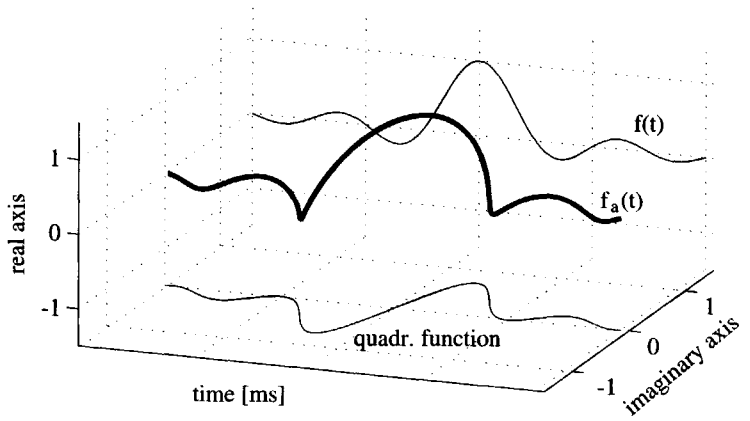

Figure 2.1: *The analytic signal $f_a(t)$, cf. eq. (2.25), the real signal $f(t)$ and the quadrature function related to $f(t)$. The quadrature function is constructed from $f(t)$ by its Hilbert transformation.*

of the signal by $-\pi/2$ (-90°) for the positive frequencies and with $\pi/2$ for the negative frequencies. However, the Hilbert transformation is better known for its application in complex signal analysis.

Figure 2.1 shows an example of the analytic signal $f_a(t)$ and the relation with the real signal $f(t)$. It shows that the projection of $f_a(t)$ on the plane defined by the axis of real numbers and the time axis represents the real signal $f(t)$; the projection of $f_a(t)$ on the plane defined by the axis of imaginary numbers and the time axis represents the Hilbert transform of $f(t)$, in most literature referred to as the *quadrature function*. An important application of the analytical signal $f_a(t)$ in eq. (2.25) is the construction of the *envelope* of a time-signal. The envelope is defined as the absolute value of $f_a(t)$. The envelope has the special property that it presents the square-root of the energy distribution in a signal. Figure 2.2 shows an example.

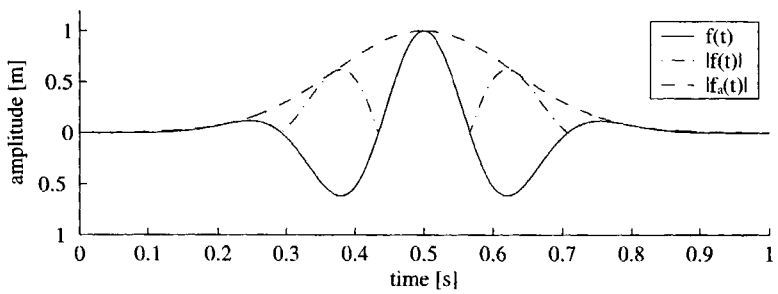

Figure 2.2: *The connection between the signal $f(t)$ and its envelope $|f_a(t)|$. The time signal $f(t)$ is represented by the solid line, the absolute value of the time signal $|f(t)|$ by the dash-dotted line and the envelope $|f_a(t)|$ by the dashed line. Note that $|f_a(t)|$ envelopes also the absolute value of the signal.*

For a more rigorous treatment of the Hilbert transformation and the background of the quadrature function, see Bracewell (2000). Many applications of the Hilbert transformation in exploration geophysics are given by Dobrin and Savit (1988)

In Chapter 3, Section 3.6 the Hilbert transformation is used to extract the instantaneous phase of an event in a seismic trace. In Section 2.3, a more practical representation of the Hilbert transformation will be introduced in terms of a convolution.

2.2.5 The linear Radon transformation

In this subsection, we assume that $u(x,t)$ is a measurement of a seismic wave field along the x-axis, where the source is a line-source stretching along the y-axis. Further we assume that the medium parameters are a function of the z-coordinate only, such that the measurement of the wave field is only dependent on the offset between the source and receivers. Due to these assumptions, the more general concept of the linear Radon transformation can be introduced as a method for the decomposition of $u(x,t)$ into plane waves. The plane waves are described in the rayparameter-intercept time (p,τ) domain, or Radon domain. Note that at any point where 'rayparameter' is used, we refer to the horizontal rayparameter, unless otherwise stated.

The linear Radon transformation is defined as the inner product of the function $U(x,\omega)$ (the temporal Fourier transform of $u(x,t)$) with the transformation basis $\{e^{-j\omega px}\}$, according to

$$\begin{aligned} \{\mathcal{R}U\}(p,\omega) = \tilde{U}(p,\omega) &= \langle U, e^{-j\omega px}\rangle \\ &= \int_{-\infty}^{\infty} U(x,\omega)e^{j\omega px}dx. \end{aligned} \tag{2.27}$$

Equivalently, in the time domain, the linear Radon transformation is given by

$$\begin{aligned} \tilde{u}(p,\tau) &= \int_{t=-\infty}^{\infty}\int_{x=-\infty}^{\infty} u(x,t)\delta(t-\tau-px)dxdt \\ &= \int_{-\infty}^{\infty} u(x,t=\tau+px)dx. \end{aligned} \tag{2.28}$$

Equation (2.28) can be interpreted as stacking along slanted lines, where p is the slope of the slanted line and τ is the intercept with the time axis [Schultz and Claerbout (1978)]. The rayparameter p is a measure for the direction of propagation of a plane wave and is defined as

$$p = \frac{\sin\theta(z)}{c(z)}. \tag{2.29}$$

Note that both the local angle of incidence $\theta(z)$ of the plane wave and the velocity $c(z)$ can change with depth z, whereas the rayparameter p is constant

for each plane wave, for all depths. Further, a plane wave has the convenient property that it does not exhibit geometrical spreading. This simplifies the analysis of the rayparameter-dependent characteristics of data, compared to a direct analysis in the space-time domain.

2.3 Convolution and deconvolution

In Section 2.2, the Fourier transformation is introduced as an important tool in signal processing. In this subsection I will introduce the process of convolution and the use of the Fourier transformation in this process.

According to Sheriff (1984), the definition of convolution as used in exploration geophysics is *"the change in wave shape as a result of passing through a linear filter"*. Suppose we have a signal $f(t)$ and a filter $g(t)$, then the resulting signal $h(t)$, which we call the convolutional product, is given by

$$h(t) = \int_{-\infty}^{\infty} f(\tau)g(t-\tau)d\tau, \tag{2.30}$$

or in shorthand notation,

$$h(t) = g(t) * f(t), \tag{2.31}$$

in which $*$ denotes 'convolution'. A more useful representation of the convolution operation can be acquired in the Fourier domain. Making use of eq. (2.7), eq. (2.30) can be rewritten as

$$\begin{aligned} H(\omega) &= \int_{t=-\infty}^{\infty} \left[\int_{\tau=-\infty}^{\infty} f(\tau)g(t-\tau)d\tau \right] e^{-j\omega t}dt \\ &= \int_{\tau=-\infty}^{\infty} f(\tau) \left[\int_{t=-\infty}^{\infty} g(t-\tau)e^{-j\omega t}dt \right] d\tau. \end{aligned} \tag{2.32}$$

Now perform the change of variables $t - \tau = u$ and $dt = du$, to arrive at

$$\begin{aligned} (2.32) &= \int_{\tau=-\infty}^{\infty} f(\tau) \left[\int_{u=-\infty}^{\infty} g(u)e^{-j\omega(u+\tau)}du \right] d\tau \\ &= \int_{\tau=-\infty}^{\infty} f(\tau)e^{-j\omega\tau}d\tau \int_{u=-\infty}^{\infty} g(u)e^{-j\omega u}du. \end{aligned} \tag{2.33}$$

Again making use of eq. (2.7) this simplifies to

$$H(\omega) = F(\omega)G(\omega). \tag{2.34}$$

Equation (2.34) shows that the convolution of two functions in the time-domain is equivalent to the multiplication of the two functions in the frequency domain. This result is generally known as the *'convolution theorem'*.

It is to noted that convolution is a linear operation, which can be checked by inspecting eq. (2.34). Convolution is frequently used in geophysical practice. One example is the computation of the Hilbert transformation in eq. (2.26) by means of a convolution, referring to Bracewell (2000)

$$\{\mathcal{H}f\}(t) = \frac{1}{\pi t} * f(t), \tag{2.35}$$

which transforms to the frequency domain as

$$\{\mathcal{F}\{\mathcal{H}f\}\}(\omega) = -j\,\mathrm{sgn}(\omega)\,F(\omega). \tag{2.36}$$

From eq. (2.36) we can see that the Hilbert transformation changes the phase of the signal by a factor $-j\,\mathrm{sgn}(\omega)$, but leaves the amplitudes intact.

Another example of the use of convolution in geophysics is the *'convolutional model'*, in which seismic data is supposed to consist of the convolution of the impulse response of an Earth model (normally defined in terms of wave velocity and density) with the wave field, measured directly at the source position (normally referred to as the 'seismic wavelet')

$$d(t) = r(t) * s(t), \tag{2.37}$$

in which $d(t)$ is the seismic data, $r(t)$ is the impulse response and $s(t)$ is the seismic wavelet. This model is used to compute the synthetic reflection and transmission data in this thesis.

Referring to eq. (2.37), the seismic wavelet can be seen as a filter that acts on the impulse response $r(t)$. The reconstruction of $r(t)$ from the data is possible by finding the inverse of the seismic wavelet $s(t)$ and convolving it with the data $d(t)$. This process is usually referred to as inverse filtering or 'deconvolution'. By measuring the wave field near the source, or by performing a (statistic) inversion on the data, an estimate of the seismic wavelet $s(t)$ can be acquired. If we define the inverse of the seismic wavelet $s^{\mathrm{inv}}(t)$ by

$$s^{\mathrm{inv}}(t) = \left\{\mathcal{F}^{-1}\frac{1}{S}\right\}(t), \tag{2.38}$$

then deconvolution is given by

$$r(t) = d(t) * s^{\text{inv}}(t), \tag{2.39}$$

or in the frequency domain

$$R(\omega) = D(\omega)/S(\omega). \tag{2.40}$$

From eq. (2.40) it is obvious that $R(\omega)$ can only be constructed inside $\Omega_\omega = \{\omega \in \mathbb{R} | S(\omega) \neq 0\}$. If we try to construct $R(\omega)$ outside Ω_ω, we create an unstable filtering procedure [Hatton *et al.* (1986)].

The discussion above shows that an exact inverse seismic wavelet can not be constructed. Therefore deconvolution is normally performed by stabilizing the frequency-domain division in eq. (2.40), according to

$$R_{\text{est}}(\omega) = \frac{D(\omega)S^*(\omega)}{|S(\omega)|^2 + \epsilon(\omega)}. \tag{2.41}$$

In this equation $R_{\text{est}}(\omega)$ is introduced, a band-limited estimate of $R(\omega)$. The factor $\epsilon(\omega)$ stabilizes the division, and may be chosen independent of the frequency ω. Note that if the factor $\epsilon(\omega) \neq 0$ for all frequencies, the reflectivity $R_{\text{est}}(\omega)$ within Ω_ω is not perfectly recovered anymore.

2.3.1 Acquiring an estimate of the seismic wavelet

There are two distinct methods for acquiring an estimate of the seismic wavelet. We can either directly measure the seismic wavelet near the source or we can try to recover it from the seismic data itself. The first method clearly has the preference, as there are no conditions on the subsurface to be met, below the point where the incident wave field detector is placed. Two examples of this kind of measurement are the placement of a hydrophone at a certain depth below an airgun array, normally at around 100m, to measure the far field response of the array. The second example can be found in land vibrator data, in which from base plate and reaction mass motion, an estimate of the full incident wave field can be acquired. Only with the explosive source on land, there is the problem that the incident wave field is hard to measure directly, because of the difficulty of placing a receiver at a depth, which would require drilling a borehole for every shotpoint.

In this situation, the assumption is made that the Earth's response is white, random and stationary, such that a deconvolution based on a minimum energy criterion can be applied to the data [e.g. Peacock and Treitel

(1969), Ziolkowski (1984)]. The stabilized division of the data by the deconvolved data is then the estimate of the seismic wavelet. It should be noted that the Earth's response is neither stationary, because of spherical divergence and attenuation, nor purely random, because it is actually the non-randomness for which we are searching in seismic exploration. The above problems will be the main sources of errors in the estimate of the seismic wavelet, together with the influence of noise, therefore we should give the preference to the direct measurement of the incident wave field.

2.4 The windowed Fourier transformation

In Cohen (1995), an adaptation of the Fourier transformation is treated that extracts local information from a signal $f(t)$. This adaption is the *time-windowed Fourier transformation*, in which the signal $f(t)$ is multiplied by the complex conjugate of a compactly supported time-window $w(t-t')$, centered around a fixed time t', according to

$$f_w(t,t') = f(t)w^*(t-t'). \tag{2.42}$$

The effect of of the multiplication with the window $w^*(t-t')$ is that in the Fourier transform of $f_w(t,t')$, we look at only a small portion of the signal $f(t)$. The appropriate transformation basis for the time-windowed Fourier transformation is therefore given by

$$\{b_{\omega,t'}(t)\} = w(t-t')e^{j\omega t}. \tag{2.43}$$

The time-windowed Fourier transformation is then the expansion of $f(t)$ with respect to this transformation basis

$$\begin{aligned} \{\mathcal{F}_w f\}(\omega,t') = F_w(\omega,t') &= \langle f, b_{\omega,t'}\rangle \\ &= \int_{-\infty}^{\infty} f(t)w^*(t-t')e^{-j\omega t}dt. \end{aligned} \tag{2.44}$$

Except for the function $w^*(t-t')$, the right hand side of eq. (2.44) is equivalent to the Fourier transformation [eq. (2.7)]. The time-windowed Fourier transform contains therefore the local spectrum of $f(t)$ around time t'. This property is of interest in many applications as seismic characterization and speech recognition of separate words; essentially any process in which we are interested in the spectral properties around a specific time.

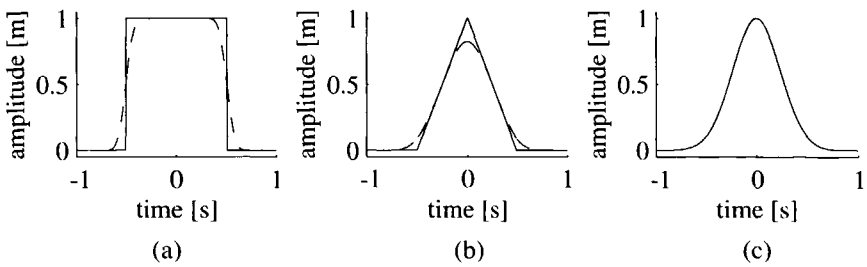

Figure 2.3: *(a) Boxcar window (solid), smoothed boxcar window (dashed) (b) Triangle window (solid), smoothed triangle window (dashed) (c) Gaussian window*

The real part of the complex window function $w(t')$ is chosen to be strictly positive. A popular choice in signal analysis for the window function is a Gaussian

$$\gamma(t,t') = \frac{1}{2\sqrt{\pi}} e^{-(\frac{t-t'}{2})^2}. \tag{2.45}$$

Note that a Gaussian is not strictly time-limited, because $\gamma(t,t') > 0$ everywhere. However, the fact that it falls off rapidly when $|t-t'|$ becomes large makes it useful as a window function. Other window functions that are in use are boxcar and triangle functions, which may be smoothed to prevent edge effects. Figure 2.3 shows some examples of commonly used window functions. Because the window function $w(t-t')$ has compact support, the reconstruction of the time-signal $f(t)$ from its time-windowed Fourier transform is only possible in the time-range $\Omega_t = \{t \in \mathbb{R} | w(t-t')| > 0\}$. Outside this region, no information on $f(t)$ is transferred to the Fourier domain, so it can not be constructed from $F_w(\omega, t')$. Therefore the inverse Fourier transform of $F_w(\omega, t')$ is only equivalent to the inverse Fourier transform of $F(t)$ within Ω_t (and 0 outside Ω_t) and given by

$$\{\mathcal{F}^{-1} F_w\}(t,t') = f_w(t,t') = \frac{1}{2\pi} \int_{-\infty}^{\infty} F_w(\omega, t') e^{j\omega t} d\omega. \tag{2.46}$$

This section has treated a transformation that can be used to perform a localized time-frequency analysis. The disadvantage of the method is that the frequency content of the analysis is fixed, because the shape and position of the window function is fixed. Within the Gabor transform [Gabor (1946)],

in which the position of the window is varied, some of these disadvantages can be solved. However, in the next section a time-frequency transformation is introduced, that analyzes frequency content and time dependency simultaneously such that all of these disadvantages are resolved.

2.5 The Continuous Wavelet Transformation

Wavelets, as a tool for time-frequency analysis of seismic data, were introduced in the beginning of the nineteen-eighties by Morlet *et al.* (1982). Wavelets are defined as square-integrable non-zero functions $\vartheta(t)$ satisfying the *admissibility property*

$$\int_{-\infty}^{\infty} \vartheta(t)dt = 0. \tag{2.47}$$

The non-zero condition imposed on $\vartheta(t)$ in eq. (2.47) implies that $\vartheta(t)$ must have at least one sign change on its domain. Furthermore it has to decay to 0 as t tends to $\pm\infty$, which shows the resemblance with the window function $w(t)$ in Section 2.4. The name 'wavelet' comes from the fact that many wavelets used in the wavelet transformation resemble seismic wavelets. Further we demand that the wavelet is normalized according to

$$||\vartheta(t)|| = 1. \tag{2.48}$$

The need for this normalization will become clear in the remainder of this section.

The motive for the development of the wavelet transformation is written down accurately by Goupillaud *et al.* (1984). Quoting them, there was a need for:

" ... a method of acquisition, transformation and recording of a seismic trace (i. e. a function of one variable, the time), so as to satisfy the requirements listed below:

1. The contributions of different frequency bands (i. e. of the different intervals of the Fourier conjugate variable) are kept reasonably separated.

2. This separation is achieved without excessive loss of resolution in the time variable (subject, of course, to the limitation of the uncertainty principle).

3. The reconstruction of the original function from its "representation" or "transform" is obtained by a method which is (a) capable of giving arbitrary high precision; (b) is robust, in the sense of being stable under small perturbations."

In this enumeration, the first two are specifying the property of time-frequency localization, already addressed by the windowed Fourier transformations in Section 2.4. However, the versatility of these transformations is limited, as the windows are always of constant shape, which will fix either the time or the frequency content of the transform. The largest problem lies in the third demand on the transformation: as has been shown, a reconstruction of the original function can not be acquired from the windowed Fourier transform. To attack this problem, the following definition of the continuous wavelet transformation is used: it is an expansion of the signal $f(t')$ on the transformation basis

$$\{b_{\sigma,t}(t')\} = \vartheta_{\sigma,t}(t') = \frac{1}{\sigma^{\mu}}\vartheta\left(\frac{t'-t}{\sigma}\right), \quad \sigma > 0, \tag{2.49}$$

where $\sigma^{-\mu}$ normalizes the wavelet basis. The function $\vartheta(t)$ is generally referred to as the 'mother wavelet'. The mother wavelet is the generating function for the analyzing wavelets $\vartheta_{\sigma,t}(t')$. The continuous wavelet transformation is now given by the following inner product

$$\begin{aligned} \{\mathcal{W}_{\vartheta} f\}(\sigma,t) = \check{f}(\sigma,t) &= \langle f, \vartheta_{\sigma,t}\rangle \\ &= \frac{1}{\sigma^{\mu}} \int_{-\infty}^{\infty} f(t')\vartheta^{*}\left(\frac{t'-t}{\sigma}\right)dt'. \end{aligned} \tag{2.50}$$

This wavelet transformation is called the *continuous* wavelet transformation because the parameters t and σ can continuously vary over $\mathbb{R}$ and $\mathbb{R}^{+}$ (i.e. the set of positive real numbers), respectively.

In computer implementations every transformation is discrete, however in Daubechies (1992) a *discrete* wavelet transformation is separately developed. It is shown that many aspects of this discrete wavelet transformation are different from the continuous wavelet transformation. Van Spaendonck (2002) applies this transformation to seismic reflection data to extract

wavelet based volume attributes. As it is beyond the scope of this thesis, no further expatiation will be made on this discrete wavelet transform.

Although the wavelet transformations in this thesis are computed for discrete values of σ only, we assume that the implicit interpolation of the wavelet transform of a signal along the σ-axis is a sufficient approximation for the following analytical expressions to hold.

The difference between the wavelet transformation and the windowed Fourier transformation lies in the shape of the generating functions of the bases $\{b_{\sigma,t}(t')\}$ and $\{b_{\omega,t}(t')\}$. The transformation basis $\{b_{\omega,t}(t')\}$ consists of functions of constant shape $w(t)$ translated to the proper time-location t'. The transformation basis $\{b_{\sigma,t}(t')\}$ consists of wavelets $\vartheta_{\sigma,t}(t')$ that are translated to the time-location t' and whose temporal bandwidth is adapted to the frequency range of interest by the scale σ. High frequency wavelets $\vartheta_{\sigma,t}(t')$ are narrow, whereas low frequency wavelets $\vartheta_{\sigma,t}(t')$ are broad. As a result, the continuous wavelet transformation is better able to "zoom in" than the time-windowed Fourier transformation on short-time, high-frequency phenomena, as pulses in signals, or singularities in functions. This property is used in this thesis to zoom in on specific reflectors in well-logs and reflections in seismic reflection data.

Contrary to what is possible with the windowed Fourier transformation, the original signal $f(t)$ can be completely reconstructed from its wavelet-transform. For this purpose, we need an expression for the inverse continuous wavelet transformation, similar to the inverse Fourier transformation in eq. (2.8). The inverse wavelet transformation is computed with the factor μ of the wavelet basis in eq. (2.49) chosen at $\mu = \frac{1}{2}$, because only then the wavelets are normalized according to $\|\vartheta_{\sigma,t}\| = \|\vartheta\| = 1$ for all σ. Only then the wavelet transformation is an *isometry*, an energy preserving transformation (up to a proportionality constant) [Kumar and Foufoula-Georgiou (1994)]. We can construct the original signal $f(t)$ from its wavelet transform, according to

$$\begin{aligned} \{\mathcal{W}_\vartheta^{-1}\check{f}\}(t) = f(t) &= \frac{1}{C_\vartheta} \int_{t'=-\infty}^{\infty} \int_{\sigma=0}^{\infty} \langle f, \vartheta_{\sigma,t'} \rangle \vartheta_t \frac{d\sigma\ dt'}{\sigma^2} \\ &= \frac{1}{C_\vartheta} \int_{t'=-\infty}^{\infty} \int_{\sigma=0}^{\infty} \check{f}(\sigma,t')\ \sigma^{-\frac{1}{2}} \vartheta\left(\frac{t-t'}{\sigma}\right) \frac{d\sigma\ dt'}{\sigma^2} \end{aligned} \quad (2.51)$$

Equation (2.51) can be shown to be correct by analyzing the following inte-

gral

$$\int_{t'=-\infty}^{\infty}\int_{\sigma=0}^{\infty} \check{f}(\sigma,t')\check{g}^*(\sigma,t')\frac{d\sigma\ dt'}{\sigma^2}$$

$$= \int_{t'=-\infty}^{\infty}\int_{\sigma=0}^{\infty}\left\{\left[\int_{\omega=-\infty}^{\infty} F(\omega)\sigma^{1/2}\Theta^*(\sigma\omega)e^{-j\omega t'}d\omega\right]\right.$$

$$\left.\left[\int_{\omega'=-\infty}^{\infty} G^*(\omega')\sigma^{1/2}\Theta(\sigma\omega')e^{j\omega' t'}d\omega'\right]\right\}\frac{d\sigma\ dt'}{\sigma^2} \quad (2.52)$$

The expression between the first pair of brackets can be seen as the inverse Fourier transform of $F_\sigma(\omega) = \sigma^{1/2}F(\omega)\Theta^*(\sigma\omega)$. The second has a similar interpretation as the complex conjugate of the inverse Fourier transform of $G_\sigma(\omega) = \sigma^{1/2}G(\omega)\Theta^*(\sigma\omega)$. Hence, applying Parseval's theorem, we can write

$$(2.52) = \frac{1}{2\pi}\int_{\sigma=0}^{\infty}\left[\int_{\omega=-\infty}^{\infty} F_\sigma(\omega)G_\sigma^*(\omega)d\omega\right]\frac{d\sigma}{\sigma^2}$$

$$= \frac{1}{2\pi}\int_{\sigma=0}^{\infty}\left[\int_{\omega=-\infty}^{\infty} F(\omega)G^*(\omega)|\Theta(\sigma\omega)|^2 d\omega\right]\frac{d\sigma}{\sigma}$$

$$= \frac{1}{2\pi}\int_{\omega=-\infty}^{\infty}\left[\int_{\sigma=0}^{\infty} |\Theta(\sigma\omega)|^2\frac{d\sigma}{\sigma}\right]F(\omega)G^*(\omega)d\omega. \quad (2.53)$$

Making the change of variables $\omega' = \sigma\omega$, and again applying Parseval's theorem, leads to

$$(2.53) = C_\vartheta\langle f, g\rangle, \quad (2.54)$$

where C_ϑ is given by

$$C_\vartheta = \int_0^{\infty}\frac{|\Theta(\omega')|^2}{|\omega'|}d\omega'. \quad (2.55)$$

Now, substituting $\check{g}$ by $\vartheta_{\sigma,t'}$ in both eqs. (2.52) and (2.54), proves the correctness of the definition of the inverse continuous wavelet transformation.

2.6 Applications of the Wavelet Transformation

The wavelet transformation is used in applications where the time-variance of the Fourier spectrum is of interest, as in time-frequency analysis and localized time-domain filtering. In this section I will show in which fields the wavelet transformation has found applications, but I will focus on the technique that is used in this thesis.

The power of the wavelet transformation lies in its combined localized and zooming behavior, therefore there is a considerable interest in the field of localized signal filtering. A common application of the wavelet transformation is localized noise reduction. Donoho and Johnstone (1994) developed the most famous example of this use. They showed that when efficiency is not ones main concern, the wavelet transformation can be a very effective tool for noise reduction, especially when the signal contains strong peaks. The results acquired are generally of slightly better quality than conventional (Fourier domain based) filters, but because of its relative inefficiency, it is only used in specific signal processing problems.

The second application I will consider is edge detection in images. When we realize that the human eye has the visual ability to recognize an object from a drawing that only outlines edges, the application in computer vision is clear. Applying recognition algorithms to edges in images is much less computationally involved than applying it to the unprocessed image. To this end, Canny (1986) has presented one of the first edge detection algorithms based on wavelet analysis. Edge detection is the characterization of sharp transitions in (normally) 2-dimensional signals. Wavelet transform analysis is therefore an excellent tool as wavelets are mostly sensitive to transients in signals. From the definition of the continuous wavelet transformation in eq. (2.50), one can see that, noting its strong resemblance with convolution, the wavelet transform of $f(t)$ will have its largest amplitudes at regions where there are sharp perturbations in $f(t)$.

Currently, edge detection is the most wide-spread application of the continuous wavelet transformation. It has found its permanent place in detection and characterization of any kind of signals. Examples can be found, among others, in medicine: segmentation of low-contrast liver tumors in noisy ultrasound images [Yoshida *et al.* (1998)], in finance: extraction of specific features from financial data for forecasting purposes [Aussem *et al.* (1998)] and in geophysics: cross-sections of 3-D migrated seismic data [Hoekstra (1996)].

In this thesis the continuous wavelet transformation is used for perform-

ing *modulus maxima* analysis. This analysis was introduced by Grossmann and Morlet (1984) and further improved practically as well as mathematically by Mallat and Hwang (1992). The purpose of modulus maxima analysis is the extraction of local singularity exponents, which characterize singularities or irregular structures in a signal. In many signals the irregular structures are the most important data carriers. Examples are the strong peaks in data from radio telescopes for the detection of extra-terrestrial intelligence (SETI) and characterization of reflectors in well-logs [Herrmann (1997)]. The latter application is one of the main motives for the research described in this thesis.

To understand the theory of modulus maxima analysis, first the concepts of the 'Wavelet Transform Modulus Maxima' (WTMM) and WTMM-lines (WTMML's) are introduced. In the following discussion, I require that both the signal $f(t)$ and the analyzing wavelet $\vartheta(t)$ are strictly real-valued. Referring to eq. (2.50) the continuous wavelet transform of the signal $f(t)$ is given by $\check{f}(\sigma,t)$. Closely following Mallat and Hwang (1992), the following definitions are given:

- Any point (σ_i,t_j) where $\frac{\partial}{\partial t}\check{f}(\sigma_i,t)$ has a zero-crossing at $t{=}t_j$ is called a *local extremum.*
- The modulus of any point $(\sigma,t){=}(\sigma_i,t_j)$ where $\check{f}(\sigma,t)$ has a local extremum is called a *modulus maximum.*
- Any connected curve in the scale space (σ,t) along which all points are modulus maxima is called a *modulus maxima line.*

Figure 2.4 shows how the modulus maxima lines can be constructed from the wavelet transform of a signal. Figure 2.4a shows a function with three isolated singular points, each of a different nature. The singular points can be described, respectively, by shifted version of $|t|^{-0.4}$ (top), a stepfunction (middle) and $|t|^{0.2}$ (bottom). Making use of the first derivative of the Gaussian $\gamma(t)$ as an analyzing wavelet (for a definition, see appendix A), the wavelet transform of this function is computed, as shown by Fig. 2.4b. Note that the horizontal axis of scale σ is logarithmically spaced. The use of this spacing will become clear in the remainder of this section. Figure 2.4c shows the position of the modulus maxima lines, the lines that interconnect the local maxima in neighboring traces. The different values of grey in Fig. 2.4c represent the amplitudes of the wavelet transform in Fig. 2.4b.

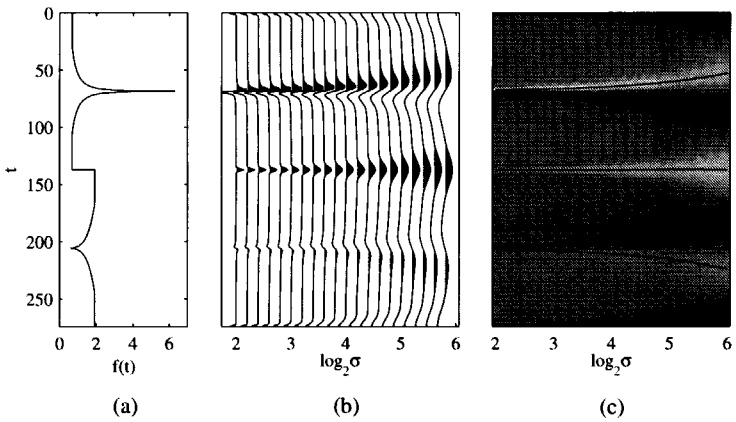

Figure 2.4: *(a) Function $f(t)$ with three isolated singular points, respectively described by shifted versions of $|t|^{-0.4}$ (top), a stepfunction (middle) and $|t|^{0.2}$ (bottom) (b) Wavelet transform $\check{f}(\sigma, t)$, for a discrete set of σ of the function $f(t)$ in (a) (c) Position of modulus maxima lines in the wavelet transform in (b)*

Making use of the above modulus maxima lines, the theory of characterizing singularities in signals is developed. This theory is more generally applicable to the characterization of fractals. Fractals (or fractal sets) have been introduced in the classic paper by Mandelbrot (1974) as functions which obey a *local scaling symmetry*. Local scaling symmetry is the condition when, for a function $f(t)$, around $t{=}t_0$, the following self-similar relationship holds

$$f(\beta(t - t_0)) = \beta^{\alpha} f(t - t_0), \tag{2.56}$$

for $\beta > 0$ and in a suitable, bounded domain. Popular terminology dictates that if eq. (2.56) is pointwise valid for fixed α, the function f is called a *monofractal*; if it is pointwise valid for varying α, f is called a *multifractal*. The parameter α is called the *singularity exponent*, and it characterizes the 'singularity strength' of a particular singular point. The parameter α is also referred to as 'Hölder exponent'.

Now suppose we have a function which locally obeys eq. (2.56), then the following derivation for the wavelet transform of this function can be made. If we skip the factor t_0 in eq. (2.56), we arrive at the following self-similar relation for f

$$f(\beta t) = \beta^{\alpha} f(t). \tag{2.57}$$

The wavelet transform $\check{f}(\sigma, t)$ of this function is defined by eq. (2.50). Replacing t' by $\sigma t'$, t by σt and using eq. (2.57) where β is replaced by σ, we arrive at

$$\check{f}(\sigma, \sigma t') = \sigma^{\alpha+1-\mu} \int_{-\infty}^{\infty} f(t')\, \vartheta(t' - t) dt', \tag{2.58}$$

or, comparing the right-hand side with that of eq. (2.50) for $\sigma = 1$,

$$\check{f}(\sigma, \sigma t) = \sigma^{\alpha+1-\mu}\, \check{f}(1, t). \tag{2.59}$$

Let $t = t_{\max}$ denote the t-value for which $|\check{f}(1, t)|$ reaches a local maximum (i. e. the modulus maximum for $\sigma = 1$ connected to the singular point in f). Substitution in eq. (2.59) gives

$$\check{f}(\sigma, \sigma t_{\max}) = \sigma^{\alpha+1-\mu}\, \check{f}(1, t_{\max}). \tag{2.60}$$

Taking the logarithm of the modulus of both sides of eq. (2.60) yields the following expression for the logarithm of the amplitudes along a modulus maxima line:

$$\log_2 |\check{f}(\sigma, \sigma t_{\max})| = (\alpha + 1 - \mu)\, \log_2 \sigma + \log_2 |\check{f}(1, t_{\max})|. \tag{2.61}$$

For $\mu = 1$ we obtain

$$\log_2 |\check{f}(\sigma, \sigma t_{\max})| = C + \alpha \log_2 \sigma, \tag{2.62}$$

with $C = \log_2 |\check{f}(1, t_{\max})|$. Equation (2.59) shows that a singularity with a singularity exponent α will manifest itself in terms of a cone-like structure in the σ-direction of the wavelet transform, originating at the position of this singularity. Moreover, referring to eq. (2.61), the singularity exponent can be measured from the amplitudes along a modulus maxima line [e.g. Ghez and Vaienti (1989)].

The local nature of the wavelet transformation is essential here. Suppose f is a multifractal, then each singular point in this function can be separately analyzed for its singularity exponent, under the assumption that interference effects in the wavelet transform are small, i. e. the maximum scale σ in the analysis is sufficiently small. Note that we take $\mu = 1$ in eq. (2.62), which is a convenient choice, as the slope of the amplitudes along a modulus maxima line is then given by α.

For the wavelet transform of Fig. 2.4, it was tacitly mentioned that the first derivative of the Gaussian was used as the analyzing wavelet. Figure 2.5 shows both the first and the second derivative of the Gaussian; at this moment we are only interested in their shape. One of the most striking features is that each derivative adds another zero-crossing to this wavelet. The number of zero-crossings in a wavelet defines the convergence properties of a wavelet in the wavelet transform, which is important in the quantification of the singularity parameter α from a signal. It is mathematically more correct to speak in terms of *vanishing moments* of a wavelet [Mallat and Hwang (1992)]. A wavelet $\vartheta(t)$ has q vanishing moments if

$$\int_{-\infty}^{\infty} t^m \vartheta(t) = 0 \quad \text{for} \quad m = 0, \ldots, q-1. \tag{2.63}$$

For wavelets that are q-th order derivatives of the Gaussian, the number of zero-crossings is identical to the number of vanishing moments. The importance of these vanishing moments in singularity analysis is accurately described by Herrmann (1997). In short, if a wavelet has q vanishing moments, then the maximum value of α that we can quantify by multiscale analysis is given by q. If we further assume that the wavelet is infinitely differentiable (e.g. the Gaussian), then the range of α we can quantify is given by $[-\infty, q]$.

Figures 2.6a-c show the same function and its wavelet transform as in Figure 2.4. Given the fact that the maximum α-value in the signal $f(t)$ is 0.2, the original choice for the analyzing wavelet is valid. Namely, the first derivative of the Gaussian has one zero-crossing, hence $q = 1$, which enables us to quantify α up to 1. Equation (2.62) shows that the singularity exponent

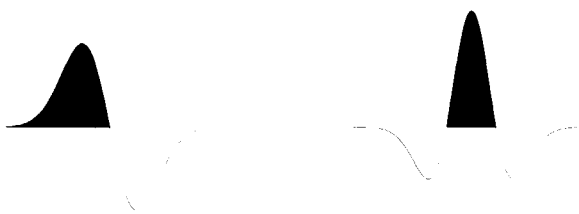

Figure 2.5: *(a) The first derivative of the Gaussian, in this thesis used as the analyzing wavelet in the wavelet transformation. (b) The opposite of the second derivative of the Gaussian, commonly referred to as the 'Ricker wavelet'.*

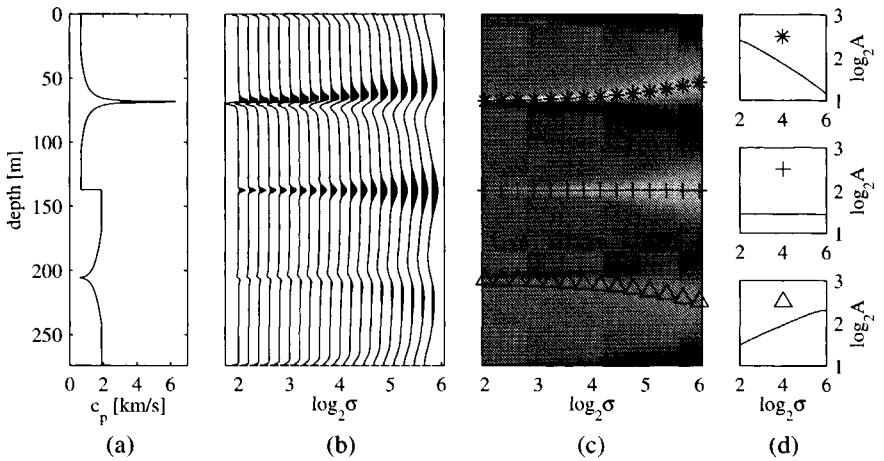

Figure 2.6: *(a) Function $f(t)$ with three isolated singular points, respectively described by shifted versions of $|t|^{-0.4}$ (top), a stepfunction (middle) and $|t|^{0.2}$ (bottom)*
(b) Wavelet transform $\check{f}(\sigma, t')$, for a discrete set of σ-values of the function $f(t)$ in (a)
(c) Position of modulus maxima lines in the wavelet transform in (b)
(d) Double-logarithmic plots of the amplitudes along the depicted modulus maxima lines in (c). The slopes are given by resp. -0.4, 0 and 0.2

can be measured by the corresponding power law divergence in the wavelet transform. We therefore extract the amplitudes along the modulus maxima lines in Fig. 2.6c and plot them in double-logarithmic scale in Figures 2.6d. I will refer to these graphs as Amplitude-Versus-Scale-curves (AVS-curves). Equation (2.62) can be more practically interpreted, by seeing that α is actually the slope along the corresponding AVS-curve. This interpretation can be checked by measuring the slope of the amplitudes along the three modulus maxima lines. The result is, as expected, that the slopes are given by resp. -0.4, 0 and 0.2, which is the same as the exponent in the local description of the singularities in $f(t)$. I will refer to the above procedure as *multiscale analysis*.

2.7 Multiscale analysis of well-logs

Herrmann (1997) describes how the method for estimating the singularity exponent α can be applied to reflectors in real well-logs. Well-logs are

densely sampled ($\frac{1}{2}$ft $= 0.1524$m) measurements of local velocities in a borehole. It gives the velocity profile at a much finer sampling than can be acquired by a surface seismic experiment, and it is used in constructing velocity profiles for migration and characterization of the very fine properties of the subsurface. Herrmann recognized that velocity functions of the subsurface show a striking resemblance with other multifractal functions, which can be found in pure mathematics (e.g. the Cantor set), in physics (the temperature in Rotterdam) and in economics (the stock rates at Wall Street).

Figure 2.7a shows a typical example of a well-log, which was kindly provided by Mobil. It shows the very high frequent variations in the seismic velocity, and shows that our conventional view of reflectors in the subsurface by stepfunctions [Zoeppritz (1919)] must be a strong simplification to the real Earth. In Fig. 2.7a three reflectors are depicted, which will be further analyzed by multiscale analysis. Figures 2.7b and c are both representations of the continuous wavelet transform, just as in Section 2.6. For the wavelet the second derivative of the Gaussian was used and $\mu = 1$. In Fig. 2.7c the modulus maxima lines corresponding to the three reflectors in Fig. 2.7 are drawn. Figure 2.7d shows the AVS-curves measured along these modulus maxima lines. We can see that the slopes of these lines can range from slightly positive to negative, indicating that the reflectors can be scale-dependent and can not all be described by stepfunction interfaces. A thorough analysis by Herrmann on many different well-logs showed that interfaces in the subsurface have singularity exponents ranging from strongly negative ($\alpha \approx -2$) up to slightly positive ($\alpha \approx 0.5$). Although the slope along the AVS-curves is not perfectly constant, the approximation that α is constant in a certain scale range is much less restrictive than assuming stepfunction interfaces ($\alpha = 0$ everywhere), as is usually done. In the next section these results will be used to develop a generalization of Zoeppritz boundaries to self-similar interfaces. This generalization will be used in this thesis to describe and characterize reflectors and seismic reflections.

2.8 A generalized parameterization of reflectors in the subsurface

The foregoing section has shown that for many reflectors in the earth's subsurface, a representation by stepfunctions in the velocity or impedance is not sufficient. Therefore, I discuss a generalized model for the velocity function that better captures the singular behavior of real well-logs.

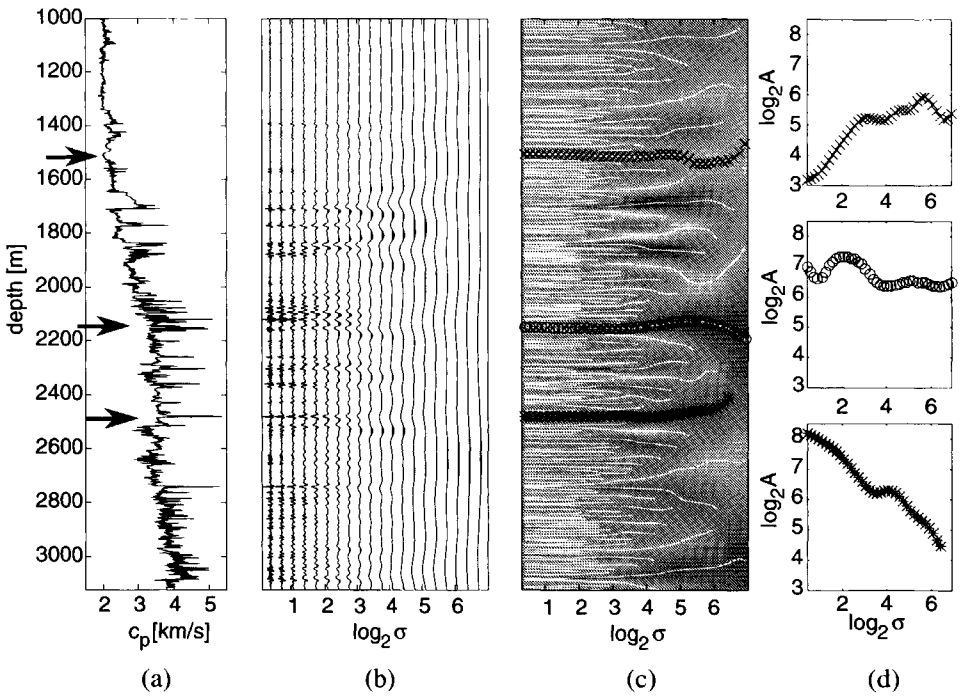

Figure 2.7: *Multiscale analysis of a well-log [Herrmann (1997)].*
(a) The original well-log (courtesy Mobil).
(b) The wavelet transform of the well-log in (a).
(c) Modulus maxima lines, obtained from the modulus of (b).
(d) Double-logarithmic plots of the amplitudes along the depicted modulus maxima lines in (c). A positive, a zero and a negative slope (singularity strength) can be discerned.

As has been show in Section 2.7, the following *self-similar* relationship holds approximately for many reflectors in the subsurface, within a limited scale range

$$c(\beta z) = \beta^{\alpha} c(z). \tag{2.64}$$

For stepfunctions, this relation simplifies to

$$c(\beta z) = c(z), \tag{2.65}$$

which means that stepfunctions are invariant under scaling. Comparing eq. (2.65) with eq. (2.64) shows that for stepfunctions the parameter α is equal to 0. When we compare this result with the slope in the AVS-curve corresponding to the middle singularity in Fig. 2.6a (the stepfunction), we see that these results are consistent. If the parameter α deviates from 0, it means that we are not dealing with stepfunctions, but with other types of reflectors.[2] Therefore, in this thesis I will use a model for reflectors in the subsurface that must be:

1. a generalization of stepfunction interfaces,
2. able to represent a parameter α in multiscale analysis (for realistic α).

The model I will use fulfills both requirements and is described by a well-log that contains (shifted versions of) a singularity in the velocity function $c(z)$ of the form

$$c(z) = \begin{cases} c_1 |z/z_1|^{\alpha} & \text{for } z < 0 \\ c_2 |z/z_1|^{\alpha} & \text{for } z > 0, \end{cases} \tag{2.66}$$

in which α is the dimensionless singularity exponent. $c_{1,2}$ are constants which define the actual velocity at $z = \pm z_1$. The parameter z_1 serves two purposes: one is to make the division $|z/z_1|$ dimensionless and the second is to determine the distance between the two points where $c(z)$ is c_1 at $z < 0$ and c_2 at $z > 0$ respectively. As both sides of the velocity model (i.e. above and below $z = 0$) obey local self-similar behavior, this model will be called the *two-sided singularity model.*

It should be noted that other models for singularities in the subsurface are proposed, which are also a generalization of stepfunctions. As an example of

[2] This argument can not be reversed. When we measure a singularity exponent of $\alpha = 0$ for a reflector, we do not necessarily have a stepfunction, cf. the middle reflector in Figure 2.7.

such models, I refer to Dessing (1997), who proposes a so-called one-sided singularity model described by either

$$c(z) = c_0 + \begin{cases} c_1|z/z_1|^{\alpha_1} & \text{for } z < 0 \\ 0 & \text{for } z > 0, \end{cases} \tag{2.67}$$

or

$$c(z) = c_0 + \begin{cases} 0 & \text{for } z < 0 \\ c_2|z/z_1|^{\alpha_2} & \text{for } z > 0. \end{cases} \tag{2.68}$$

Dessing (1997) has chosen this parameterization to acquire a generalized model for reflectors in the subsurface. An important result acquired by Dessing is the so-called (ϕ, α)-diamond, which classifies one-sided singularities by their effect on the phase of seismic reflection responses.

It will be shown in Chapter 3, Section 3.5, that velocity functions described by the two-sided singularity model are equally well able to account for these phase shifts. The simplicity of the two-sided singularity model in eq. (2.66), however, is one of the main reasons for choosing this model as the standard singularity model in this thesis.

2.9 Conclusions

This chapter has given an overview of transformations that are used within this thesis to process well-log and seismic reflection data. It has been shown (e.g. by Herrmann (1997)) that well-logs exhibit multifractal behavior over a large range of scales, which can be quantified by a singularity parameter α. This singularity parameter describes the local self-similar behavior of the velocity field. In the remainder of this thesis, we consider the possibility of extracting this local self-similar behavior from seismic reflection data. To this end, analytical expressions for the rayparameter-dependent reflectivity at the proposed generalized reflector model will be derived. Further, inversion schemes based on these analytical expressions are developed and tested on synthetic and field data.

Chapter 3

Multiangle multiscale characterization of acoustic seismic reflection data

In Chapter 2 the definition of the continuous wavelet transform and an overview of a method for extracting a singularity parameter α from well-logs were given. This chapter is focused on a method for retrieving this singularity parameter from seismic reflection data modeled in these well-logs. A method for the inversion for the singularity parameter is presented, which makes use of rayparameter-dependent seismic reflection data. Furthermore, it will be shown that the instantaneous phase of a reflection event contains complementary information that can be used in the inversion for both the singularity parameter and a velocity contrast ratio.

3.1 Approximation of singular velocity fields by superposition of homogeneous layers

The velocity model that is proposed in Chapter 2, Section 2.8, is given by

$$c(z) = \begin{cases} c_1 |z/z_1|^\alpha & \text{for } z < 0 \\ c_2 |z/z_1|^\alpha & \text{for } z > 0. \end{cases} \tag{3.1}$$

Obviously, for $\alpha < 0$, the velocity function $c(z)$ becomes infinite for $z \to 0$ or, for $\alpha > 0$ and $z \to 0$, the velocity becomes zero. As is shown by Wapenaar (1999), taking the usual boundary conditions at $z = 0$, i.e. continuity of the pressure and the vertical component of the particle velocity, closed form

finite reflection and transmission coefficients for this model can be acquired. This means that the wave equation can handle these singularities, in a similar way as it can handle stepfunction interfaces.

In conventional numerical modeling techniques for the construction of wave fields, the background velocity (and density) model is a discretized version of the actual model. Hence, in numerical modeling, the velocity function of eq. (3.1) can not be used at the point $z = 0$, as infinite or zero velocities are generally not properly treated. The preferred modeling technique in this thesis is the reflectivity method, as developed by Kennett (1983). This method assumes homogeneous layers with stepfunction interfaces, which is clearly different from the model described by eq. (3.1), with $\alpha \neq 0$. We therefore approximate this model by a stack of thin layers with increasing or decreasing velocities. Note that thin is quantified as being much thinner than the minimum spatial wavelength of the modeled wave. A practical choice is to take the spatial sampling of the model in the order of the spatial sampling of most well-logs, which is $\frac{1}{2}$ ft (0.1524 m), which is much smaller than the minimum spatial wavelength of real and modeled wave fields (in the order of 5-10 m). We put the singular point halfway between two sample points, to avoid practical problems concerning zero or infinite velocities.

Figure 3.1 shows a singular velocity model, for $\alpha = -0.3$, $c_1 = c_2 = 1800$ m/s and $z_1 = 1$ m, depicted by the black line. The gray line is the approximation of this model, with homogeneous layers of 0.2 m thickness and where at $z = 0$, the velocity is now finite. Every time a synthetic model is generated, we assume that the above approximation sufficiently describes the analytical singularity. In the remainder of this chapter, it is shown that analytical expressions for the reflection at these velocity functions are in agreement with the modeled reflection data, which supports this assumption.

3.2 An implicit relation for the angle-dependent reflectivity of the singular velocity model

In this section, an implicit relation is derived for the multiangle multiscale reflectivity of a singular reflector described by eq. (3.1). This relation will be used to estimate the singularity parameter α from seismic reflection data. The starting point of this derivation is the scalar acoustic wave equation in the space-time domain, where we assume a line-source (taken as the y-axis),

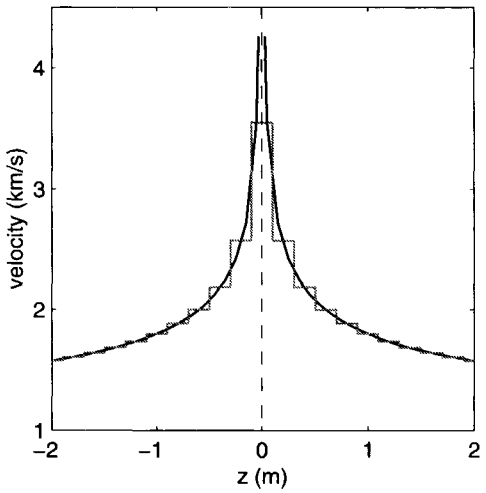

Figure 3.1: *(a) singular velocity function $c(z)$ (black), for $\alpha = -0.3$, $c_1 = c_2 = 1800$ m/s and $z_1 = 1$ m. (b) approximation of $c(z)$ by homogeneous layers of 0.2m thickness (grey).*

given by

$$\left[\frac{\partial^2}{\partial x^2} + \frac{\partial^2}{\partial z^2} - \frac{1}{c^2(z)}\frac{\partial^2}{\partial t^2}\right] u(x,z,t) = 0. \tag{3.2}$$

As is shown, e.g. by McCowen and Brysk (1989), we can rewrite eq. (3.2) such that it describes the wave field in terms of plane waves, according to

$$\left[\frac{\partial^2}{\partial z^2} - \left(\frac{1}{c^2(z)} - p^2\right)\frac{\partial^2}{\partial \tau^2}\right] \tilde{u}(z,p,\tau) = 0. \tag{3.3}$$

Equation (3.3) is the scalar acoustic wave equation in the Radon transform (p,τ) domain. In Chapter 2, Section 2.2.5, the linear Radon transformation has been treated, which transforms seismic reflection data from the space-time domain to this domain.

Using eq. (3.3), it is now possible to derive an implicit expression for the rayparameter-dependent reflectivity of singular velocity models described by eq. (3.1). We replace z by βz, and substitute the self-similar relation of velocity functions obeying eq. (3.1), which is $c(\beta z) = \beta^{\alpha} c(z)$ [cf. eq. (2.64)].

Next, we multiply the result by β^2 to get from eq. (3.3)

$$\left[\frac{\partial^2}{\partial z^2} - \Big(\frac{1}{c^2(z)} - (\beta^\alpha p)^2\Big)\frac{\partial^2}{(\partial\beta^{\alpha-1}\tau)^2}\right]\tilde{u}(\beta z, p, \tau) = 0. \tag{3.4}$$

The term between the square brackets is the same as in eq. (3.3), with p replaced by $\beta^\alpha p$ and τ replaced by $\beta^{\alpha-1}\tau$. Hence, eq. (3.4) is satisfied by $\tilde{u}(z, \beta^\alpha p, \beta^{\alpha-1}\tau)$ as well as $\tilde{u}(\beta z, p, \tau)$. Consequently,

$$\tilde{u}(z, \beta^\alpha p, \beta^{\alpha-1}\tau) = f(\alpha)\tilde{u}(\beta z, p, \tau), \tag{3.5}$$

where $f(\alpha)$ is an undetermined α-dependent factor. In the upper half-space $z < 0$ we define an 'incident' wave field $\tilde{u}^{\text{inc}}$ and a 'reflected' wave field $\tilde{u}^{\text{refl}}$, both obeying eq. (3.5) with one and the same factor $f(\alpha)$. For our analysis we do not need to specify this 'decomposition' any further. We relate these incident and reflected wave fields via a reflection kernel $\tilde{r}(p, \tau)$, according to

$$\tilde{u}^{\text{refl}}(-\epsilon, p, \tau) = \int_{-\infty}^{\infty} \tilde{r}(p, \tau - \tau')\tilde{u}^{\text{inc}}(-\epsilon, p, \tau')d\tau', \tag{3.6}$$

with $\epsilon \to 0$. When we replace ϵ by $\beta\epsilon$ and substitute eq. (3.5) for $\tilde{u}^{\text{inc}}$ and $\tilde{u}^{\text{refl}}$, we can compare the result with eq. (3.6), which shows that the reflection kernel $\tilde{r}(p, \tau)$ obeys the following similarity relation

$$\tilde{r}(p, \tau) = \beta^{\alpha-1}\tilde{r}(\beta^\alpha p, \beta^{\alpha-1}\tau). \tag{3.7}$$

We now apply the continuous wavelet transformation to $\tilde{r}(p, \tau)$ [cf. eq. (2.50)], according to

$$\check{r}(p, \sigma, \tau) = \int_{-\infty}^{\infty} \tilde{r}(p, \tau')\vartheta\Big(\frac{\tau' - \tau}{\sigma}\Big)d\tau'. \tag{3.8}$$

Note that in this case we have taken the normalization coefficient $\mu = 0$. Substituting eq. (3.7), replacing τ' by $\beta^{1-\alpha}\tau'$ and $d\tau'$ by $\beta^{1-\alpha}d\tau'$ yields

$$\check{r}(p, \sigma, \tau) = \int_{-\infty}^{\infty} \tilde{r}(\beta^\alpha p, \tau')\vartheta\Big(\frac{\tau' - \beta^{\alpha-1}\tau}{\beta^{\alpha-1}\sigma}\Big)d\tau', \tag{3.9}$$

or, comparing the right-hand side with that of eq. (3.8),

$$\check{r}(p, \sigma, \tau) = \check{r}(\beta^\alpha p, \beta^{\alpha-1}\sigma, \beta^{\alpha-1}\tau). \tag{3.10}$$

Let $\tau = \tau_{\max}$ denote the τ-value for which $|\check{r}(p, \sigma, \tau)|$ reaches its maximum for fixed p and σ. We will refer to this level in the data set as a *modulus maxima plane*; in Section 3.3.3 this concept will be more accurately defined. It follows from eq. (3.10) that the reflection amplitude in a modulus maxima plane behaves as

$$|\check{r}(p, \sigma, \tau_{\max})| = |\check{r}(\beta^{\alpha} p, \beta^{\alpha-1}\sigma, \beta^{\alpha-1}\tau_{\max})|. \tag{3.11}$$

The latter equation implies that contours of constant reflection amplitude in a modulus maxima plane are described by

$$p^{1-\alpha}\sigma^{\alpha} = \text{constant}. \tag{3.12}$$

Note that for $\alpha = 0$ (e.g. the reflection at a stepfunction interface) these contours reduce to straight lines, described by $p = \text{constant}$. This means that the reflectivity of an interface between two halfspaces is scale independent, which is a well-known result. On the other hand, any deviation from these straight lines indicates that we are dealing with a singularity, other than the stepfunction. If we assume normal incidence data ($p = 0$) only, eq. (3.12) is not defined. This means that, using the implicit relation of eq. (3.12), it is not possible to resolve the singularity parameter α when only normal incidence data is available. The incorporation of rayparameter-dependent data is therefore required. When we incorporate rayparameter-dependent data, we can see that eq. (3.12) is only dependent on α, because σ and p are the variables which define the axes of the modulus maxima plane $|\check{r}(p, \sigma, \tau_{\max})|$. In the next section a method is proposed to recover the singularity parameter α from seismic reflection data, making use of eq. (3.12).

3.3 Estimating the singularity exponent from the amplitudes in modulus maxima planes

In section 3.2 an implicit expression [eq. (3.12)] is derived for the rayparameter and scale dependency of the amplitudes of the reflection at a self-similar interface. In this section a method is proposed for retrieving the singularity parameter α from seismic reflection data, making use of this expression. The method consists of four steps:

First, the data are transformed to a plane-wave representation, by means of the linear Radon transformation. Following, the data are imaged to the (p, z) domain, to acquire flat events, which are more easily analyzed. Third,

the data are wavelet-transformed to create the data cube $\check{\mathrm{R}}(p, \sigma, z)$. In this data cube, the modulus maxima planes are constructed, and finally, the reflection amplitudes in these modulus maxima planes are inverted for the singularity parameter α.

In the following subsections these four steps are further treated. A synthetic example illustrates the method.

3.3.1 Linear Radon transformation of seismic reflection data

Seismic reflection data are normally measured in shotgathers. A source is ignited, and a set of detectors measure the Earth's response. In the following analysis we require that the sources and receivers are organized along one line, such that the measurements are dependent on one spatial coordinate (denoted by x) and the time t. Now, from several shotgathers, the measurements are combined that share the same midpoint of source and receiver, to acquire common midpoint gathers (CMPs). As was posed in the foregoing section, for wave fields that are generated by a line-source, the Radon transformation is exactly a decomposition into plane waves, fulfilling the wave equation given by eq. (3.3). Therefore, we assume that the Earth can be locally approximated by a 1-D medium (only contrasts in the depth (z) direction). In practice, this means that we require that fluctuations of the medium parameters in the inline (x) and crossline (y) direction around the midpoint of a CMP are small, such that they can be ignored.

The first step in the inversion for the singularity parameter α is the application of the Radon transformation to the CMP-gathers. A synthetic data set was generated, using the velocity function shown in Fig. 2.6a in Chapter 2. Note that this velocity function contains isolated singularities for both a negative and a positive singularity parameter α. Further, a stepfunction interface is present. The density was chosen at a constant value of 1500 kg/m^3.

Figure 3.2a shows a synthetic CMP-gather in the space-time domain, Fig. 3.2b shows the same gather, but now in the Radon domain, as modeled in the velocity function in Fig. 2.6a. The forward modeling used for these data is the acoustic reflectivity method, as developed by Kennett (1983).

3.3.2 Imaging of the rayparameter-dependent reflectivity

The second step in the inversion for the singularity parameter α, is to acquire a depth section of the reflectivity $\tilde{u}(p, \tau)$. To this end, an imaging algorithm is applied, that maps the intercept time τ to the depth coordinate z, according

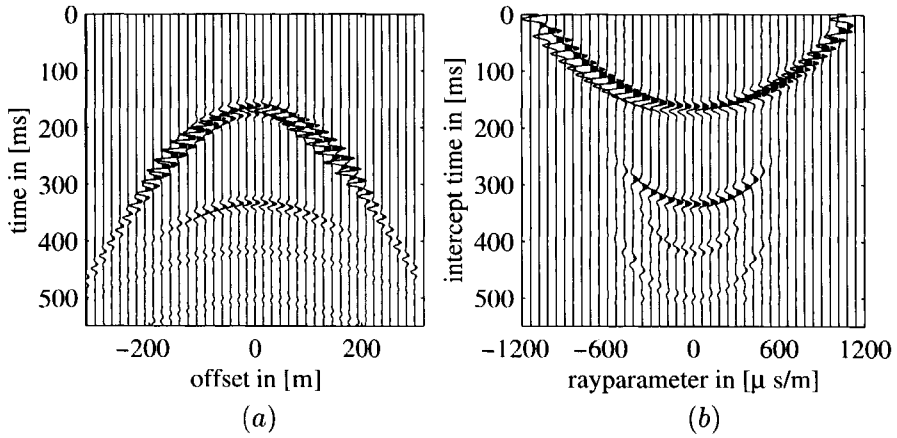

Figure 3.2: *(a) Synthetic CMP-gather in the space-time domain (b) Synthetic CMP-gather in the Radon domain.*

to the method of Clayton and McMechan (1981). This time-to-depth conversion is performed in the temporal Fourier domain, therefore the reflectivity $\tilde{u}(p,\tau)$ is Fourier-transformed to acquire the data set $\tilde{U}(p,\omega)$. Imaging is performed by multiplying $\tilde{U}(p,\omega)$ with a simple phase-shift operator, and summing over the frequencies (equivalent to taking the zero time component), according to

$$\mathsf{R}(p,z_i) = \sum_{\omega} \tilde{U}(p,\omega) \exp\left(2j\omega T(p,z_i)\right), \tag{3.13}$$

where $T(p,z_j)$ is defined as

$$T(p,z_i) = \sum_{k=0}^{i} \sqrt{\frac{1}{c^2(z_k)} - p^2}\,\Delta z_k, \tag{3.14}$$

where Δz_k is the thickness of each consecutive layer. The above imaging procedure is performed for all depth levels z_i, to acquire the full depth image of the reflectivity $\mathsf{R}(p,z)$. Note that the above imaging procedure is a strict primary wavefield operation, such that multiple arrivals are not imaged correctly. Figure 3.3 shows the rayparameter-dependent image of the reflectivity acquired from imaging the data in Fig. 3.2b. Clearly, Amplitude-Versus-rayParameter (AVP) effects are visible, especially on the first reflection.

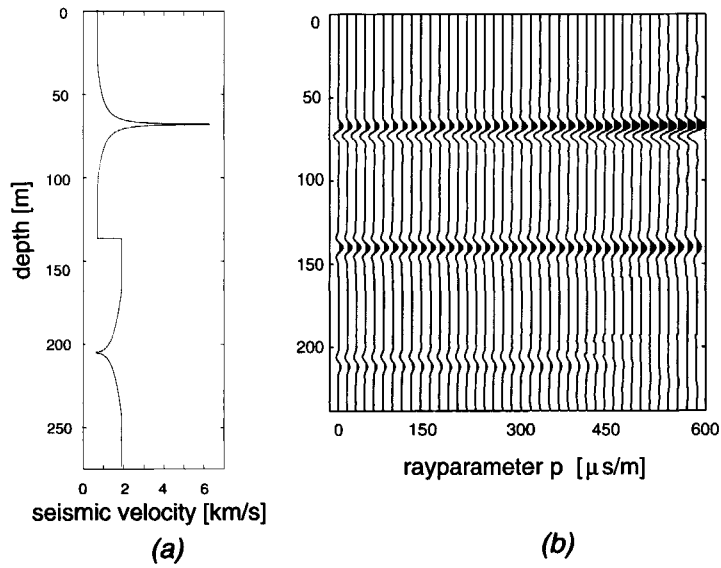

Figure 3.3: *(a) Synthetic velocity function (identical to the one in Fig. 2.6a) containing three isolated singularities, with singularity exponents α of -0.4, 0 and 0.2 respectively. (b) Imaged reflection data $R(p, z)$ from imaging the data in Fig. 3.2b.*

3.3.3 Construction of modulus maxima planes in the wavelet transform of the rayparameter-dependent image of the reflectivity

The rayparameter-dependent image of the reflectivity $R(p, z)$, constructed by the above imaging procedure, is transformed to the wavelet domain according to

$$\check{R}(p, \sigma, z) = \int_{-\infty}^{\infty} R(p, z')\vartheta\Big(\frac{z' - z}{\sigma}\Big)dz'. \tag{3.15}$$

The result is a 'cube' of data on which the following analysis is applied.

In Section 3.2, it was stated that the modulus maxima plane is the two-dimensional generalization of the modulus maxima line. The construction of these planes is as follows. The first step is to construct modulus maxima lines for each wavelet-transformed trace $\check{R}(p_i, \sigma, z)$. The result of this analysis is a set of neighboring modulus maxima lines. Now the modulus maxima

lines, belonging to the same seismic reflection are connected, to acquire the complete modulus maxima planes, for each event in the data. Referring to Chapter 2, Section 2.6, where the modulus maxima line is defined, the modulus maxima plane is therefore defined as

- the union of the modulus maxima lines in the wavelet-transformed data $\check{\mathsf{R}}(p, \sigma, z)$, belonging to the same rayparameter-dependent seismic reflection event in the image $\mathsf{R}(p, z)$ is called a modulus maxima plane.

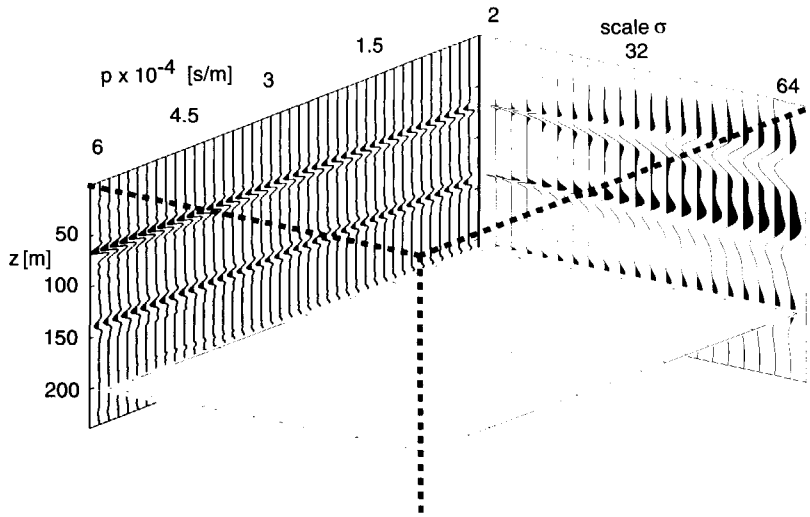

Figure 3.4: *The continuous wavelet transform $\check{\mathsf{R}}(p, \sigma, z)$ of the imaged reflectivity in Fig. 3.3b. The modulus maxima plane for the bottom reflection in the data is depicted, where contours of constant reflection amplitudes are drawn.*

An example of this cube of wavelet-transformed imaged data is depicted in Fig. 3.4. In this figure, we see the wavelet transform of the image in Fig. 3.3b, where the analyzing wavelet $\vartheta(z)$ is the first derivative of the Gaussian. The left backplane is the image from Fig. 3.3b, the right backplane is the continuous wavelet transform of the trace at $p = 0$. The modulus maxima plane belonging to the bottom reflection (the reflection connected to the reflector with $\alpha = 0.2$) is also depicted. Similar modulus maxima planes can be constructed for the other two reflections.

On the modulus maxima plane, contours of constant reflection amplitude in the wavelet-transformed image $|\check{\mathsf{R}}(p, \sigma, z)|$ are drawn. In the next subsec-

tion, it will be shown how, from these contours, an estimate of the singularity parameter α can be acquired.

3.3.4 Inversion for the singularity parameter

From the three reflections in Fig. 3.3b, the modulus maxima planes are created. In Fig. 3.5a-c we see surface plots of the absolute values of the amplitudes in these modulus maxima planes, derived from the respective reflections in the data of Fig. 3.3b.

Fig. 3.5b shows clearly that an oblique reflection on a stepfunction in the velocity field ($\alpha = 0$) is scale-independent. When it is realized that scale σ is proportional to the inverse of frequency ω, this effect can be easily understood, as it is commonly known that the reflectivity of stepfunctions is frequency independent. Reflections on singular velocity profiles, on the other hand, are clearly scale dependent for oblique incidence [cf. Fig. 3.5a,c]. We see that for $\alpha < 0$, the reflectivity decreases with scale, whereas for $\alpha > 0$, the reflectivity increases with scale. Note that for higher p-values we see scale independent behavior in both Figs. 3.12a,b. This is due to the incorporation of post-critical reflections in this analysis.

From Figs. 3.5a-c, contours of constant reflection amplitudes are derived, for pre-critical reflection only. These contours are shown in Figs. 3.5def. We see that the contours have a distinct behavior for different values of α. For $\alpha < 0$ (Fig. 3.5d), we see that the contours follow a J-shaped pattern, for $\alpha = 0$ (Fig. 3.5e) they are vertical, and for $\alpha > 0$ (Fig. 3.5f) they follow an inverse J-shaped pattern. This qualitative behavior is typical for these three ranges of the singularity parameter α and can be used as direct indicator of the sign of α. The *quantitative* behavior of these contours is now used to estimate the singularity parameter α from seismic reflection data.

The shape of the contours in these figures can be computed analytically by applying eq. (3.12) in the range of p and σ for which the data were analyzed. In Fig. 3.5g-i we can see these analytical contours, for the three values of α ($-0.4, 0$ and 0.2, respectively).

When we compare the contours of constant reflection amplitudes in Figs. 3.5d-f with the – expected – analytical contours (Figs. 3.5g-i) we can see that there is a strong resemblance.

The exact shape of the contours can be used to estimate the singularity parameter α from the reflection data, by computing the contours of eq. (3.12) for a range of α-values, which we expect to exist in the data set, and match these with the contours extracted from the seismic data. Referring to Herr-

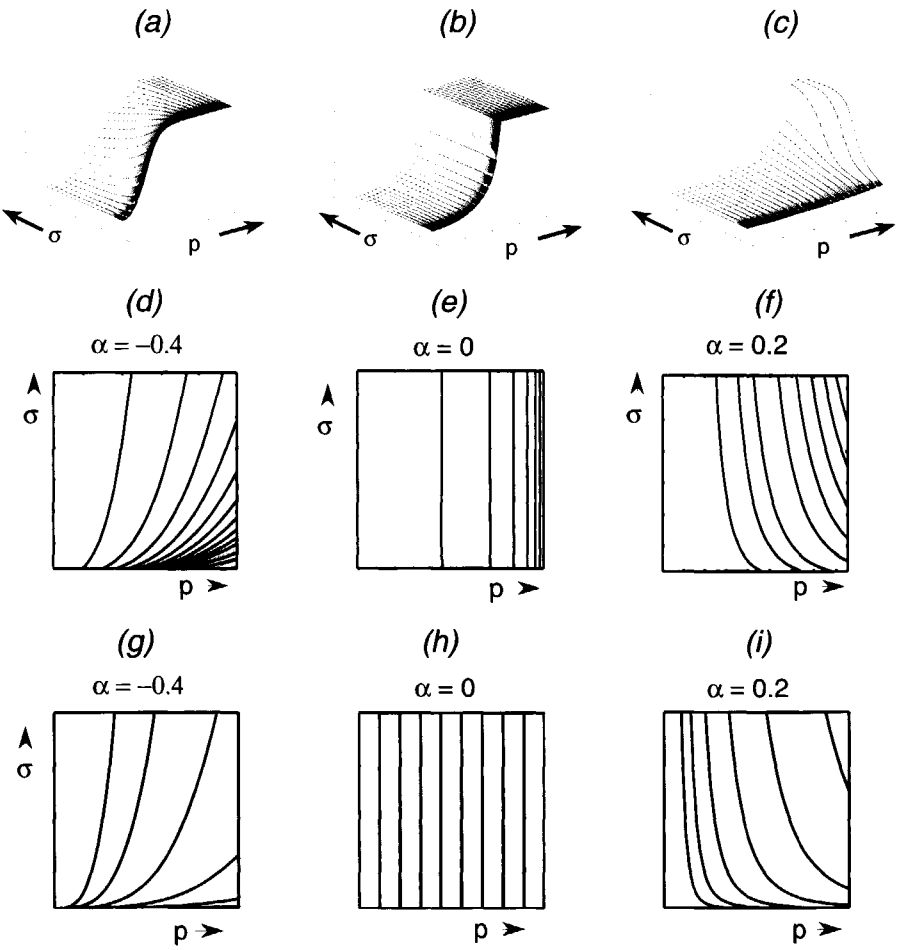

Figure 3.5: *(abc) Surface plots of reflectivity* $|\check{R}(p, \sigma, z_i)|$ *for* α *= -0.4, 0 and 0.2. (def) Contourplots of pre-critical reflectivity* $|\check{R}(p, \sigma, z_i)|$ *for* α *= -0.4, 0 and 0.2. (ghi) Analytical contours for* α *= -0.4, 0 and 0.2*

mann (1997), we assume that singularity parameters α in well-logs range from quite strongly negative ($\alpha_{\min} \approx -1$) up to slightly positive ($\alpha_{\max} \approx 0.5$).

The matching algorithm is set up as follows. For every α in the above range, the analytical contours are constructed. Next, the standard deviations $s(\alpha)$ of the reflection amplitudes in the modulus maxima planes along these analytical contours are computed, according to

$$s(\alpha_k) = \frac{1}{M} \sum_{i=1}^{M} \sqrt{\frac{\sum_{j=1}^{N_i} \left(|\check{\mathsf{R}}(p_{ij}, \sigma_{ij}, z_{\max})| - \overline{|\check{\mathsf{R}}(p_i, \sigma_i, z_{\max})|} \right)^2}{N_i}} \tag{3.16}$$

where α_k is one value in a range of singularity parameters $\alpha \in [\alpha_{\min}, \alpha_{\max}]$. In this equation, N_i is the number of samples for each analytical contour, M is the number of analytical contours, along which the matching algorithm is applied. $\overline{|\check{\mathsf{R}}(p_i, \sigma_i, z_{\max})|}$ is the mean value of the measured multiscale amplitudes along an analytical contour.

Finally, an estimate of the singularity parameter α can be found by finding the α_{opt}-value for which the standard deviation function $s(\alpha)$ exhibits its global minimum, according to

$$\alpha_{\text{opt}} = \{\alpha_k | s(\alpha_k) = \min(s(\alpha))\}. \tag{3.17}$$

This inversion scheme is applied to the contours depicted in Fig. 3.5def. Figs. 3.6a-c show the graphs of the respective standard deviations for these contours. It is clear that pronounced minima in these graphs are present. For each graph, the minimum occurs at the expected singularity parameter α-value ($-0.4, 0$ and 0.2, respectively). Note that in Fig 3.6a, we see that there can be more than one local minimum in these standard deviation graphs. In this figure, a local maximum standard deviation is found at $\alpha \approx 0.1$; for α-values larger than 0.1, the standard deviation decreases. The contours for $\alpha = 0.1$ are maximally perpendicular to the ones for $\alpha = -0.4$, thus giving this maximum standard deviation. However, the optimal α-value can still be found by taking the absolute minimum along these standard deviations.

An inversion scheme, based on matching analytical contours described by eq. (3.12) with contours derived from multiscale reflectivity amplitudes has been presented. It can be used to estimate a singularity parameter α from seismic reflection data. This singularity parameter is consistent with the one derived from a velocity model, in which the seismic reflection data were modeled.

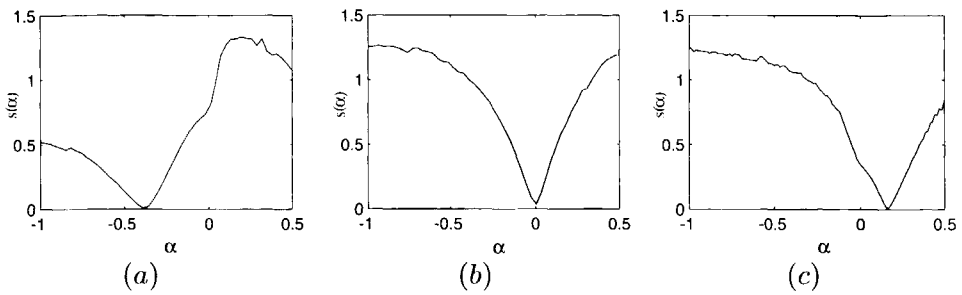

Figure 3.6: *Graphs of the standard deviation $s(\alpha)$ of multiscale reflection amplitudes along analytical contours described by $p^{1-\alpha}\sigma^{\alpha} = \text{constant}$, for the cases (a) $\alpha = -0.4$, (b) $\alpha = 0$ and (c) $\alpha = +0.2$.*

3.4 Application of the inversion scheme to data modeled in real well-logs

The foregoing section has proposed a method for estimating the singularity parameter α from seismic reflection data. To further analyze the method, real data are used. First a test on synthetic seismic reflection data, modeled in real well-logs, was performed. The results of this analysis are presented in this section. The next step has been the application of the method to a complete field data set. The analysis of such a field data set was performed during a three-months visit at Shell Research Center in Rijswijk. For this purpose, a field data set was made available, which was measured (on land) in the northern part of Friesland. It consisted of common-offset migrated gathers and one well-log of the P-wave velocity. Unfortunately, the contours describing constant reflection amplitudes in the modulus maxima planes were severely affected by the relatively high noise level in the seismic data. Further, the maximum angle of incidence present in the data was not sufficient to clearly exhibit AVO behavior in the data. Hence, the minimum requirements for a successful application of the method were not reached. As a result, it is decided not to cover this analysis in this thesis.

The proposed inversion scheme is applied to seismic reflection data modeled in actual velocity functions from well-logs. Two distinct types of reflectors are analyzed. The first example covers a reflector that is described by a negative singularity exponent, the second example covers a reflector described by a stepfunction ($\alpha \approx 0$). Figures 3.7a,b,c show the multiscale

analysis of a real well-log, made available by Mobil, analogous to the multiscale analysis of the synthetic velocity function as shown in Fig. 2.6. A reflector is chosen at the depth $z = 155$m (denoted by the black arrow in Fig. 3.7a), for which the singularity parameter is measured. The slope along

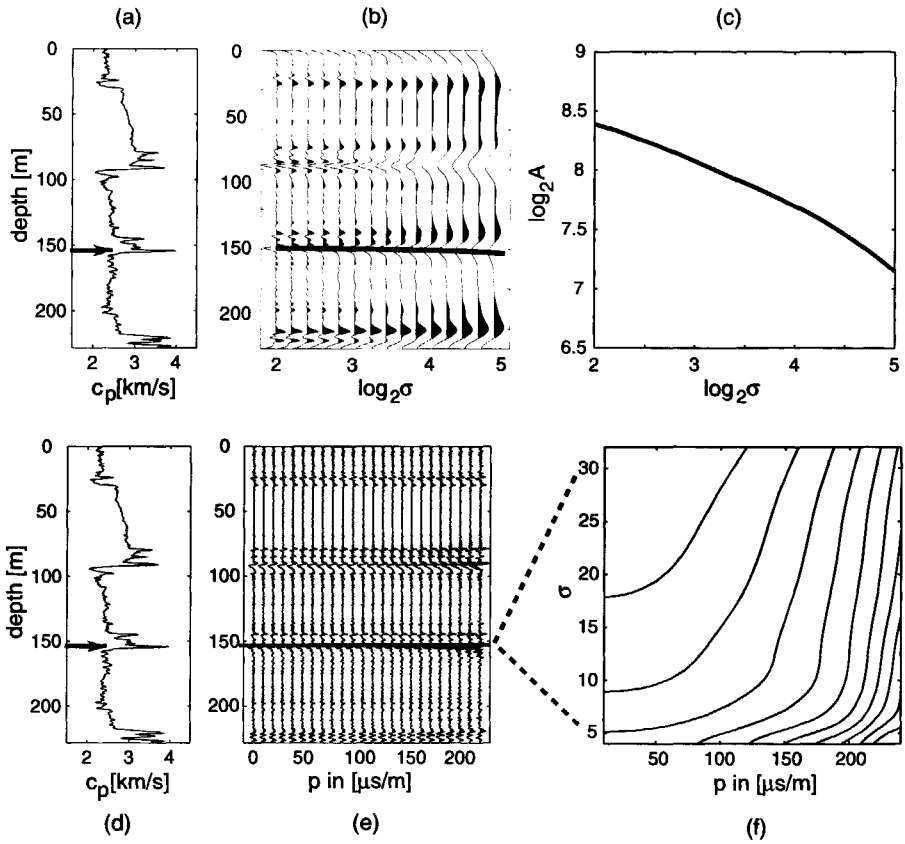

Figure 3.7: *(a,b,c) Multiscale analysis of a singularity in a well-log:* $\alpha = -0.32$. *(d,e,f) Multiangle, multiscale analysis of its seismic response:* $\alpha = -0.34$.

the modulus maxima line in Fig. 3.7c characterizes the singularity. A value of the singularity parameter is found at $\alpha = -0.32$. Data were modeled in this velocity model, using an acoustic reflectivity method; the density was chosen at a constant value of $\rho = 2000\text{kg/m}^3$. In Figure 3.7e the imaged rayparameter-dependent reflectivity is shown. The reflection at $z = 155$m depth is recognized as the reflection that correlates with the depicted reflec-

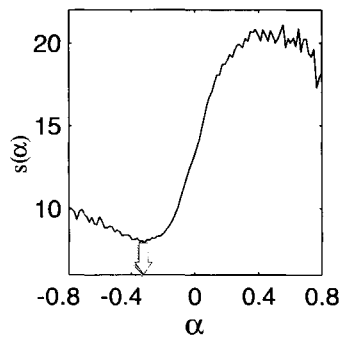

Figure 3.8: *Graph of the standard deviation $s(\alpha)$ of multiscale reflection amplitudes of Fig. 3.7f along analytical contours. A minimum is found at $\alpha = -0.34$.*

tor in Fig. 3.7a,d. For this reflector, the modulus maxima plane is computed, and the contours of constant amplitude on this plane are drawn in Fig. 3.7f. We see that the general behavior of these J-shaped contours is similar to the contours drawn in Fig. 3.5d. It is therefore already clear that we have recovered the fact that we are dealing with a negative singularity exponent α. The result of applying the contour matching algorithm of Subsection 3.3.4 is shown in Fig. 3.8. Although the minimum is not as pronounced as in Fig. 3.6, we can find an estimate for the singularity parameter at $\alpha = -0.34$. Note that this corresponds very well to the value obtained directly from the well-log ($\alpha = -0.32$).

Figure 3.9 shows a similar example, but this time the analyzed reflector in Fig. 3.9a at $z = 170$m (denoted by the black arrow) clearly resembles a stepfunction. This well-log was made available by Shell. The result of applying the multiscale analysis gave an estimate of the singularity parameter at $\alpha = -0.01$, as can be visually checked in Fig. 3.9c. Again seismic reflection data were modeled, taking the density at $\rho = 2000\text{kg/m}^3$. The reflection, identified to match the reflector indicated in Fig. 3.9a,d is depicted in Fig. 3.9e. From this reflection the amplitudes in the modulus maxima plane were acquired; the contours are drawn in Fig. 3.9f. The contours in Fig. 3.9f show that for this reflection there is hardly any scale-dependency, as we expect from the singularity parameter derived from the well-log ($\alpha = -0.01$). The application of the contour matching algorithm presented us with the standard deviations as shown in Fig. 3.10. A clear minimum is found at a

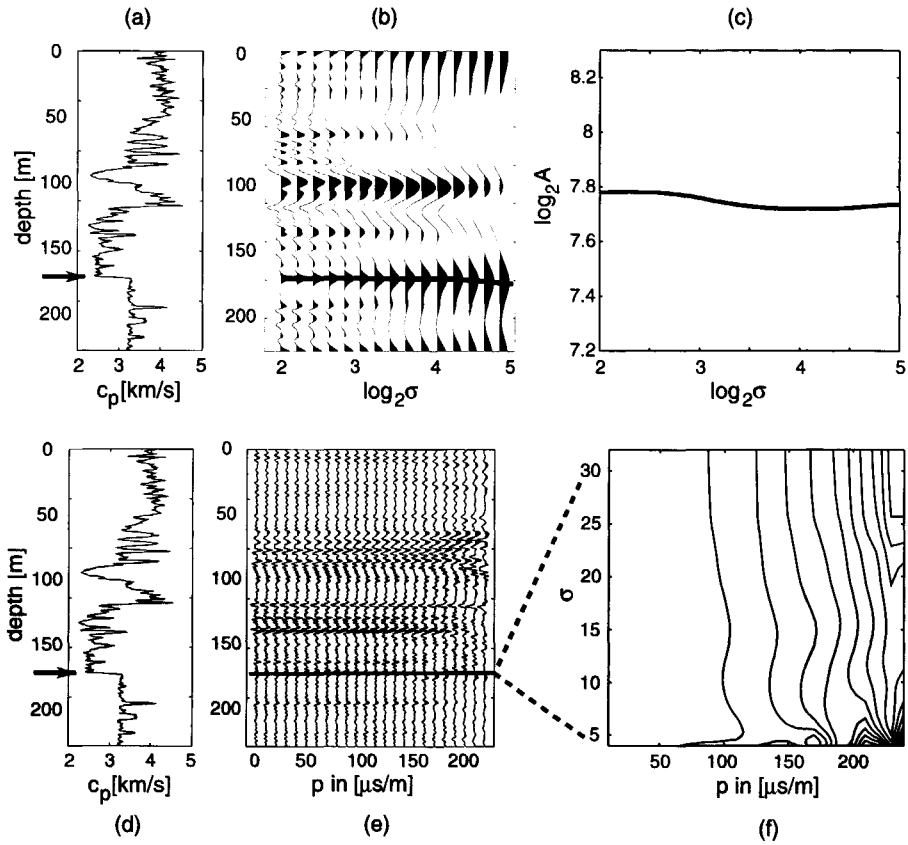

Figure 3.9: *(a,b,c) Multiscale analysis of a stepfunction in a well-log:* $\alpha = -0.01$. *(d,e,f) Multiangle, multiscale analysis of its seismic response:* $\alpha = -0.03$.

singularity parameter $\alpha = -0.03$. Just as in the first example, this corresponds very well to the estimate of the singularity parameter from the well-log ($\alpha = -0.01$).

We have shown that the inversion for the singularity parameter α is stable, when applied to synthetic data, modeled in real well-logs. Although the derived contours of constant multiscale reflection amplitudes are quite strongly affected by surrounding events in the imaged seismic data, the recovered singularity parameters α from the seismic reflection data are consistent with the singularity parameters derived from the well-logs.

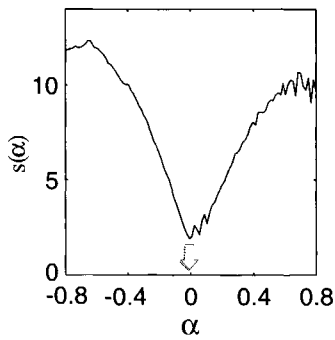

Figure 3.10: *Graph of the standard deviation $s(\alpha)$ of multiscale reflection amplitudes of Fig. 3.9f along analytical contours. A minimum is found at $\alpha = -0.03$.*

3.5 The normal incidence reflection coefficient of a singular interface

In Wapenaar (1999), a derivation is given for the normal incidence reflection and transmission coefficients $R^{-,+}$ and $T^{-,+}$ of the singular velocity model, described by,

$$c(z) = \begin{cases} c_1 |z/z_1|^\alpha & \text{for } z < 0 \\ c_2 |z/z_1|^\alpha & \text{for } z > 0. \end{cases} \tag{3.18}$$

In this section, the analytical expression for the normal incidence reflection coefficient for the downgoing wave field R^+ is analyzed for its dependency on the parameters c_1, c_2 and α. The expression for this reflection coefficient, as derived by Wapenaar (1999), is given by

$$R^+ = j \left[\frac{e^{-j\nu\pi} \rho_2 c_2^{2\nu} + e^{j\nu\pi} \rho_1 c_1^{2\nu}}{\rho_2 c_2^{2\nu} + \rho_1 c_1^{2\nu}} \right], \tag{3.19}$$

in which

$$\nu = 1/(2 - 2\alpha). \tag{3.20}$$

Note that eq. (3.19) is only valid for the positive angular frequencies ($\omega > 0$). The reflection coefficient for the negative frequencies follows from applying

the relations in Chapter 2, Section 2.2.2. However, in the remainder of this chapter we assume that all angular frequencies ω are positive, which simplifies the expressions.

We can check whether eq. (3.19) is a generalization of the conventional expression for the normal incidence reflection coefficient of a stepfunction, by taking $\alpha = 0$. It is easily verified that for stepfunctions, eq. (3.19) reduces to

$$R^+(\alpha = 0) = \frac{\rho_2 c_2 - \rho_1 c_1}{\rho_2 c_2 + \rho_1 c_1}, \tag{3.21}$$

which is the well-known normal incidence reflection coefficient of the boundary between two halfspaces.

To properly analyze the effect of the parameters c_1, c_2 and α on the reflection coefficient r^+, we take $\rho_1 = \rho_2$ (no density contrast) and decompose eq. (3.19) into a real and an imaginary part, according to

$$R^+ = \sin \nu\pi \left[\frac{1 - \eta^{2\nu}}{1 + \eta^{2\nu}}\right] + j \cos \nu\pi, \tag{3.22}$$

where

$$\eta = \frac{c_1}{c_2}. \tag{3.23}$$

As we can see from eq. (3.22), the dependency of the reflection coefficient R^+ on the velocities c_1 and c_2 is not explicit; only the ratio of c_1 by c_2 is present in the expression. This ratio (η) will be referred to as the *velocity contrast ratio*.

An interesting form of eq. (3.19) is acquired when we take $\eta = 1$

$$R^+ = j \cos \nu\pi. \tag{3.24}$$

Equation (3.24) shows that the reflection at a singular velocity field is identical to applying a Hilbert transformation to the incident wave field [cf. Chapter 2, Section 2.2.4] and multiplying this by $-\cos \nu\pi$. For $\alpha < 0$ this factor is negative, for $0 < \alpha \leq \frac{1}{2}$ it is positive. For $\alpha = \frac{1}{2}$ the factor is 1, such that the reflected wave field is identical to the Hilbert transform of the incident wave field.

3.6 Instantaneous phase analysis

When a seismic wave is emitted from a source, the amplitude spectrum and the phase of the emitted wavelet are important parameters that should be known to perform further processing and characterization of the seismic data.

When we assume that the estimate of the incident wave field is correct, there is the possibility of performing a quantitative characterization of both the amplitudes and the phase of a reflection event, and compare it with the incident wave field. The method that is treated in this section is concerned with the phase of the different reflection events and shows how measurements of instantaneous phase can be used in seismic characterization.

In section 3.5, an expression for the normal incidence reflection coefficient of a singular interface was introduced [eq. (3.22)]. From this equation, we can see that for $\alpha \neq 0$, the reflection coefficient is complex, which means that the reflected wave field contains a phase shift. In this section, it will be shown how to extract the phase shift of a specific reflection event in a seismic measurement. This phase shift is generally referred to as the *instantaneous phase* of a seismic reflection event.

The concept of instantaneous phase was introduced in the geophysics community by Taner *et al.* (1979) as a tool for attribute analysis in seismic characterization. Taner *et al.* (1979) argue that the instantaneous phase emphasizes the coherency of reflection events. From this observation, it can be concluded that the phase shift measured by this technique is related to lateral consistency of reflective behavior of an interface. However, Taner *et al.* (1979) do not explicitly treat models or give reasons that could account for the difference in instantaneous phases between separate reflectors.

A quantitative explanation for phase shifts of reflection events has first been given by Widess (1973). Widess analyzes the reflectivity of a progressively thinner high velocity layer, in which the bed below and above this layer have the same velocity. The density is assumed to be constant. In this analysis it was assumed that the reflective behavior of an incident wave could be characterized by its predominant wavelength λ_{eff} *within* the thin bed. It was shown that the reflection of a bed with thicknesses $d \lesssim \lambda_{\text{eff}}/8$ is almost identical to applying a first order differential operator to the incident wave field.

Figure 3.11 is a modified version of Fig. 1 in Widess (1973), showing the reflective behavior for a bed thickness of $d = \lambda_{\text{eff}}/8$. Figure 3.11a shows the reflection at the top interface in Fig. 3.11c and d, denoted by $u_1(t)$, by a solid

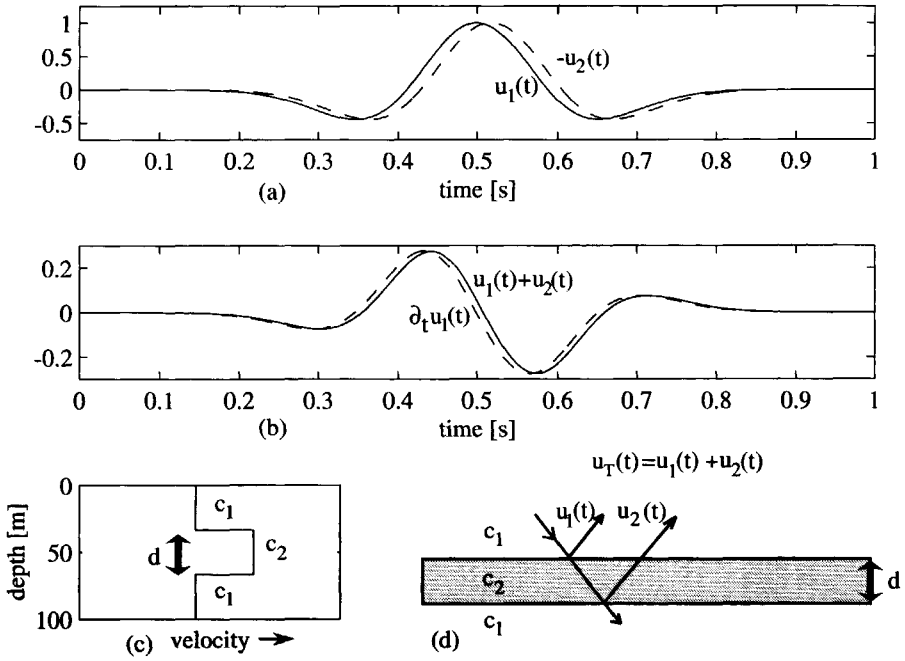

Figure 3.11: *(a) reflections $u_1(t)$ (solid) and -$u_2(t)$ (dashed) as denoted in (d). (b) total reflection $u_T(t) = u_1(t) + u_2(t)$ (solid), and the time-derivative of $u_1(t)$ (dashed), which is scaled by a constant factor, to match the amplitude of $u_T(t)$. (c) velocity graph of the thin layer. (d) reflection ray diagram. [after Widess (1973)]*

line. The time-delayed reflection at the bottom interface is displayed by a dashed line.

It is clear from Fig. 3.11 that the reflected wave field $u_T(t)$ shows a striking resemblance with the time derivative of $u_1(t)$. This shows graphically that a thin layer acts as a differential operator on the incident wave field.

This effect can also be made quantitative by studying the experiment analytically. We define a wave field $u(t)$, incident on the thin layer of Fig. 3.11d. The wave field reflected at the top interface is then given by $u_1(t) = u(t)$, the reflected wave field at the bottom interface by $u_2(t) = -u(t - \Delta t)$, where Δt is the time delay due to the propagation in the fine layer. Therefore, the resulting total reflected wave field, when transmission effects and internal

multiples are neglected, is given by

$$\begin{aligned} u_T(t) &= u_1(t) + u_2(t) \\ &= u(t) - u(t - \Delta t). \end{aligned} \tag{3.25}$$

From basic calculus we know that,

$$u(t) - u(t - \Delta t) = \Delta t \, \frac{d}{dt} u(t), \quad \text{for } \Delta t \to 0. \tag{3.26}$$

From eqs. (3.25) and (3.26) we see that $u_T(t)$ behaves similar to the first derivative of the incident wave field $u(t)$. Due to the fact that the high velocity layer can not be infinitely thin, Δt in eq. (3.25) does not go to the zero limit. Therefore, we see that because Δt keeps a value, we can quantify the scaling term as used in Fig. 3.11b as being Δt.

The most important effect of a thin layer is that the reflected wave field contains a phase shift. In general, the phase shift of a seismic event can by quantified by means of the technique of instantaneous phase analysis [Taner *et al.* (1979)]. The technique computes the instantaneous phase φ_{inst} of an event as follows

$$\varphi_{\text{inst}} = \tan^{-1} \frac{\{\mathcal{H}f\}(t_{\max})}{f(t_{\max})}, \tag{3.27}$$

where $t_{\max}$ is the point where the envelope of the analytical signal reaches a local maximum. $\{\mathcal{H}.\}$ is the Hilbert transform, as defined in Chapter 2, Section 2.2.4.

There exist other techniques for instantaneous phase estimation. E.g., the *matching pursuit approach*, proposed by Mallat and Zhang (1993), is more stable in the presence of noise and near-interfering events. Verhelst (2000) has used this technique for the characterization of local wavelet shapes. In this thesis however, the technique of Taner *et al.* (1979) has been given the preference for its simplicity.

Applying this technique to the reflection at the thin layer, denoted by $u_T(t)$ and shown in Fig. 3.11, shows that its instantaneous phase is given by $\varphi_{\text{inst}} = 90°$. Note that the incident wavefield is described by a Ricker wavelet, which is a zero-phase wavelet. When we compare this with eq. (3.22), this is similar to taking the velocity contrast ratio $\eta = 1$ and the singularity parameter $\alpha < 0$, which would also give an instantaneous phase $\varphi_{\text{inst}} = 90°$.

We recall eq. (2.12) in Chapter 2, which states that a differentiation of a function in the time domain forms a Fourier pair with the multiplication by

$j\omega$ of this function in the frequency domain, i.e.

$$\frac{\partial f(t)}{\partial t} \leftrightarrow j\omega F(\omega). \tag{3.28}$$

Now we compare eq. (3.28) with with the Fourier pair of the Hilbert transform, given by

$$-\{\mathcal{H}f(t)\} \leftrightarrow jF(\omega). \tag{3.29}$$

We note that where the thin layer performs an approximate differentiation (multiplication with $j\omega$ in the frequency domain), the singular velocity model, for $\eta = 1$, performs a Hilbert transformation and multiplies by $-\cos \nu\pi$ (multiplication with $j \cos \nu\pi$ in the frequency domain). Hence, the normal incidence response of a thin layer is frequency dependent, whereas the normal incidence response of the singular velocity model is scale independent. On the other hand, the resemblance of the phase factor in eqs. (3.28) and (3.29) in the frequency domain is an explanation for the fact that the reflection responses of a thin layer and the reflection response of the singular velocity model described by eq. (3.1) are quite similar.

Accordingly, both models can explain a phase shift of $\pm 90°$ in reflection data. However, the singular velocity model is more consistent with the finding of Herrmann (1997) that well-logs exhibit local self-similar behavior, than the model by Widess.

We now further analyze the effect of the singularity parameter α and the velocity contrast ratio η on the instantaneous phase of the reflection response of the singular velocity model. First we analyze the effect of the singularity parameter α on the normal incidence reflectivity by taking the velocity contrast ratio fixed at $\eta = \frac{1}{2}$. Note that this analysis is similar to the technique of Dessing (1997), who recovers the so-called $(\varphi_{\text{inst}}, \alpha)$-diamonds from one-sided singular velocity models. Figure 3.12a shows singular velocity models for a range of singularity parameters α. Figure 3.12b shows the normal incidence reflection responses for these singular velocity models. For clarity, the responses are convolved with a Ricker wavelet. A clear phase shift is visible as a function of the singularity parameter α. This phase shift is now quantified by means of the above instantaneous phase analysis. Figure 3.12c shows the course of the instantaneous phase as a function of singularity parameter. We see that within the range of $\alpha \in [-1, .5]$ the instantaneous phase changes a full $180°$.

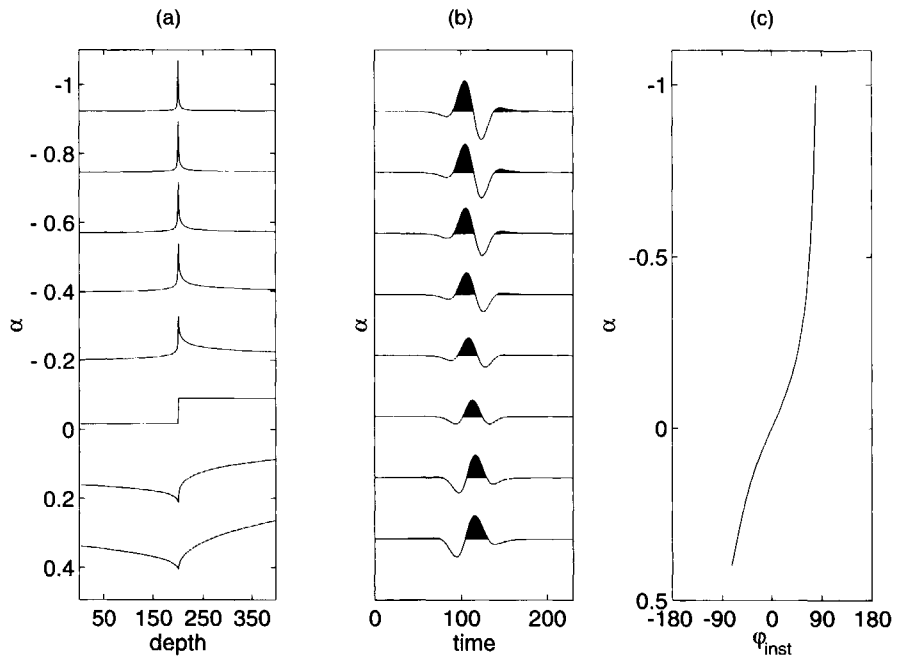

Figure 3.12: *Instantaneous phase as a function of α.*
(a) Velocity functions as a function of singularity parameter α, with velocity contrast ratio $\eta = \frac{1}{2}$. (b) Normal incidence reflection response (convolved with a Ricker wavelet) on these velocity functions. (c) The instantaneous phase as a function of α.

A similar analysis is performed to visualize the effect of the velocity contrast ratio η on the instantaneous phase of the normal incidence reflection response, with the singularity parameter fixed at $\alpha = -0.4$. Figure 3.13a shows again the singular velocity models, but now for a range of the velocity contrast parameter $\eta \in [0.2, 2]$. The reflection responses are depicted in Fig. 3.13b, where again there is a strong effect on the phase of the reflectivity visible. Figure 3.13c shows that for this range of η, the phase changes from approximately 45° to 135°.

In a further analysis, we can check the dependency of the instantaneous phase on the angle of incidence of the incident wave field. As we do not have an explicit expression for the rayparameter-dependent reflectivity of the singular velocity models, this must be checked numerically. To this end, data are

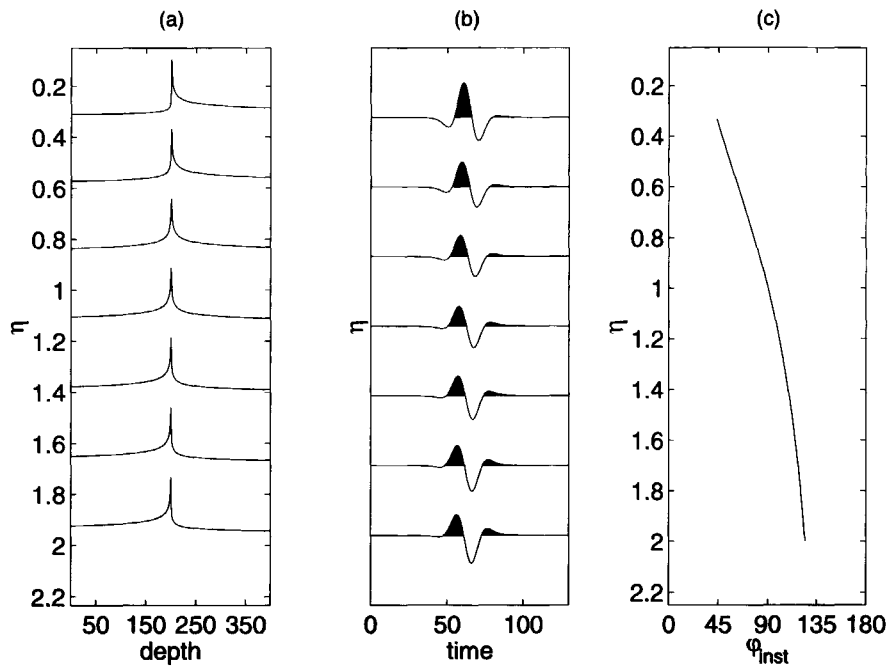

Figure 3.13: *Instantaneous phase as a function of η.*
(a) Velocity functions as a function of η, with α=-0.4. (b) Normal incidence reflection response (convolved with a Ricker wavelet) on these velocity functions. (c) The instantaneous phase as a function of η.

modeled in singular velocity models described by eq. (3.1). Both the singularity parameter α and the velocity contrast ratio η are varied. These angle-dependent data are then analyzed, for every rayparameter, by the instantaneous phase analysis. In this modeling, fixed values of $c_2 = 1200$ and $z_1 = 5$ m were chosen. The derived rayparameter-dependent instantaneous phases for $\alpha = -0.3, 0$ and $+0.3$ and $\eta = 0.5, 1$ and 2 can be found in Fig. 3.14a-c. The figure shows that the phase of the reflection response is almost constant along the rayparameter (p) values, for fixed singularity parameter α and velocity contrast ratio η. Note that in Fig. 3.14b the phase for $\eta = 0.5$ is only constant up to the critical reflection angle, which is about 8×10^{-4} s/m. Beyond this point the phase will gradually change to a value of 180 degrees, which is the standard post-critical behavior of the reflectivity of stepfunction interfaces.

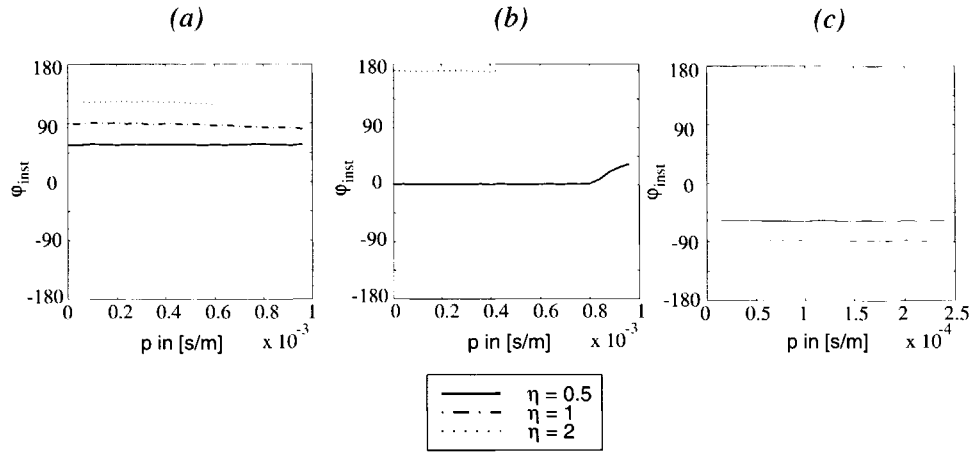

Figure 3.14: *Instantaneous phase φ_{inst} as a function of rayparameter p, for $\eta \in [0.5, 1, 2]$ where the singularity parameter $\alpha = -0.3$ (a), $\alpha = 0$ (b) and $\alpha = 0.3$ (c).*

3.7 Inversion for contrast and singularity parameter

We have seen that both the rayparameter dependent amplitudes in the modulus maxima planes and the instantaneous phase of the reflectivity are strongly dependent on the singularity parameter α and the velocity contrast ratio η. The implicit formula for the contours describing the constant reflection amplitudes [eq. (3.12)] does not contain a reference to the velocity parameters c_1 and c_2. Using the results of Section 3.3 and Section 3.6, we propose a one-step inversion scheme to estimate the parameters α and η for a specific reflector from the rayparameter-dependent reflection response.

Referring to Menke (1984), the general expression for linearized damped least-squares inversion is given by

$$\delta\mathbf{m} \approx (\mathbf{J}^T\mathbf{J} + \epsilon\mathbf{I})^{-1}\mathbf{J}^T\delta\mathbf{d}. \tag{3.30}$$

This is generally referred to as Gauss-Newton inversion. In this equation, $\delta\mathbf{m}$ is the update to the model vector $\mathbf{m} = (\alpha, \eta)^T$ and $\delta\mathbf{d}$ is the misfit between the modeled and the measured data. This misfit is quantified by a penalty function E that is a combination of the misfit of the rayparameter dependent

amplitudes in the modulus maxima planes and of the misfit of the instantaneous phase. The Jacobian **J** is defined as $\frac{\delta \mathbf{d}}{\delta \mathbf{m}}$, and is acquired by modeling data for perturbations of the starting model. We note the presence of the parameter ϵ, which is used to damp the inversion. The value of this parameter is decreased when the update to the model gives too small an improvement to the modeled data, where the parameter is increased when the update to the model results in an increase of the value of the penalty function E. The inversion scheme is continued until the penalty function E has reached a smaller value than a certain stop criterion.

To analyze whether the singularity parameter α and the velocity contrast ratio η are resolvable from the imaged angle-dependent reflectivity, the following steps must be taken. First, a penalty function is defined on the basis of the amplitudes in modulus maxima planes and the instantaneous phase. Second, this penalty function is analyzed for the shape of its error surface, i.e. whether the minimum is unique and well-defined. After this analysis, the stop criterion can be defined. Finally, the above Gauss-Newton inversion procedure is applied to a synthetic data set, to assess its performance. In the following two subsections the above steps are covered.

3.7.1 Creation of the penalty function in inversion for singularity parameter and velocity contrast ratio

The contours of constant reflection amplitude in the modulus maxima planes in figures 3.7f and 3.9f show that there are some areas where the contours seem to be very stable and some areas where the contours are strongly affected by noise or interference with other events. Therefore, for both the penalty function for the multiscale amplitudes E_A and the penalty function for the instantaneous phases $\mathrm{E}_{\varphi_{\mathrm{inst}}}$, we choose an expression that does not emphasize on outliers or bad measurements in the data. A stable choice is then to take the ℓ_1-norm of the difference between data and modeled data

$$\mathrm{E}_A = \frac{1}{N} \sum_{i=1}^{N} |A_i^d - A_i^m|, \tag{3.31}$$

in which A^d are the amplitudes measured in de modulus maxima plane of the data we want to analyze and $N = N_\sigma \times N_p$ is the number of sample points in these planes. A^m are the amplitudes in the modulus maxima plane from the modeled data and are found by creating a synthetic velocity model,

modeling reflection data in it and creating the modulus maxima plane for these data.

For the instantaneous phase φ_{inst} it was shown (Fig. 3.14), that the phase is almost constant for all rayparameter-values, as long as we are in the subcritical reflection domain. So for this penalty function, a logical choice would be to take the absolute difference between the phase of the measured data and the modelled data, according to

$$\mathrm{E}_{\varphi_{\text{inst}}} = |\bar{\varphi}^{d}_{\text{inst}} - \bar{\varphi}^{m}_{\text{inst}}|, \tag{3.32}$$

in which $\bar{\varphi}_{\text{inst}}$ is the mean of the instantaneous phases for all subcritical rayparameter values. Namely, when we take the mean of the phases, a wrong value of the instantaneous phase for one p-value is (partially) cancelled. A weighted sum of these two penalty functions form the total penalty function E, according to

$$\mathrm{E} = \frac{1}{W}\mathrm{E}_{\varphi_{\text{inst}}} + \mathrm{E}_A \tag{3.33}$$

W is the weight factor and it must be chosen such that the total penalty function E has a balanced sensitivity to both the errors in multiscale reflection amplitudes and the instantaneous phases. This weight factor W can be found by trial-and-error, using an inversion problem on reflection data, for which we already know the solutions α_{opt} and η_{opt}. It turned out, empirically, that when the instantaneous phase φ_{inst} is measured in radians a good estimate for the weighting factor is $W=1$.

To test the quality of the defined penalty functions, two synthetic examples are created. A data set of rayparameter-dependent reflectivity is generated on a reflector model described by eq. (3.1). This data set is referred to as the measured data. Then, for a range of singularity parameters α and velocity contrast ratios η, similar data sets are generated. For all these data, the penalty functions E_A, $\mathrm{E}_{\varphi_{\text{inst}}}$ and E are computed, and are analyzed for their shape and how well they perform in resolving the singularity parameter α and the velocity contrast ratio η. This type of analysis shows whether the penalty functions contain local minima or not. If local minima are present, this would seriously trouble the inversion.

The first example treats the penalty functions for a stepfunction interface ($\alpha = 0$), where the velocity contrast ratio was set at $\eta = 0.5$. In this example, we assume that we know the background velocity parameter $c_1 = 1000$m/s. Figure 3.15 shows the gray-scale plots of the values of the penalty functions, as a function of α and η.

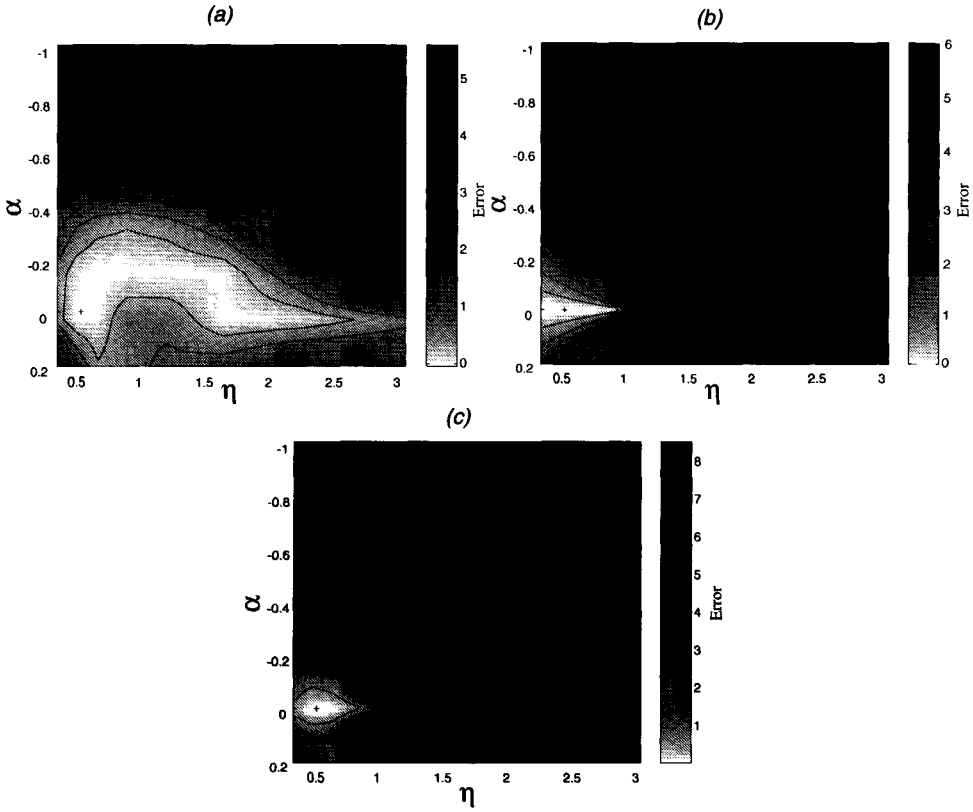

Figure 3.15: *(a) Penalty function for multiscale reflection amplitudes* E_A*, (b) Penalty function for instantaneous phase* $E_{\varphi_{inst}}$ *and (c) Total penalty function* E*, all for a stepfunction interface, with desired optimal solution* α*=0 and* η*=0.5, denoted by the* + *sign.*

It is clear that the total penalty function E in Fig. 3.15c is well able to resolve the parameters from the angle dependent reflectivity, as the minimum is pronounced and well-defined.

A similar example is generated for a singular reflector model, where the singularity parameter was chosen at $\alpha = -0.3$ and the velocity contrast ratio at $\eta = 1$. The velocity parameter c_1 is again assumed to be known and is $c_1 = 1000$m/s. The results of this analysis are depicted in Fig. 3.15. Again the total penalty function E shows a pronounced and unique minimum at the expected position.

An interesting aspect is recognized in Figs. 3.15ab and 3.16ab, namely

that the penalty functions E_A and $E_{\varphi_{inst}}$ have complementary resolving power. In neither of the examples is one of these penalty functions separately sufficient to derive both the velocity contrast ratio η as well as the singularity parameter α. Furthermore, from Figs. 3.16a,b, we see that to derive the velocity contrast ratio η from the angle-dependent reflectivity of a singularity with negative α, the instantaneous phase φ_{inst} is far more important than the multiscale reflection amplitudes. This behavior is completely different from the behavior of the angle-dependent reflectivity of stepfunction interfaces, in which the multiscale reflection amplitudes resolve primarily the velocity contrast ratio.

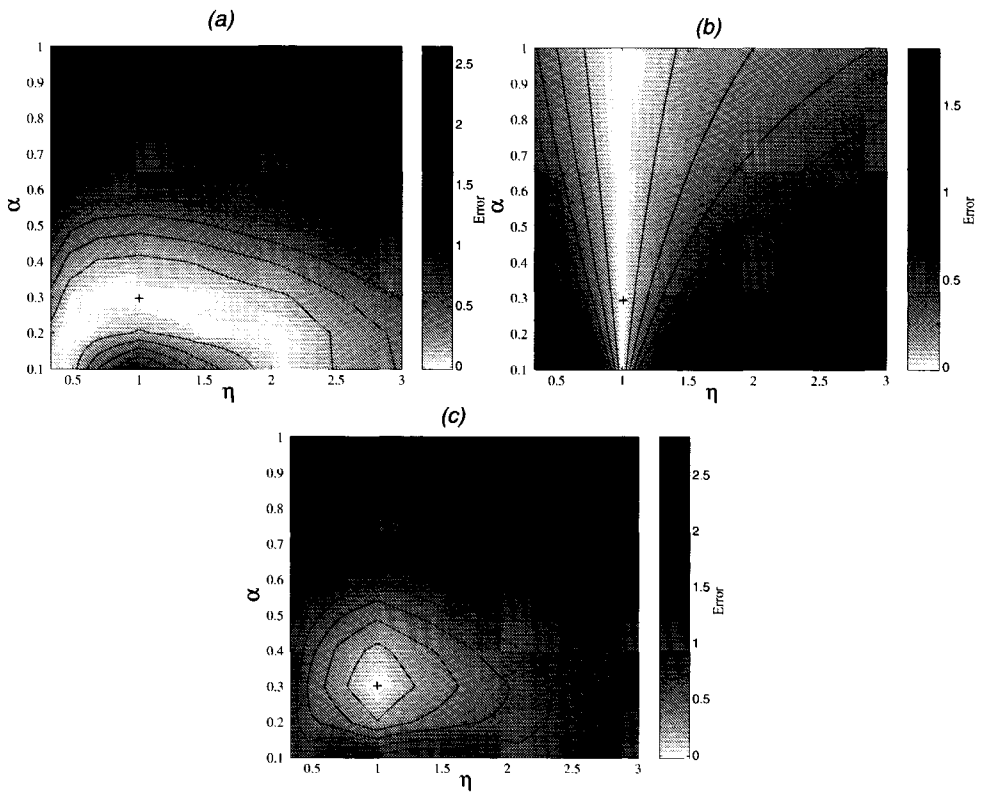

Figure 3.16: *(a) Penalty function for multiscale amplitudes* E_A*, (b) Penalty function for instantaneous phase* $E_{\varphi_{inst}}$ *and (c) Total penalty function* E*, all for a two-sided singularity model, with desired optimal solution* α*=-0.3 and* η*=1, denoted by the + sign.*

From this behavior we can conclude that the multiscale reflection amplitudes and the instantaneous phases are independent parameters, which must be both used for the characterization of seismic events, if we want to estimate both the singularity exponent α and the velocity contrast ratio η.

3.7.2 Gauss-Newton inversion to estimate the singularity parameter and the velocity contrast ratio

As we have seen in Figs. 3.15c and 3.16c the penalty function E is well defined, and approximately convex, so the use of a gradient method like Gauss-Newton is justified.

To illustrate the inversion for the singularity parameter α and the velocity contrast ratio η, an inversion on synthetic data is performed. The data to which the inversion is applied is the same as the one used to compute the penalty functions in Fig. 3.16 ($\alpha = -0.3$ and $\eta = 1$, $c_1 = 1000$ m/s). Choosing quite arbitrarily starting values of the model parameters $\alpha_0 = -0.6$ and $\eta_0 = 1.7$, the Gauss-Newton inversion scheme is applied.

Fig. 3.17 gives an overview of the behavior of this inversion. Figure 3.17a shows the value of the singularity parameter α for each inversion step, Fig. 3.17b the value for the velocity contrast function η. Figure 3.17c shows the decrease of the penalty function, only for the inversion steps where the update to the model parameter was accepted (i.e. where the value of the penalty function E had sufficiently decreased). Quite unexpectedly, only after 33 inversion steps, the value of the penalty function decreased to a value below the stop criterion.

We see in Fig. 3.17a that after 14 steps the singularity parameter α was resolved, however, the determination of the velocity contrast ratio turned out to be much more time consuming (cf. Fig. 3.17b). Because the convergence rate is very slow and due to the fact that for each inversion step a forward modeling must be performed, this inversion is not practically applicable to perform multiangle, multiscale analysis of seismic data. Further, field measurements are always affected by transmission and scattering losses, which are hard to measure or estimate. The penalty function for the multiscale amplitudes E_A is however based on true amplitudes, assuming that the losses are corrected for, such that this penalty function will be unreliable in practice.

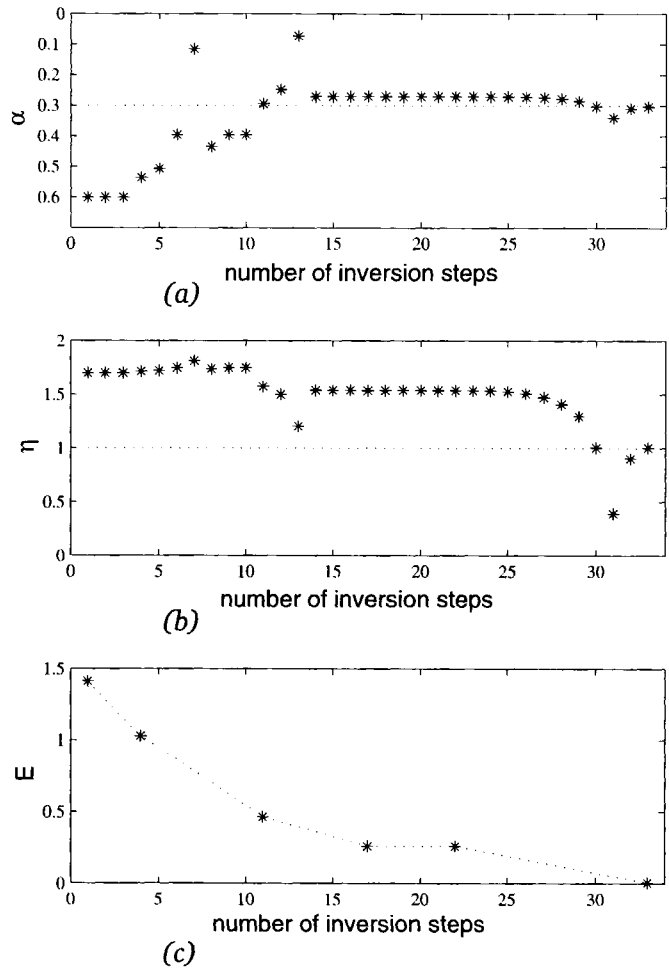

Figure 3.17: *(a) course of α as a function of the number of penalty function evaluations (b) course of η as a function of the number of penalty function evaluations (c) course of the penalty function* E *as a function of the number of penalty function evaluations.*

3.8 Conclusions

This chapter has given a framework for extracting a singularity parameter α from seismic reflection data by analyzing the contours of constant reflection amplitudes in modulus maxima planes. The application of this method to synthetic data, modeled in both synthetic and real well-logs, showed that an estimate of the singularity parameter α can be found that is consistent with the one derived from reflectors in these well-logs.

Furthermore, it was shown that the instantaneous phase of a specific reflection event contains information complimentary to the multiscale reflection amplitudes. This can be used to resolve both the singularity parameter α and a velocity contrast ratio η from seismic reflection data. A Gauss-Newton inversion scheme is proposed that is theoretically able to solve for these parameters using a penalty function based on a combination of these multiscale amplitudes and instantaneous phases. However, the rate of convergence of this inversion scheme is not sufficient for applying it to real data.

In the next chapter, an inversion scheme is proposed that is faster in convergence and more stable in the presence of noise than the inversion scheme proposed in this chapter.

Chapter 4

Multiscale characterization of velocity contrast functions

In this chapter, an alternative technique for multiangle, multiscale analysis of seismic reflection data is presented. This technique facilitates the analysis of both acoustic and elastic reflection data. To this end, the singular velocity model of Chapter 2, Section 2.8 is extended to an elastic parameterization. A two-step inversion scheme for estimating the singularity parameter α from seismic reflection data is presented, in which first velocity contrast functions are derived from reflectivity sections by Linearized Zoeppritz Inversion. These velocity contrast functions are then analyzed by a multiscale analysis, to acquire an estimate of the singularity parameter for every contrast.

4.1 Introduction

The direct inversion for both the singularity parameter α and the velocity contrast ratio η, as described in Chapter 3, Section 3.7, is strongly dependent on a consistent high quality of the seismic reflection data and their processing. Especially the constraint of a perfect deconvolution with the source wavelet is extremely difficult to fulfill in practice. The inversion method for the singularity parameter α, based on the contours of constant reflection amplitude in modulus maxima planes, suffers from the same problem. Furthermore, no closed-form implicit expression (such as in eq. (3.12)) for these contours in the elastic situation has been found.

In this chapter an alternative inversion technique for the determination of the singularity parameter α is proposed, which is less sensitive to the constraints on deconvolution and other processing. Contrary to the inversion methods of Chapter 3, this method can be used on acoustic as well as elastic

reflection data.

To this end, first an elastic singular velocity model is presented that is an extension of the acoustic singularity model in eq. (2.66) in Chapter 2.

On the basis of the above model, an inversion method is presented that consists of two steps. First, velocity contrast functions are derived from the seismic reflection data, using the method of Linearized Zoeppritz Inversion [Van Wijngaarden (1998)]. Second, the singularity parameters α is estimated from modified versions of these velocity contrasts. For this purpose the adapted form of the technique for retrieving the parameter α from well-logs (Chapter 2, Section 2.6) is applied.

4.2 An elastic singular velocity model

As is generally known, real seismic reflection data are more completely described by the elastic wave equation than by the acoustic wave equation, as the Earth behaves predominantly as an elastic medium. Therefore, in practice, pre-stack seismic characterization like AVO analysis is performed in either the elastic or poro-elastic approximation.

The singular velocity model described by eq. (2.66) is however an acoustic model. In this section, a parameterization of a singular elastic velocity model is proposed, that is an extension of this acoustic model. With this model, it is possible to perform a multiscale analysis of elastic velocity functions, similar to the technique described in Chapter 2, Section 2.6.

In this model, we define singularities in the P-wave velocity function $c_P(z)$ as (shifted versions of)

$$c_P(z) = \begin{cases} c_{P,1}|z/z_1|^{\alpha_P} & \text{for } z < 0 \\ c_{P,2}|z/z_1|^{\alpha_P} & \text{for } z > 0, \end{cases} \tag{4.1}$$

where α_P is the local P-wave singularity parameter. $c_{P,1}$ and $c_{P,2}$ are the P-wave velocities at $z = -z_1$ and $z = z_1$ respectively. Singularities in the S-wave velocity function are defined as (shifted versions of)

$$c_S(z) = \begin{cases} c_{S,1}|z/z_1|^{\alpha_S} & \text{for } z < 0 \\ c_{S,2}|z/z_1|^{\alpha_S} & \text{for } z > 0, \end{cases} \tag{4.2}$$

where α_S is the local S-wave singularity parameter. It is noted that these velocity functions obey the local scaling relations

$$c_P(\beta z) = \beta^{\alpha_P} c_P(z), \tag{4.3}$$

and

$$c_S(\beta z) = \beta^{\alpha_S} c_S(z), \tag{4.4}$$

similar to eq. (2.64). We assume this model for singularities in the P- and S-wave velocities in the remainder of this thesis.

4.3 Linearized Zoeppritz inversion

Explicit analytical expressions exist for the elastic rayparameter-dependent reflection coefficients. Knott (1899) was the first to derive an analytical expression for the reflection of ultrasound wave-packets. This formulation was subsequently refined for seismological use by Zoeppritz (1919). Zoeppritz's result, the Knott-Zoeppritz matrix equation, describes the rayparameter-dependent reflection coefficients of an elastic medium, at a boundary of two half spaces.

The elastic singular velocity model, described by eqs. (4.1) and (4.2) can be approximated by a superposition of stepfunction interfaces, as is described in Chapter 3, Section 3.1. Consequently, the reflectivity of these singular velocity models is approximated by a cascade of the reflection coefficients of these stepfunction interfaces.

Using the full Knott-Zoeppritz matrix equation, it is in principle possible to invert for the medium parameters from seismic reflection data. Unfortunately, this inversion is strongly non-linear, as there are many higher order coupled terms to take into account. The full matrix equation can however be linearized in such a way that it only describes the pre-critical parts of the rayparameter-dependent reflection coefficients. An example of such a linearization can be found in Aki and Richards (1980). By this linearization, the full Knott-Zoeppritz matrix equation reduces to a set of scalar expressions for the reflection coefficients, that contain only a small number of lower order terms. These expressions enable us to acquire an estimate of the medium parameters by inversion of the pre-critical seismic reflectivity.

4.3.1 Linearized P-P reflection coefficient

In Van Wijngaarden and Berkhout (1995) a modified version of the linearized expression of Aki and Richards (1980) for the rayparameter-dependent P-P reflection coefficient $\tilde{R}_{PP}(p)$ is presented. This linearization is written in terms of the following normalized contrasts of seismic parameters:

P-Wave velocity contrasts	$\Delta c_P/\bar{c}_P$,		
Impedance contrasts	$\Delta Z/\bar{Z}$,	and	(4.5)
Shear modulus contrasts	$\Delta\mu/\bar{\mu}$.		

At the boundary of two halfspaces, the overlined variables $\bar{c}_P$, $\bar{Z}$ and $\bar{\mu}$ are defined as the means of the P-wave velocity, the impedance and the shear modulus over the boundary, respectively.

The linearized Zoeppritz equation for the rayparameter-dependent reflection coefficient $\tilde{R}_{PP}(p)$ in terms of potentials, expressed in the above contrasts, is given by

$$\tilde{R}_{PP}(p) \approx \frac{1}{2}\frac{\Delta Z}{\bar{Z}} + \frac{1}{2}\left(\frac{\bar{c}_P^2 p^2}{1-\bar{c}_P^2 p^2}\right)\frac{\Delta c_P}{\bar{c}_P} - 2\bar{c}_S^2 p^2 \frac{\Delta\mu}{\bar{\mu}}, \tag{4.6}$$

which, when $\left[1-\bar{c}_P^2 p^2\right]^{-1}$ is approximated by 1 (a zeroth order series truncation), becomes

$$\tilde{R}_{PP}(p) \approx \frac{1}{2}\frac{\Delta Z}{\bar{Z}} + \left[\frac{1}{2}\frac{\Delta c_P}{\bar{c}_P} - 2\left(\frac{\bar{c}_S}{\bar{c}_P}\right)^2 \frac{\Delta\mu}{\bar{\mu}}\right]\bar{c}_P^2 p^2. \tag{4.7}$$

Due to the linearization and the above series truncation, eq. (4.7) is only valid for $\bar{c}_P^2 p^2 \ll 1$, so only small angles of incidence are taken into account. In practice, these angles of incidence are limited to approximately 30 degrees [Van Wijngaarden and Berkhout (1995)]. It is shown by De Haas (1992) that the above relation is also valid for the rayparameter-dependent reflection coefficient in terms of particle displacements.

From eq. (4.7) it can be seen that the normal incidence reflectivity gives the estimate of the impedance contrast. The rayparameter-dependent P-P reflectivity $\tilde{R}_{PP}$ gives, for small values of $\bar{c}_P^2 p^2$, the combined estimate of the P-wave velocity contrast and the shear modulus contrast. Note that an a priori model for the relation between the P-wave velocity c_P and the shear modulus μ has to be specified, to decouple these contrasts.

The acoustic rayparameter-dependent reflection coefficient $\tilde{R}(p)$ is acquired from eq. (4.7) by taking $\bar{c}_S = 0$, from which follows

$$\tilde{R}(p) \approx \frac{1}{2}\frac{\Delta Z}{\bar{Z}} + \frac{1}{2}\frac{\Delta c_P}{\bar{c}_P}\bar{c}_P^2 p^2. \tag{4.8}$$

4.3.2 Linearized SV-SV reflection coefficient

Equally well, linearized S-wave reflection coefficients can be derived. This subsection covers the reflection of a vertically polarized SV-wave on an elastic boundary. We only consider the rayparameter-dependent SV-SV-reflectivity. Mode conversions to P-waves are not covered.

Again referring to Van Wijngaarden (1998), the linearized Zoeppritz equation for $\tilde{R}_{SV,SV}(p)$ in terms of potentials, is given by

$$\tilde{R}_{SV,SV}(p) \approx \frac{1}{2}\frac{\Delta\rho}{\bar{\rho}} + \frac{1}{2}\left(\frac{1}{1-\bar{c}_S^2 p^2}\right)\frac{\Delta c_S}{\bar{c}_S} - 2\bar{c}_S^2 p^2 \frac{\Delta\mu}{\bar{\mu}}, \tag{4.9}$$

where $\Delta\rho/\bar{\rho}$ is the (normalized) density contrast. We now substitute for the contrast of the shear modulus μ

$$\frac{\Delta\mu}{\bar{\mu}} \approx 2\frac{\Delta c_S}{\bar{c}_S} + \frac{\Delta\rho}{\bar{\rho}}. \tag{4.10}$$

The series expansion of eq. (4.9) onto $\bar{c}_S^2 p^2$, dropping all terms with powers of p larger than 2, leads to

$$\tilde{R}_{SV,SV}(p) \approx \frac{1}{2}\left[\frac{\Delta c_S}{\bar{c}_S} + \frac{\Delta\rho}{\bar{\rho}}\right] - \left[\frac{7}{2}\frac{\Delta c_S}{\bar{c}_S} + 2\frac{\Delta\rho}{\bar{\rho}}\right]\bar{c}_S^2 p^2. \tag{4.11}$$

When we substitute for the contrast of the S-wave impedance Z_S

$$\frac{\Delta Z_S}{\bar{Z}_S} \approx \frac{\Delta c_S}{\bar{c}_S} + \frac{\Delta\rho}{\bar{\rho}}, \tag{4.12}$$

we arrive at the following linearized expression for the vertically polarized S-wave reflection coefficient $\tilde{R}_{SV,SV}(p)$

$$\tilde{R}_{SV,SV}(p) \approx \frac{1}{2}\frac{\Delta Z_S}{\bar{Z}_S} - \left[\frac{3}{2}\frac{\Delta c_S}{\bar{c}_S} + 2\frac{\Delta Z_S}{\bar{Z}_S}\right]\bar{c}_S^2 p^2. \tag{4.13}$$

To acquire the rayparameter-dependent reflection coefficient $\tilde{R}_{SV,SV}(p)$ in terms of particle displacements, we substitute $\tilde{R}_{SV,SV}(p) \rightarrow -\tilde{R}_{SV,SV}(p)$, as is shown by De Haas (1992). Similar to the linearized expression of the rayparameter-dependent P-P reflection coefficient, this expression is only valid for small values of $\bar{c}_S^2 p^2$. Comparing eq. (4.13) with eq. (4.7), we see that, contrary to the P-wave velocity contrast, the S-wave velocity contrast can be solved for independently. Namely, first the S-wave impedance contrast is derived from the normal incidence reflectivity. Second, using this estimate of the S-wave impedance contrast, the S-wave velocity contrast follows from the $\bar{c}_S^2 p^2$-dependent term.

4.3.3 Linearized SH-SH reflection coefficient

For a horizontally polarized SH-wave, the SH-SH reflection coefficient is fully decoupled from the SV-SV and P-P reflection coefficients [e.g. Aki and Richards (1980)].

The linearized expression for the rayparameter-dependent SH-SH reflection coefficient $\tilde{R}_{SH,SH}(p)$ in terms of potentials is given by [cf. Rüger (1996)],

$$\tilde{R}_{SH,SH}(p) \approx \frac{1}{2}\frac{\Delta Z_S}{\bar{Z}_S} - \frac{1}{2}\left(\frac{\bar{c}_S^2 p^2}{1-\bar{c}_S^2 p^2}\right)\frac{\Delta c_S}{\bar{c}_S}, \tag{4.14}$$

which, when $\left[1-\bar{c}_S^2 p^2\right]^{-1}$ is approximated by 1, becomes

$$\tilde{R}_{SH,SH}(p) \approx \frac{1}{2}\frac{\Delta Z_S}{\bar{Z}_S} - \frac{1}{2}\frac{\Delta c_S}{\bar{c}_S}\bar{c}_S^2 p^2. \tag{4.15}$$

Similar to the SV-SV case, the reflection coefficient in terms of particle displacements is acquired by substituting $\tilde{R}_{SH,SH}(p) \rightarrow -\tilde{R}_{SH,SH}(p)$. In eq. (4.15) we observe that the S-wave impedance contrast and the S-wave velocity contrast are fully decoupled. Note the similarity of eq. (4.15) with the linearized rayparameter-dependent acoustic reflection coefficient $R(p)$ in eq. (4.8).

4.3.4 Linearized Zoeppritz Inversion

In Van Wijngaarden (1998) it is shown that the contrasts in eq. (4.5) can be recovered from seismic reflection data, by means of *Linearized Zoeppritz Inversion* (LZI). To this end, first images of the rayparameter-dependent reflectivity are generated, according to the method described in Chapter 3, Subsection 3.3.2. These images can be looked upon as cascades of rayparameter-dependent reflection coefficients. Hence, the linearized Zoeppritz equation, governing the data type under consideration, can be solved at a specific imaging depth to acquire estimates of the parameter contrasts at that depth.

As an example, Fig. 4.1 shows how the inversion for the contrasts is performed on a rayparameter-dependent P-P reflection coefficient. The figure shows that the intercept with the vertical axis gives the estimate of the impedance contrast. The rayparameter-dependent P-P reflectivity $\tilde{R}_{PP}$ in eq. (4.7) gives, for small values of $\bar{c}_P^2 p^2$, the combined estimate of the P-wave velocity contrast and the shear modulus contrast, by means of the slope along

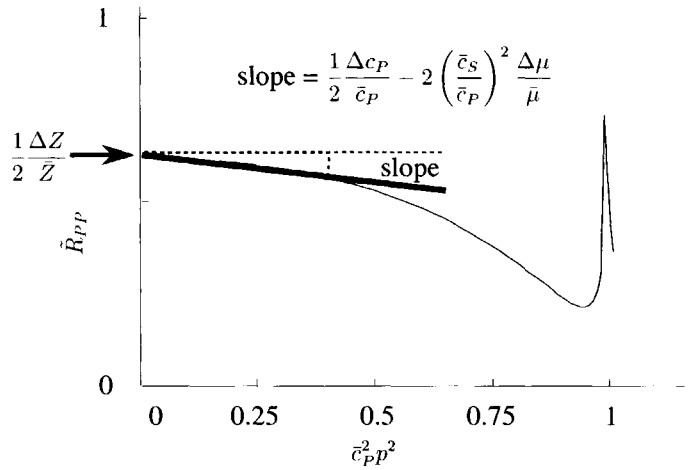

Figure 4.1: *A rayparameter-dependent P-P reflection coefficient. Note that the horizontal axis is $\bar{c}_P^2 p^2$. Referring to eq. (4.7), the intercept with the vertical axis gives the estimate for the impedance contrast, the slope of the thick black line gives a combined estimate for the P-wave velocity contrast and the shear modulus contrast.*

the depicted thick black line. In a similar way, this inversion can be applied to the rayparameter-dependent SV-SV and SH-SH reflectivities.

Linearized Zoeppritz Inversion (LZI) is now defined as solving the linearized Zoeppritz equation at every imaging depth separately. The results of applying LZI to a rayparameter-dependent reflectivity image are continuous estimates of the contrasts as a function of depth. In this thesis we refer to these results to as *contrast functions*. In this inversion, we assume that smoothed versions of the actual functions $c_P(z)$, $Z(z)$ and $\mu(z)$ are sufficient approximations of the functions $\bar{c}_P(z)$, $\bar{Z}(z)$ and $\bar{\mu}(z)$, respectively.

In Van Wijngaarden (1998) an analysis is performed on the influence of errors in the value of the background P-wave velocity $\bar{c}_P$ on the estimates of these contrasts. It was shown that especially the estimate of the shear modulus contrast is affected by errors in this background function; the P-wave velocity contrast function is affected in a lesser degree, the impedance contrast is not affected, as it is estimated independently from the background function of the P-wave velocity [cf. eq. (4.7)].

LZI is applied to field data in Chapter 5 and 6, to construct the velocity contrast functions from P-P and SH-SH-wave reflection data, respectively.

4.4 Multiscale analysis of velocity contrast functions

The foregoing section has given a framework for deriving P- and S-wave velocity contrast functions $\Delta c_P(z)/\bar{c}_P(z)$ and $\Delta c_S(z)/\bar{c}_S(z)$ from imaged angle-dependent reflectivity gathers. In this section, a method is presented for deriving the singularity exponent α from these velocity contrast functions. The derivation presented is valid for singularities in both P- and S-wave velocity functions, therefore the dependence of the contrast functions and the singularity exponent on either P or S is dropped.

When we perform multiscale inversion on well-logs, as described in Chapter 2, Section 2.6, we retrieve a local self-similar behavior of the velocity function, described by

$$c(\beta z) = \beta^{\alpha} c(z), \qquad \text{where } \sigma > 0. \tag{4.16}$$

The result of this inversion is an estimate of the singularity parameter α, for the scale σ in some bounded, positive region $[\sigma_{\min}, \sigma_{\max}]$.

From the contrast functions $\Delta c(z)/\bar{c}(z)$, a modified velocity contrast function $D(z)$ is defined according to

$$D(z) = \frac{1}{2\bar{c}(z)} \frac{\Delta c(z)}{\Delta z}. \tag{4.17}$$

Note that these velocity contrast functions can either be derived from velocity functions $c(z)$, where they are referred to as $D_c(z)$, or from seismic reflection data, referred to as $D_{\mathrm{R}}(z)$. In eq. (4.17) we recognize the approximation of a differentiation of the velocity function $c(z)$ with respect to z, so we can write

$$D(z) \approx \frac{1}{2\bar{c}(z)} \frac{dc(z)}{dz}. \tag{4.18}$$

Note that this is the well-known expression for the continuous reflectivity, for constant density. If we now substitute z by βz, we get

$$D(\beta z) \approx \frac{1}{2\beta\bar{c}(\beta z)} \frac{dc(\beta z)}{dz}. \tag{4.19}$$

We now assume that the background function $\bar{c}(z)$ is sufficiently smooth, such that

$$\bar{c}(\beta z) \approx \bar{c}(z). \tag{4.20}$$

This constraint is satisfied when the background velocity function $\bar{c}(z)$ contains no fluctuations within the scale range used in multiscale analysis of the velocity contrast function $D(z)$. The consequence of taking the real velocity function $c(z)$ instead of the smooth background function $\bar{c}(z)$ on the inversion for α is treated in Section 4.5.

Substituting eq. (4.20) and (4.16) into eq. (4.19) leads to

$$D(\beta z) \approx \frac{\beta^{\alpha-1}}{2\bar{c}(z)} \frac{dc(z)}{dz}. \tag{4.21}$$

Comparing the right-hand side of eq. (4.21) with that of eq. (4.18) gives the following self-similarity condition for velocity contrast functions

$$D(\beta z) \approx \beta^{\alpha-1} D(z). \tag{4.22}$$

Now we follow a similar derivation as in Chapter 2, Section 2.6. The wavelet transform $\check{D}(\sigma, z)$ (for real-valued wavelets $\vartheta(z)$) of $D(z)$ is defined as

$$\check{D}(\sigma, z) = \frac{1}{\sigma^{\mu}} \int_{-\infty}^{\infty} D(z') \vartheta\left(\frac{z'-z}{\sigma}\right) dz'. \tag{4.23}$$

Replacing z' by $\sigma z'$, z by σz and using eq. (4.22), where β is replaced by σ, for $\sigma > 0$, we arrive at

$$\check{D}(\sigma, \sigma z) = \sigma^{\alpha-\mu} \int_{-\infty}^{\infty} D(z')\, \vartheta(z'-z) dz', \tag{4.24}$$

or, comparing the right-hand side with that of eq. (4.23) for $\sigma = 1$, it follows that for the AVS-curves connected to local maxima of the wavelet transform of these velocity contrast functions $D(z)$

$$\check{D}(\sigma, \sigma z_{\max}) = \sigma^{\alpha-\mu}\, \check{D}(1, z_{\max}). \tag{4.25}$$

Taking the logarithm of the modulus of both sides of eq. (2.60) gives

$$\log_2 |\check{D}(\sigma, \sigma z_{\max})| = (\alpha - \mu) \log_2 \sigma + C_D, \tag{4.26}$$

with

$$C_D = \log_2 |\check{D}(1, z_{\max})|.$$

Note that if we would take $\mu = 1$, as in the derivation in Chapter 2, Section 2.6, the slope of the AVS-curve would give $(\alpha - 1)$. Therefore we take in the multiscale analysis of velocity contrast functions $\mu = 0$, such that eq. (4.26) becomes

$$\log_2|\check{D}(\sigma, \sigma z_{\max})| = \alpha \log_2 \sigma + C_D. \tag{4.27}$$

Now the slope of the AVS-curve, connected to a singular point in the velocity contrast function, gives the same estimate for the singularity parameter α as in the multiscale analysis of well-logs.

4.5 Influence of the background velocity on the inversion for α

The self-similar condition in eq. (4.22) is only valid when the background velocity profile $\bar{c}(z)$ does not contain fluctuations within the scale range used in multiscale analysis. Note that this was also recognized by Dessing (1997). This effect can be made clear by taking $\bar{c}(z) = c(z)$, the velocity function that contains all self-similar behavior. In that case $\frac{d}{dz}c(z)$ and $\bar{c}(z)$ satisfy the following scaling relations

$$\begin{aligned} \frac{dc(\beta z)}{dz} &= \beta^{\alpha-1}\frac{dc(z)}{dz}, \\ \bar{c}(\beta z) &= \beta^{\alpha}\bar{c}(z). \end{aligned} \tag{4.28}$$

If we recall the approximation of the modified velocity contrast function $D(z)$ in eq. (4.18)

$$D(z) \approx \frac{1}{2\bar{c}(z)}\frac{dc(z)}{dz}, \tag{4.29}$$

we see that when eqs. (4.28) hold we obtain, instead of the self-similar relation (4.22)

$$D(\beta z) = \beta^{-1} D(z), \tag{4.30}$$

which does not contain a reference to α anymore. Under this condition each α-estimate for a singular point in $D(z)$ will be 0 (cf. eqs. (4.22) to (4.27)). This result shows that in the inversion for the singularity parameter α, care should be taken in choosing the background velocity function $\bar{c}(z)$.

4.6 Application of the two-step inversion scheme to a synthetic data set

To test the two-step inversion scheme for the retrieval of the singularity parameter α from velocity contrast functions, a synthetic experiment is performed. Figure 4.2 shows real well-logs of the P- and S-wave velocities c_P

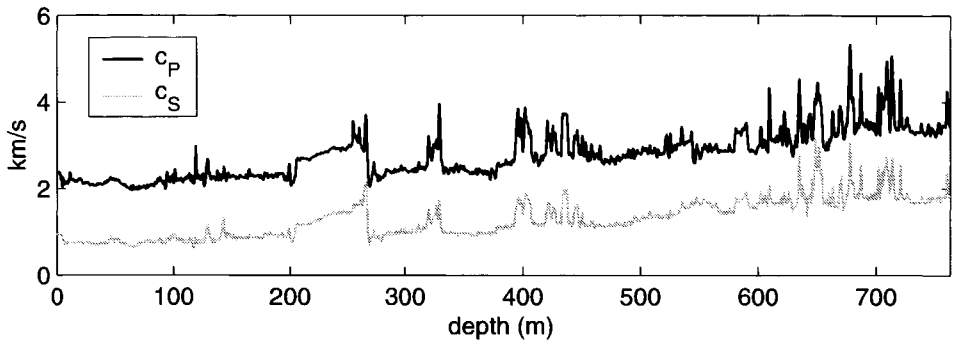

Figure 4.2: *Real well-logs of the P- and S-wave velocities c_P and c_S (provided by Mobil).*

and c_S with a depth sampling of .5 ft (0.1524 m). The density function is given by a constant value of 2000 kg/m^3. In these functions, synthetic data were modeled, using an elastic reflectivity method [Kennett (1983)]. In this experiment, only the P-P and the SV-SV reflectivities are analyzed. For brevity, the SV-SV data are referred to as S-S data.

Following, the P-P data were imaged up to an angle of 50° to acquire the angle-dependent image $\mathrm{R}_{PP}(p, z)$. As a background velocity in this imaging, a heavily smoothed, down-sampled version of the P-wave velocity in Fig. 4.2 was used. The depth sampling of this background velocity function was 1 m. The angle dependent image $\mathrm{R}_{PP}(p, z)$ is shown in Fig. 4.3b. We can see strong reflections in the range of 200 to 400m depth, which clearly correlate with outliers in the P-wave velocity function in Fig. 4.3a, at the same depths.

Similarly, the rayparameter-dependent image $\mathrm{R}_{SS}(p, z)$ is constructed for angles up to 50°. The result of this imaging is shown in Fig. 4.4b. We note that the spatial resolution of the image is much higher than the spatial resolution of the image of the P-P reflectivity in Fig. 4.3b. This is due to the fact that the S-wave velocity is much lower than the P-wave velocity (as can be

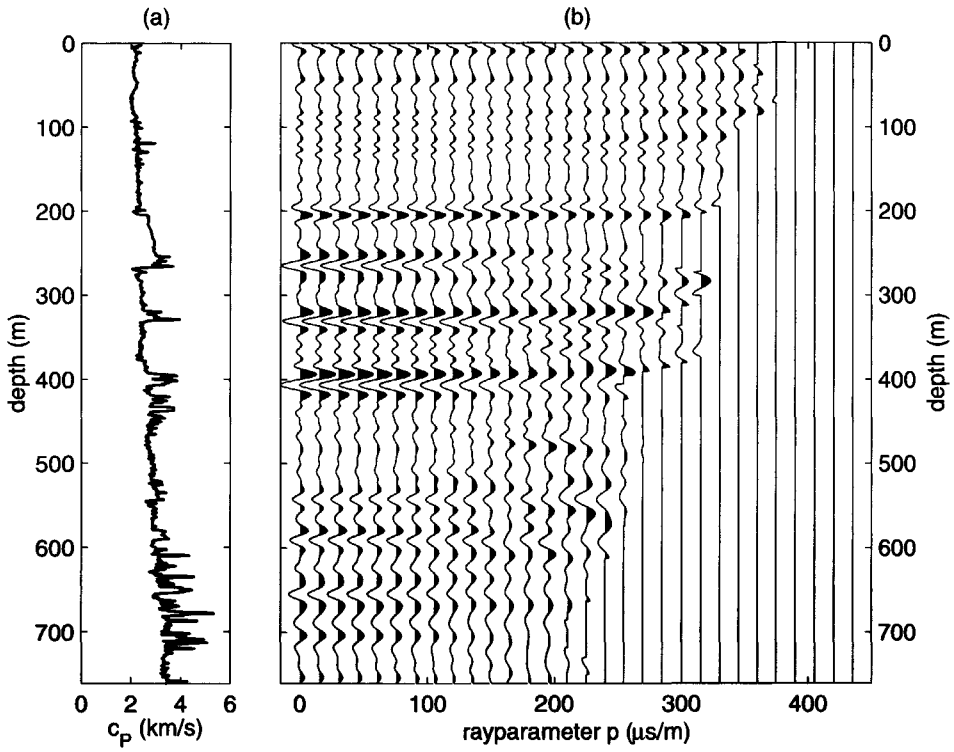

Figure 4.3: *(a) Real well-log of the P-wave velocity*
(b) Imaged rayparameter-dependent P-P reflectivity $R_{PP}(p, z)$*, as used for the Linearized Zoeppritz Inversion, imaged up to an angle of 50 degrees.*

visually checked in Fig. 4.2) and, consequently, the wavelength of S-waves is much smaller.

Again, we see that there is a good correlation between reflections in the image $R_{SS}(p, z)$ and outliers in the velocity function $c_S(z)$. A careful inspection of the image $R_{SS}(p, z)$ in Fig. 4.4b shows however an unexpectedly strong reflection at about 120 m depth, that does not correlate with a boundary in the S-wave velocity field. Comparing the velocity functions in Fig. 4.2 we see that there is a strong spike in the P-wave velocity at this depth, therefore this reflection can be contributed to higher order terms in the explicit Zoeppritz equation for the S-S reflectivity. Note that these higher order terms are not accounted for in the linearized expression for the S-S reflectivity in eq. (4.13).

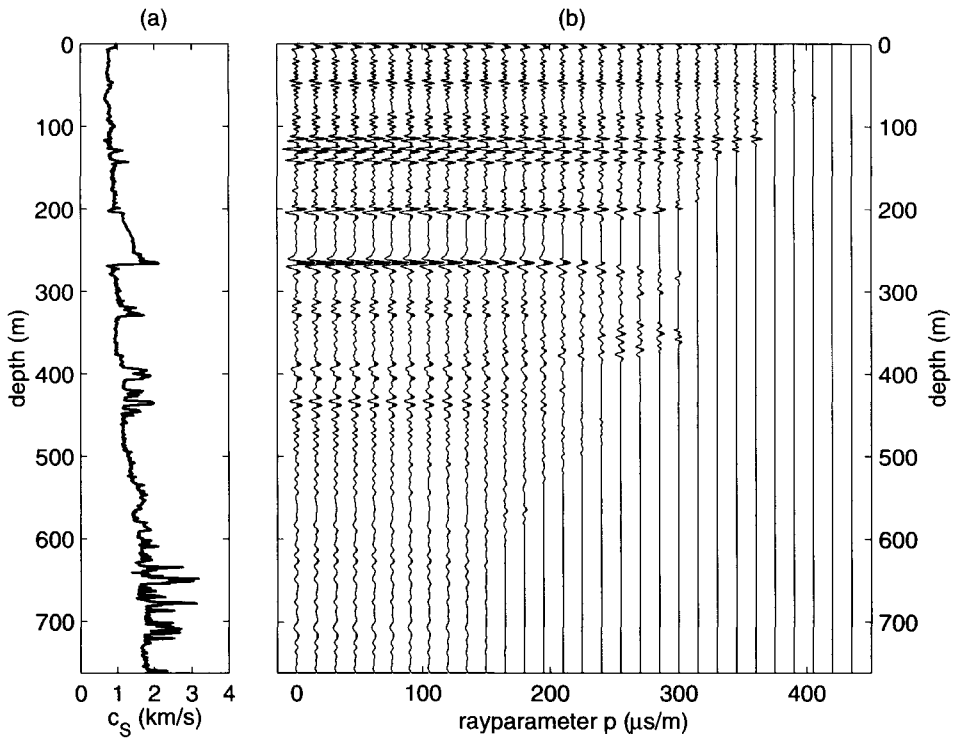

Figure 4.4: *(a) Real well-log of the S-wave velocity*
(b) Imaged rayparameter-dependent S-S reflectivity $\mathsf{R}_{SS}(p,z)$*, as used for the Linearized Zoeppritz Inversion, imaged up to an angle of 50 degrees.*

To the data sets $\mathsf{R}_{PP}(p,z)$ and $\mathsf{R}_{SS}(p,z)$ in Figs. 4.3b and 4.4b, the LZI algorithm is applied. The background P- and S-wave velocity fields were chosen identical to the migration velocities. The maximum angle of incidence taken into the inversion was 30°.

Figure 4.5 shows the inversion result $D_{\mathsf{R}_{PP}}(z)$, depicted by the black line. The quality of the inversion result can be assessed by comparing the inversion result $D_{\mathsf{R}_{PP}}(z)$ with the function $D_{c_P}(z)$, constructed from the actual P-wave velocity function (denoted by a grey line). To be able to compare both velocity contrast functions, the $D_{c_P}(z)$ is low-pass filtered and down-sampled to a 1 m spacing, such that it contains the same spatial bandwidth as the $D_{\mathsf{R}_{PP}}(z)$.

It is clear that the velocity contrast function $D_{\mathsf{R}_{PP}}(z)$, derived from the

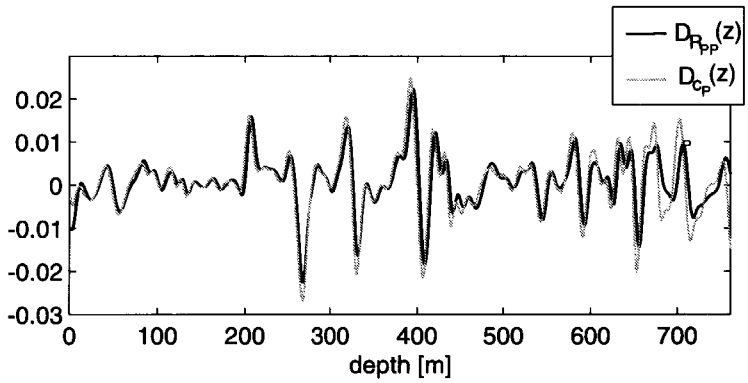

Figure 4.5: *Inversion result $D_{\mathsf{R}_{PP}}(z)$, derived from the image in Fig. 4.3b (black) and $D_{c_P}(z)$ derived from the well-log in Fig. 4.3a (grey).*

imaged P-P reflectivity, is well recovered, as it is almost identical to the velocity contrast function $D_{c_P}(z)$, derived directly from the well-log. However, starting from a depth of 600m, we note a mismatch between the two velocity contrast functions. Referring to Fig. 4.3a, we see that the reflections in the image $\mathsf{R}_{PP}(p, z)$ are relatively strong, which would normally enhance the quality of the inversion. However, we suspect that the image is contaminated with internal multiples, generated by the dense distribution of outliers in the velocity function around that depth range (Fig. 4.3a). Nevertheless, the general trend of the actual velocity contrast function $D_{c_P}(z)$ is well recovered by the $D_{\mathsf{R}_{PP}}(z)$.

We now assess the quality of the inversion on the S-S reflectivity. The inversion result $D_{\mathsf{R}_{SS}}(z)$ is shown in Fig. 4.6, denoted by the black line; the low-pass filtered and down-sampled $D_{c_S}(z)$ is represented by the grey line. We note that a larger discrepancy between both velocity contrast functions than in the analysis of the P-P reflectivity. Especially in the ranges of 100-200 m depth and below 600 m depth, we see large mismatches between the $D_{\mathsf{R}_{SS}}(z)$ and the $D_{c_S}(z)$. The mismatches at shallow depths can be explained from the fact that higher order terms in the explicit Zoeppritz equation are not taken into account by the inversion. For the mismatches below 600 m depth, we suppose that this is caused by internal multiples, similar to the effect we have seen in the inversion of P-P reflectivity. Still, the general trend of the velocity contrast function $D_{\mathsf{R}_{SS}}(z)$ matches the trend of the actual velocity contrast function $D_{c_S(z)}$ well.

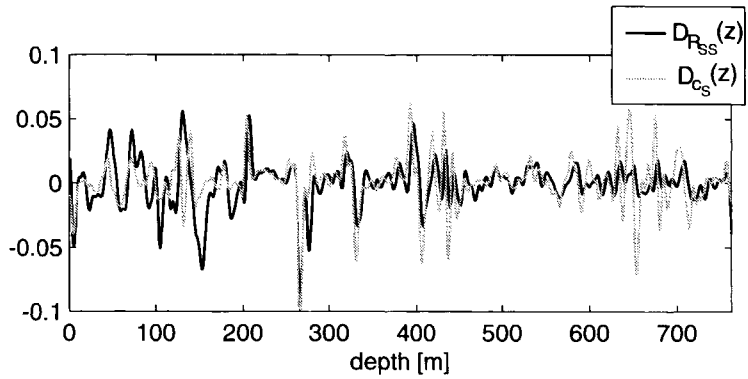

Figure 4.6: *Inversion result $D_{R_{SS}}(z)$, derived from the image in Fig. 4.4b (black) and $D_{c_S}(z)$ derived from the well-log in Fig. 4.4a (grey).*

The proposed multiscale analysis to derive the singularity parameter α is now applied to the velocity contrast functions for both the P-wave velocity and the P-P reflectivity (Fig. 4.5). Its results are shown in Fig. 4.7. Similar to the conventions in Fig. 4.5, the black circles represents the α-estimates derived from $D_{R_{PP}}(z)$ (denoted $\alpha_{R_{PP}}$) and the grey circles are the α-estimates derived from $D_{c_P}(z)$ (denoted by α_{c_P}). The lines interconnecting the circles are drawn for clarity only. The consistency of the estimate of the $\alpha_{R_{PP}}$-profile with the estimate of α_{c_P}-profile is rather convincing. Beyond 600 m depth however, the estimate is slightly in error, which we could expect from the mis-

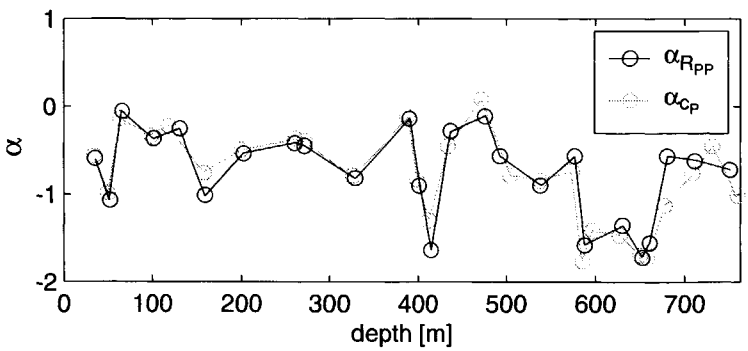

Figure 4.7: *Estimated α-profile derived from $D_{R_{PP}}(z)$ (black) and α-profile derived from $D_{c_P}(z)$ (grey)*

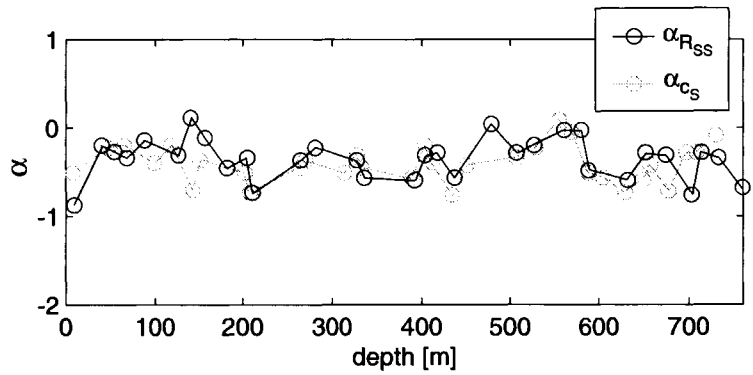

Figure 4.8: *Estimated α-profile derived from $D_{R_{SS}}(z)$ (black) and α-profile derived from $D_{c_S}(z)$ (grey)*

match in that depth range between the velocity contrast functions (Fig. 4.5). As noted before, this is probably caused by internal multiples.

In Chapter 5, a method is proposed to reduce the amount of internal multiples in walk-away VSP data. It will be shown that the reduction of internal multiples from field data greatly improves the consistency of the estimates of the $\alpha_{R_{PP}}$ with the estimates of the α_{c_P}.

The results of applying the multiscale analysis to the velocity contrast functions $D_{R_{SS}}(z)$ and $D_{c_S(z)}$ is shown in Fig. 4.8. The α-estimates derived from $D_{R_{SS}}(z)$ (denoted $\alpha_{R_{SS}}$) are depicted by the black circles and the α-estimates derived from $D_{c_S}(z)$ (denoted by α_{c_S}) by the grey circles. As we could expect from the lower quality of the velocity contrast function, derived from the S-S reflectivity, we note larger mismatches between both α-profiles. The general trend is however recovered quite nicely. The largest mismatch is found between 100-200 m depth. We attribute this to the fact that the linearized expression for the S-S reflectivity insufficiently accounts for the higher order terms in the explicit Zoeppritz equation.

4.7 Conclusions

A method for multiangle, multiscale analysis of both acoustic and elastic seismic reflection data has been proposed. The method consists of two steps.

The first step is the application of Linearized Zoeppritz Inversion (LZI) to

imaged rayparameter-dependent reflectivity gathers, to acquire velocity contrast functions, which are estimates of the velocity contrasts at each imaging depth. A test on synthetic data has shown that the velocity contrast functions derived from the rayparameter-dependent reflectivity gathers are generally good estimates of the actual velocity contrast functions.

The second step is a multiscale analysis of these velocity contrast functions. A technique, similar to the technique used to estimate the singularity parameter α from well-logs, is used to estimate the parameter α from velocity contrast functions. This method is applied to both the velocity contrast functions constructed by LZI and the velocity contrast functions derived directly from the velocity fields. It is shown that the estimates of singularity parameters α derived from both velocity contrast functions give consistent results. Higher order terms in the explicit Zoeppritz equations that are not accounted for in LZI and internal multiples are the main causes of errors in this inversion.

In the following two chapters this technique is applied to field data sets.

Chapter 5

Multiangle processing and multiscale characterization of walk-away VSP data

The research described in this chapter is a joint effort of dr. Menno Dillen and the author of this thesis. In this chapter the method for multiangle, multiscale analysis of elastic seismic data is applied to walk-away VSP data. Both synthetic and real data are treated. It is shown that a migration algorithm, specifically developed for walk-away VSP data, effectively suppresses multiple arrivals and improves the overall image quality. Furthermore, the multiscale analysis of well-log and seismic data is performed. It is shown that the results of the multiscale analysis of the well-log correlate better with the results of the multiscale analysis of the updated imaging scheme than with the results of the conventional imaging scheme.

5.1 Introduction

In this thesis, multiscale analysis is presented as a method for characterizing seismic reflection data and well-logs. The method has been tested on both synthetic (Chapters 3 and 4) and real (Chapter 6) surface data and well-logs. In this chapter, an approach is proposed for processing walk-away VSP data. Figure 5.1 shows the basic setup of a walk-away VSP configuration. The major difference with surface seismics is that the receivers are not at the surface, but are lowered in a bore-hole. Note the difference with normal VSP data, in which only one source at the surface is used. Normal VSP data are often used to construct a (1-D) velocity model of the subsurface, to calibrate surface data.

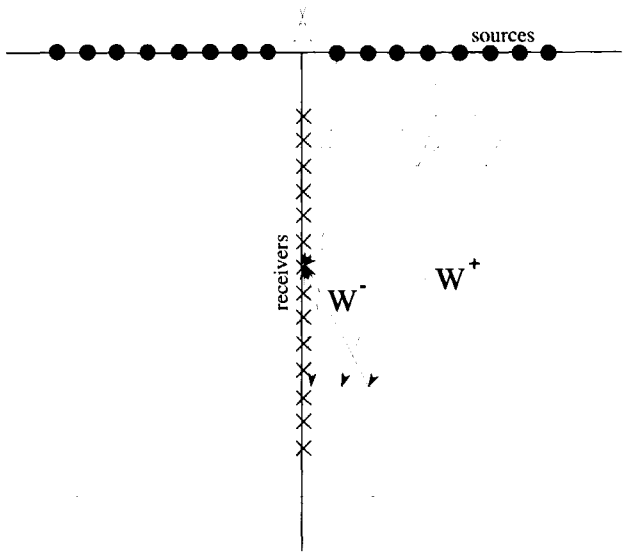

Figure 5.1: *Walk-away VSP-configuration.*

The reason for working with walk-away VSP data instead of surface data in this research, is that the receivers in a VSP experiment are close to the interfaces that we are analyzing. From fig. 5.1 we can see that the upgoing transmission path (from reflector to receiver), denoted by W^-, is shorter than the downgoing transmission path (from source to reflector), denoted by W^+. From the above observations, we understand that the propagation disturbances in walk-away VSP data are less than in surface data. Moreover, in the multiscale analysis, the correlation of the results with well-logs is easier, since no time-to-depth conversion is required. Therefore, VSP data are an excellent data type to apply the multiscale analysis to, if we want to test the method on real elastic data in a controlled way.

In walk-away VSP data we normally measure the inline, crossline and vertical particle velocities denoted by v_x, v_y and v_z respectively. To these data a complete processing sequence is applied, to arrive at rayparameter-dependent imaged reflectivity sections, which are the input of the multiscale analysis.

The method consists of the following steps:

1. Decomposition of the particle velocity components into P- and S-wave potentials. For this purpose an explicit polarization scheme is presented which uses the curl and the divergence of the inline and vertical particle velocity fields.

2. Separation of the P- and S-wave potentials into up- and downgoing wave field potentials. To this end the walk-away VSP's (which are common-receiver gathers) are reorganized into normal VSP's (which are common-source gathers). In this domain the separation is performed by applying a median filtering technique in the common-source domain.

3. Radon transform and rayparameter-dependent imaging of the rayparameter-dependent P-P and P-S reflection data. An improved imaging scheme is presented that uses the images from all receivers to construct more reliable imaged sections of these wave field potentials.

The multiscale analysis is then performed on the results of the imaging scheme above, making use of the technique described in Chapter 4.

4. Construction of velocity contrast functions from the imaged P-P data, making use of the Linearized Zoeppritz Inversion (LZI) by Van Wijngaarden and Berkhout (1995).

5. Multiscale correlation of the velocity contrast functions with the well-log. The results of the updated imaging scheme are compared with the results of the conventional imaging scheme.

First, synthetic walk-away VSP data are created, to assess the proposed processing sequence. Results of the application of the above processing scheme to these data are analyzed to detect possible weaknesses in the processing.

Using the experience from this analysis, the processing is then applied to a real walk-away VSP data set, which was recorded in a well near Boulogne-sur-Mer in France. In the remainder of this chapter, this data set is referred to as the *Boulogne VSP data set*. In the Boulogne VSP experiment, a P-wave velocity log was also recorded, which makes it possible to perform a multiscale correlation of the seismic reflection data with the well-log.

5.2 Multiangle processing and multiscale characterization of synthetic walk-away VSP data

In this section, the proposed processing and imaging scheme is further explained and illustrated with two examples on synthetic data. The results of these synthetic experiments are analyzed and conclusions from this analysis are given.

5.2.1 Decomposition of walk-away VSP data into P- and S-wave potentials

The decomposition of the particle velocity field $\boldsymbol{v}$ into P- and S-wave potentials is performed on two synthetic data sets. The source in these experiments is a pure P-wave source; no S-waves are excited by the source. Further, we choose a model that is invariant in the horizontal x- and y-directions, so no out-of-plane converted wave motion is generated. Therefore, we only consider the inline v_x and the vertical v_z particle velocities. The first synthetic 2-D data set is generated using an elastic reflectivity method [Kennett (1983)], where the densities and velocities are given by the plane-layered model shown in Table 5.1.

interface depth [m]	c_P [m/s]	c_S [m/s]	ρ [kg/m^3]
	1800	1200	1500
300			
	2100	1400	1700
400			
	2200	1500	1800
550			
	2500	1700	2000
700			
	3000	2100	2400

Table 5.1: *Parameters of the plane-layered model, as used for modeling the data in the first synthetic experiment.*

The model contains four interfaces at 300, 400, 550, and 700 m depth, respectively. The wave fields are computed at depths ranging from 300 to

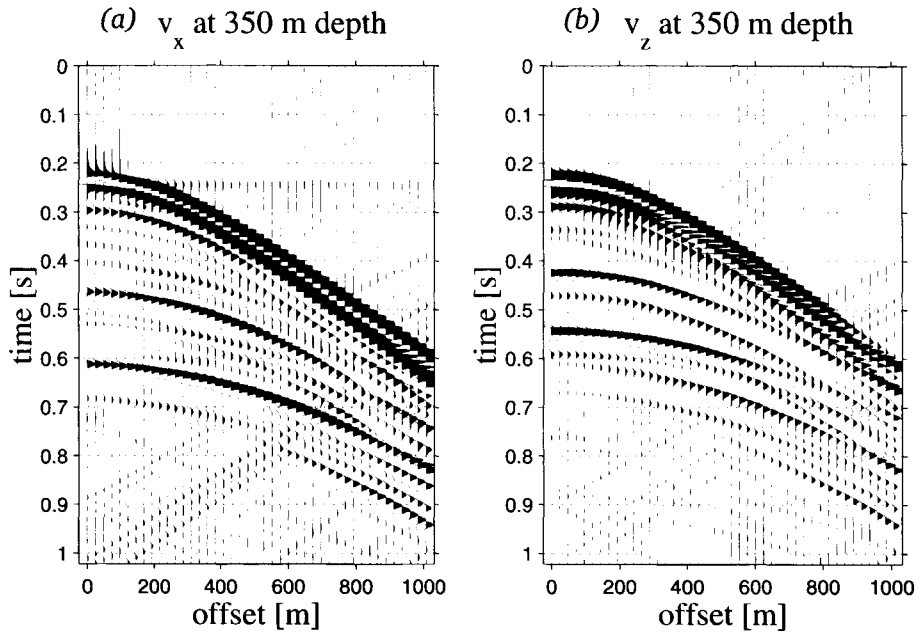

Figure 5.2: *(a) v_x and (b) v_z common-receiver gathers at a depth of 350 m.*

700 m with 10m interval, i.e., at 41 depth levels. The computed wave fields, with one source at the surface at zero offset from the bore-hole, and 512 receivers at various offsets from the bore-hole, at 41 depths, are converted to the walk-away VSP-configuration of Fig. 5.1, in which we have 41 receivers in the bore-hole and 512 sources at the surface. Interchanging sources and receivers and applying a reversal of the x-axis, utilizing the lateral-invariance of the layered medium, we obtain a common-receiver gather for every VSP depth. In Fig. 5.2 the v_x (a) and v_z (b) common-receiver gathers are shown for a depth of 350 m, i.e. between the first and second interface (see Table 5.1). We observe in both figures a primary downgoing wave and three reflections from the second, third, and fourth interface, respectively. The reflection from the second interface almost coincides with the primary downgoing wave.

In Fig. 5.3 the v_x (a) and v_z (b) common-source gathers are shown for a source-bore-hole offset of 320 m. Clearly, the down- and up-going wave field components are recognized, but also, from the slopes of the events,

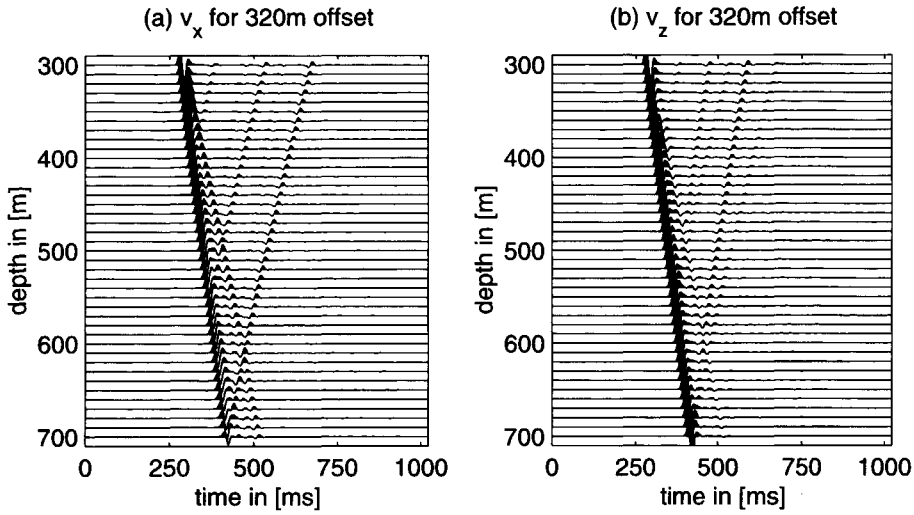

Figure 5.3: *(a) v_x and (b) v_z common-source gathers for a source-bore-hole offset of 320 m.*

the P- and S-wave field components can be distinguished. We observe in Fig. 5.3 that the v_x-wave field contains better discernible S-wave reflections than P-wave reflections, whereas in the v_z-wave field the P-wave reflections are more pronounced.

In order to decompose the v_x- and v_z-wave fields into P- and S-wave field potentials, we use the following definition [Wapenaar and Berkhout (1989)]:

$$-\rho\frac{\partial \boldsymbol{v}\,(x,z,t)}{\partial t} = \nabla\phi\,(x,z,t) + \nabla\times\boldsymbol{\psi}\,(x,z,t)\,, \tag{5.1}$$

where $\phi\,(x,z,t)$ is the scalar P-wave potential and $\boldsymbol{\psi}\,(x,z,t)$ is the vectorial S-wave potential. If we take the divergence of both sides of eq. (5.1) we arrive at

$$\begin{aligned}\rho\frac{\partial\nabla\cdot\boldsymbol{v}\,(x,z,t)}{\partial t} &= -\nabla^2\phi\,(x,z,t)\\ &= -\frac{1}{c_P^2}\frac{\partial^2\phi\,(x,z,t)}{\partial t^2},\end{aligned} \tag{5.2}$$

where the 2-D wave equation for the P-wave potential is used. When we

integrate both sides of eq. (5.2) with respect to time, we obtain

$$\begin{aligned} \frac{\partial}{\partial t}\phi(x,z,t) &= -\rho c_P^2 \nabla\cdot\boldsymbol{v}(x,z,t) \\ &= -(\lambda+2\mu)\nabla\cdot\boldsymbol{v}(x,z,t), \end{aligned} \tag{5.3}$$

where λ and μ are the local Lamé parameters, which are related to c_P, c_S and ρ according to

$$\begin{aligned} c_P &= \sqrt{\frac{\lambda+2\mu}{\rho}} \\ c_S &= \sqrt{\frac{\mu}{\rho}}. \end{aligned} \tag{5.4}$$

Similar to eq. (5.2) we can take the curl of both sides of eq. (5.1) to arrive at

$$\begin{aligned} \rho\frac{\partial\nabla\times\boldsymbol{v}(x,z,t)}{\partial t} &= -\nabla\times\nabla\times\boldsymbol{\psi}(x,z,t) \\ &= \frac{1}{c_S^2}\frac{\partial^2\boldsymbol{\psi}(x,z,t)}{\partial t^2}, \end{aligned} \tag{5.5}$$

where the wave equation for the S-wave potential is used. Integrating both sides of eq. (5.5) with respect to time, and taking only the y-component, gives the following expression for the scalar S-wave potential ψ_y, which is the y-component of the vectorial S-wave potential $\boldsymbol{\psi}$,

$$\begin{aligned} \frac{\partial}{\partial t}\psi_y(x,z,t) &= \rho c_S^2\left(\nabla\times\boldsymbol{v}\right)_y(x,z,t) \\ &= \mu\left(\nabla\times\boldsymbol{v}\right)_y(x,z,t). \end{aligned} \tag{5.6}$$

For brevity, we will drop the index y, such that $\psi=\psi_y$. In eq. (5.3) the time-derivative of the scalar P-wave potential ϕ is obtained by taking the divergence of the velocity wave field vector $\boldsymbol{v}=(v_x,v_z)^{\mathrm{T}}$. The y-component of the curl of $\boldsymbol{v}$ in eq. (5.6) produces the time-derivative of the scalar S-wave potential ψ. Writing the ∇-operators in eqs. (5.3) and (5.6) in terms of spatial partial derivatives and integrating with respect to time, gives

$$\phi(x,z,t) = -(\lambda+2\mu)\int_{-\infty}^{t}\left[\frac{\partial}{\partial x}v_x(x,z,t') + \frac{\partial}{\partial z}v_z(x,z,t')\right]\mathrm{d}t', \tag{5.7}$$

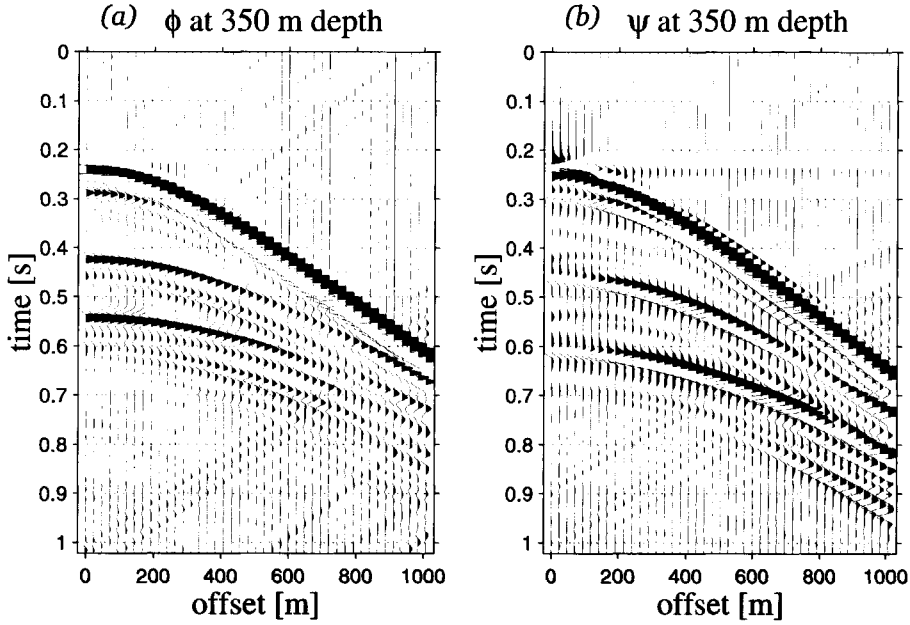

Figure 5.4: *(a) ϕ and (b) ψ common-receiver gathers at a depth of 350 m.*

and

$$\psi(x,z,t) = \mu \int_{-\infty}^{t} \left[\frac{\partial}{\partial z} v_x(x,z,t') - \frac{\partial}{\partial x} v_z(x,z,t') \right] \mathrm{d}t'. \qquad (5.8)$$

These last two equations are solved numerically to obtain the P- and S-wave field potentials from the v_x- and v_z-wave field components. The partial derivatives with respect to the x- and z-coordinates are solved using second-order central finite-differences. The partial derivative with respect to the x-coordinate is computed using common-receiver data, as shown in Fig. 5.2. In this domain the sources cover the x-axis along the surface which makes it possible to compute these finite differences. The central finite-difference operator uses three offsets to calculate a partial derivative with respect to the x-coordinate, assuming lateral-invariance of the medium. The partial derivative with respect to the z-coordinate is obtained from the common-source data, as shown in Fig. 5.3, using three depths. At the data boundaries end-on left or right finite-differences are employed. Subsequently, the integrations with respect to time, in eqs. (5.7) and (5.8) are applied numerically to the

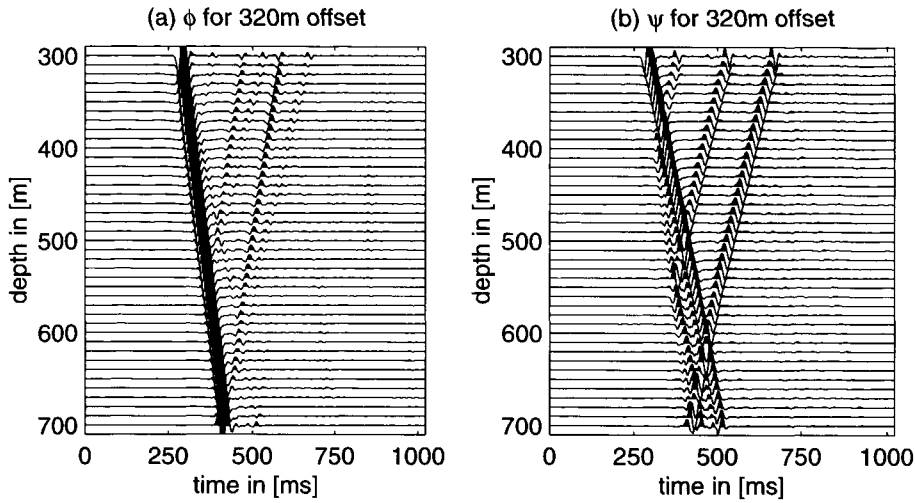

Figure 5.5: *(a) ϕ and (b) ψ common-source gathers for a source-bore-hole offset of 320 m.*

computed partial derivatives. On noisy field data the integrations produce a large time-variant DC-component. The DC-component is removed from the time-integrated result by smoothing the integrated data by convolving the data with a low frequent gaussian function and subsequently subtracting the smoothed data from the time-integrated data.

In Fig. 5.4 the common-receiver P- and S- wave potential gathers are shown for a receiver depth of 350 m. The down- and up-going P- and S-wave events are best recognized in the common source gathers in Fig. 5.5 from the slopes associated with the respective wave velocities. We observe in Fig. 5.5 residual S-wave amplitudes in the ϕ-gather, and residual P-wave amplitudes in the ψ-gather, due to the finite difference approximation of the spatial partial derivatives.

5.2.2 Separation of P- and S-wave potentials into up- and downgoing wave field components

The P- and S-wave potentials of the previous section are now separated into up- and downgoing wave field components by means of subtraction of down- and upgoing wave fields respectively. The simplest way to remove

the up- or downgoing wave modes is by applying an (f, k)-based filter to the data. To this end, the walk-away VSP data are reorganized into common-source gathers, in which representation the downgoing wave fields are visible as events with a negative slope and upgoing wave fields as events with a positive slope. If the data are then transformed into the (f, k)-domain, the half-plane described by $k > 0$ represents the downgoing wave field, which can be removed by applying a pie-shape filter to this part of the data. However, it is known from literature [e.g. Sheriff (1984)], that applying such a filter to seismic data induces the –sometimes very strong– unwanted effect of Rieber mixing. This Rieber mixing is characterized by a spatial averaging of the upgoing data along the position of each removed downgoing event and vice versa. Therefore, this technique is not particularly apt to the separation of up- and downgoing wave fields.

A better method for this separation is described by Hardage (1983), in which the respective down- and upgoing wave fields can be estimated in the *linear move-out* or LMO-domain, by means of median filtering. This technique has the advantage that, because of the fact that it is performed in the (z, t)-domain, it does not have the problem of spatial averaging. The first processing step (for acquiring the upgoing wave field) is to accurately pick the downgoing wave modes and perform a negative time-shift to each reflection, such that all downgoing wave modes align vertically. After this alignment we refer to these data as LMO-corrected VSP data. Note that performing the LMO accurately is the most crucial step in the processing, as very small time shifts will introduce large amounts of noise to the *whole* data set! In the LMO-corrected VSP data, the upgoing events are attenuated by applying a vertical median filter to the data, where the median is typically taken over five samples. The effect of the median filter is that all strictly vertical events (the downgoing events) in the data set are preserved, whereas all non-vertical events (the upgoing events) are strongly attenuated. After the median filtering, the result is inversely LMO-corrected, and subtracted trace-by-trace from the original data set. In this way, the downgoing wave field components are attenuated, which gives an estimate of the upgoing wave field. The same technique is also applied vice versa, to arrive at an estimate of the downgoing wave fields. An important mathematical property of the median filter is that it is a non-linear process. The footprint of the median filter is therefore dependent on the position at which it was performed in the processing sequence. In our VSP processing sequence we chose to perform the median filtering after the decomposition into P- and S-wave potentials, because of

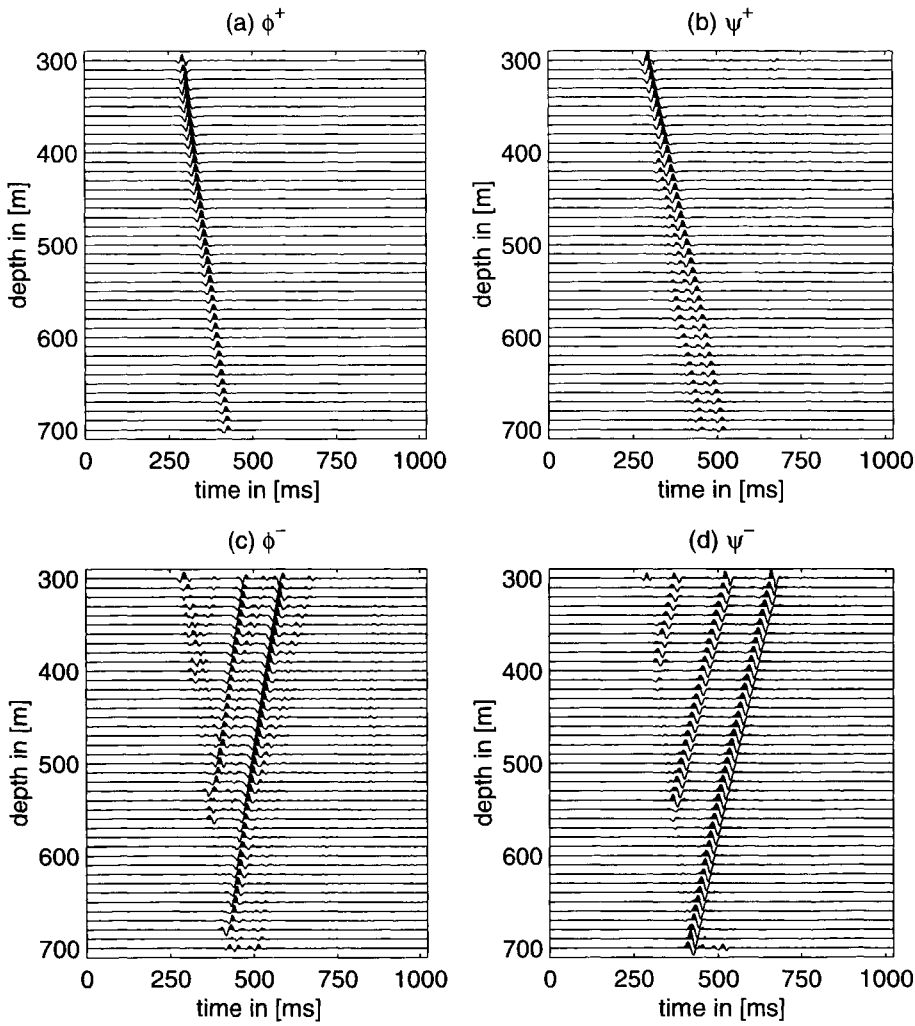

Figure 5.6: *Up- and downgoing P- and S-wave potentials for a for a source offset of 320m, constructed by median filtering. (a) The downgoing P-wave potential ϕ^+ .*
(b) The downgoing S-wave potential ψ^+
(c) The upgoing P-wave potential ϕ^-.
(d) The upgoing S-wave potential ψ^-.

the different linear move-outs of P- and S-waves. A second remark that has to be made is that due to small errors in the LMO correction, we introduce high-frequency noise (referred to as *whiskers*) to the estimates of the up- and downgoing wave fields. We therefore have to apply a band-pass filter to the data, such that the frequency content of the estimates is approximately equal to the frequency content of the full data set, thus effectively removing these whiskers.

Figure 5.6 shows the result of this filtering technique, in the common-source domain. In these figures an example has been given for the intermediate source offset of 320m. The downgoing P-wave potential ϕ^+ (fig. 5.6a) shows a strong attenuation of the other wave modes. No energy of the upgoing wave modes is visible, and there is no spatial averaging of the downgoing wave fields visible. In the downgoing S-wave potential ψ^+ (fig. 5.6b) we see that the upgoing wave field is also strongly attenuated. Because the source in this experiment is a strict P-source, all downgoing S-waves are converted waves generated at the boundaries in the model. In Figs. 5.6c,d we see the upgoing P- and S-wave potentials. It is clear from these figures that the down-going field is not fully attenuated. The reason for this effect lies in the relatively strong downgoing wave field compared to the upgoing wave field. In real walk-away VSP data we normally do not encounter such strong downgoing events as in the synthetic data. Therefore we will also use this technique for separation of up- and downgoing wave fields on real walk-away VSP data.

5.3 Imaging and characterization of rayparameter-dependent synthetic walk-away VSP data

5.3.1 Imaging of rayparameter-dependent synthetic walk-away VSP data

In this section it is explained how upgoing wave fields ϕ^- and ψ^- (which are in the (x,t)-domain) can be imaged to the rayparameter-dependent P-P and P-S reflectivity in the rayparameter-depth (p,z)-domain. Two imaging approaches are discussed, the conventional rayparameter-dependent imaging technique as described in Chapter 3, Section 3.3.2, and a novel adaption to this imaging technique, that combines the images at all receiver depths into one piecewise constructed image.

To compare the proposed novel imaging scheme with the conventional

scheme, a test is performed on a synthetic data set. Figure 5.7a shows a real c_P- and c_S-velocity function, a 182m long section of well-log ranging from 300 to 482m depth. The real well-log data is made available by Mobil. The density is taken constant at a value of 2000 kg/m^3. The seismic velocities from the surface to 300m depth are taken at a constant value of 1000m/s (c_S) and 2300m/s (c_P). In this velocity model, synthetic walk-away VSP data (particle velocities v_x and v_z) are modeled for 24 receiver depths, ranging from 300 to 482m, with a constant receiver spacing of 7.9m. The up- and downgoing wave fields are constructed by the method described in Section 5.2. After the separation into up- and downgoing wave fields, the upgoing wave fields are organized back into common-receiver gathers. The results of this processing (i.e. the upgoing wave field potentials ϕ^- and ψ^-) are shown in Fig. 5.7b,c.

Before imaging to the rayparameter-depth (p,z)-domain can be performed, the data are transformed into the Radon domain, by means of the Radon transform (cf. Chapter 3, Section 3.3.1). By applying this transform, we arrive at the data sets $\hat{\phi}^-(p,\tau)$ and $\hat{\psi}^-(p,\tau)$ respectively. These data sets, which are computed for every receiver depth, are the input of the described imaging schemes.

The first imaging approach is the construction of rayparameter-dependent depth images of the P-P and P-S reflectivity $\mathsf{R}_{PP}(p,z)$ and $\mathsf{R}_{SP}(p,z)$[1] for every single receiver depth. This imaging approach is similar to the imaging approach described in Chapter 3, Section 3.3.2, with the difference that the upgoing wave field operators W^- do not range to the surface (z=0), but to the respective receiver depths (z=z_{rec}). In this chapter we ignore the dispersion effects caused by the fine-layering; ongoing research by prof. Kees Wapenaar is focused on developing an approach for incorporating the attenuation estimates obtained from the downgoing wave fields ϕ^+ and ψ^+ to improve the propagators W^+ and W^- in this imaging approach.

Figures 5.8b and 5.9b show the results of this imaging approach for the topmost receiver at 300m depth for the P-P and P-S data respectively. These imaging results show clear horizontal reflections, however the imaged primary events are contaminated by internal multiples (the events which have a negative move-out) and the deeper P-P reflections seem to contain some

[1]We refer to P-wave data converted to S-wave data as P-S data. However, the image for this data type is called $\mathsf{R}_{SP}(p,z)$, to be consistent with prevalent operator notation.

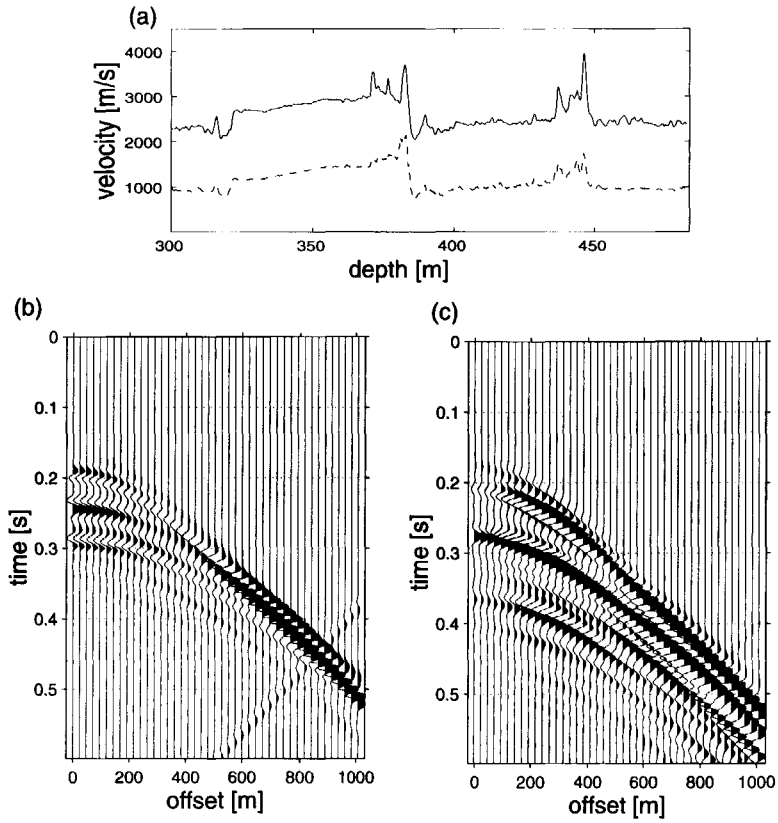

Figure 5.7: *(a) Velocity profiles c_P (solid) and c_S (dashed) of the finely-layered target. (b) upgoing P-wave potential ϕ^- at 300m depth.*
(c)upgoing S-wave potential ψ^- at 300m depth.

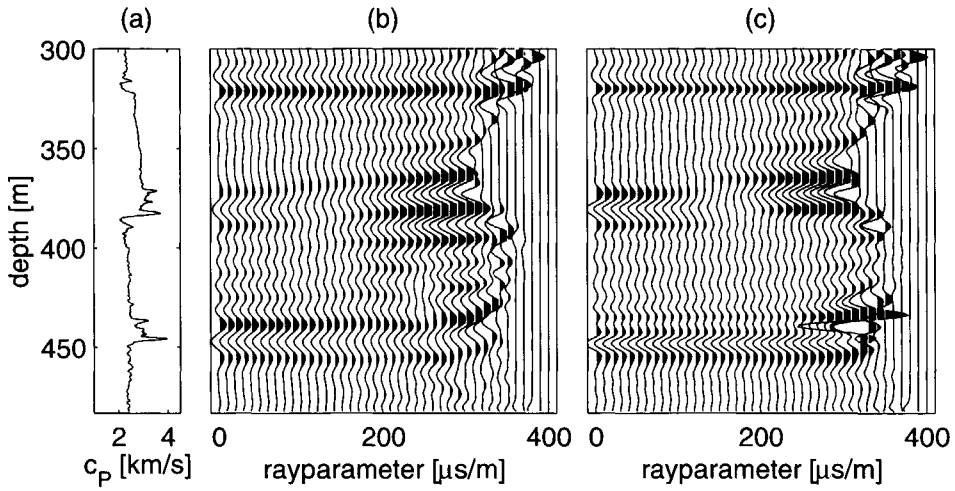

Figure 5.8: *(a) P-wave velocity profile.*
(b) Depth image $\mathsf{R}_{PP}(p,z)$ *for the receiver at 300m depth.*
(c) Piecewise depth image $\mathsf{R}^{\mathrm{pw}}_{PP}(p,z)$ *constructed by combining depth images of all receivers.*

amplitude and phase distortions. However, the match between the velocity profiles in Figs. 5.8a and 5.9a is good, as the depths of the main outliers in the velocity profiles coincide with the main reflectors.

The second imaging approach is focused on improving the images created by the first approach. In brief, it consists of constructing a piecewise depth image $\mathsf{R}^{\mathrm{pw}}(p,z)$ by concatenating subimages from the receiver which is nearest to a specific depth in the image.

With the first imaging approach, we have constructed rayparameter-dependent images $\mathsf{R}_n(p,z)$ for all receiver depths z_n separately. Let us assume there are N receiver depths in the experiment. The piecewise constructed image is built up as follows. First we select the reflectivity from the images $\mathsf{R}_n(p,z)$ for the interval $z \in d_n = [z_n + \Delta z, z_{n+1}]$, where Δz is the depth sampling in imaging. Hence, we define subimages $\mathsf{R}^{\mathrm{sub}}_n(p,z)$ as

$$\mathsf{R}^{\mathrm{sub}}_n(p,z) = \begin{cases} \mathsf{R}_n(p,z) & \text{for} \quad z \in d_n \\ 0 & \text{for} \quad z \notin d_n. \end{cases} \tag{5.9}$$

We now have N subimages, where every subimage represents the re-

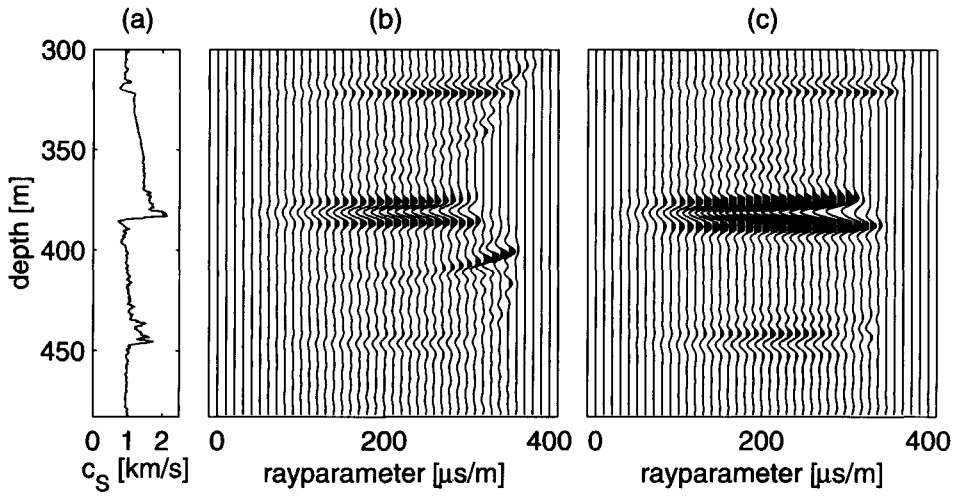

Figure 5.9: *(a) S-wave velocity profile.*
(b) Depth image $\mathsf{R}_{SP}(p,z)$ *for the receiver at 300m depth.*
(c) Piecewise depth image $\mathsf{R}^{\mathrm{pw}}_{SP}(p,z)$ *constructed by combining depth images of all receivers.*

flected arrivals, nearest in vertical sense to the receiver at z_n. The *piecewise constructed image* $\mathsf{R}^{\mathrm{pw}}(p,z)$ is defined as the sum of these subimages, according to

$$\mathsf{R}^{\mathrm{pw}}(p,z) = \sum_{n=1}^{N} \mathsf{R}^{\mathrm{sub}}_n(p,z). \tag{5.10}$$

By applying this technique, we reduce the number of internal multiples in the image, because the subimages mainly contain the primaries reflected from the nearest reflector below the receiver, or, when no reflector is present in that depth interval, no reflections at all. Furthermore, the amplitudes of the deeper events are better preserved in this piecewise constructed image than in the image of the topmost receivers, because the upgoing transmission paths are shorter.

The depths z_i of the receivers for which the images $\mathsf{R}^{\mathrm{pw}}_{PP}(p,z)$ and $\mathsf{R}^{\mathrm{pw}}_{SP}(p,z)$ have been created range from 300 to 482m, therefore the piecewise constructed images represent the same depth interval as the conventional images from the receiver at 300m depth. Figures 5.8c and 5.9c show the results

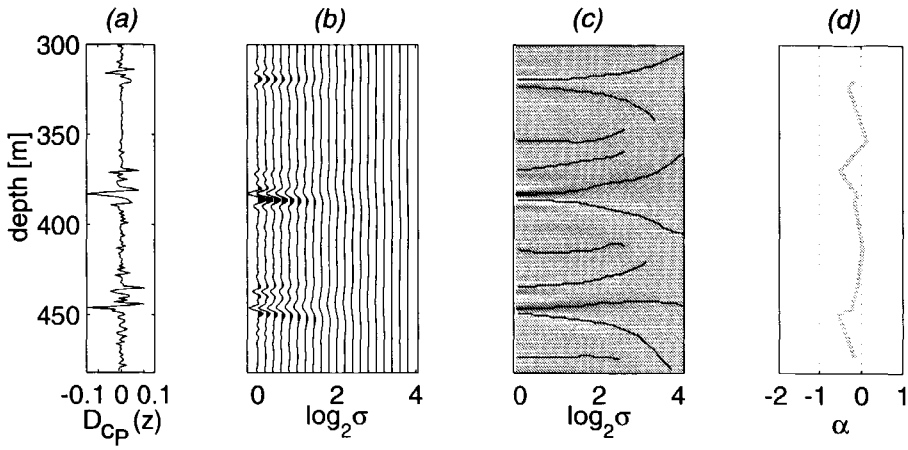

Figure 5.10: *(a) Velocity contrast function $D_{c_P}(z)$ from P-wave velocity profile in Fig. 5.7a*
(b) Continuous Wavelet Transform of (a)
(c) Position of modulus-maxima lines in wavelet transform
(d) Estimates of α as a function of depth

of the piecewise imaging approach. It is clear that this imaging technique has considerably decreased the amount of imaged internal multiples. Note that only at points where the velocity profiles change rapidly, we see reflection events in the piecewise constructed images R^{pw}_{PP} and R^{pw}_{SP}. Furthermore, there are neither amplitude nor phase distortions for the deeper events visible anymore. At first sight the piecewise imaging technique has drastically improved the quality of the images.

5.3.2 Multiscale characterization of the imaged rayparameter-dependent synthetic walk-away VSP data

The multiscale characterization on the imaged rayparameter-dependent P-P reflectivity in Fig. 5.8, is performed following the approach discussed in Chapter 4.

As a reference, we have constructed the velocity contrast function $D_{c_P}(z)$ directly from the P-wave velocity profile in Fig. 5.7a. The result is depicted in Fig. 5.10a; it shows strong outliers at the same depths as they are visible in the P-wave velocity profile. Next, we have computed the singularity

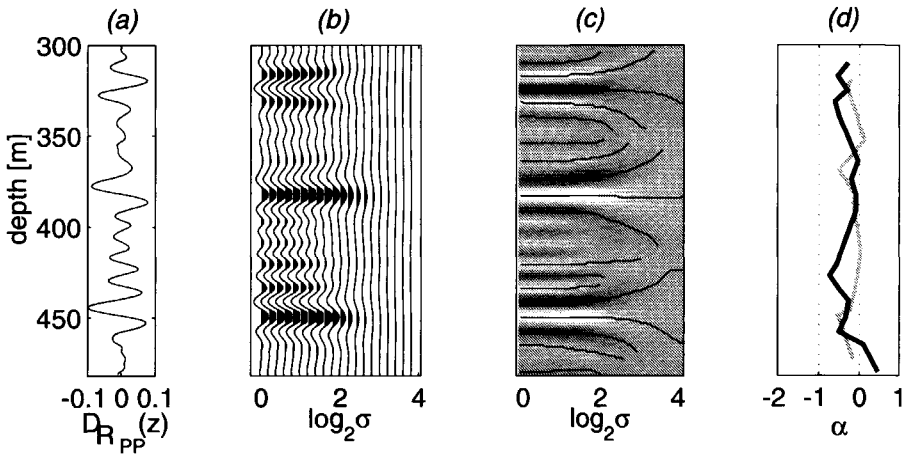

Figure 5.11: *(a) Estimate of $D_{\mathrm{R}_{PP}}(z)$ from the image $\mathrm{R}_{PP}(z{=}300\mathrm{m})$ in Fig. 5.8b*
(b) Continuous Wavelet Transform of (a)
(c) Position of modulus-maxima lines in wavelet transform
(d) Estimates of α as a function of depth from $D_{\mathrm{R}_{PP}}(z)$ (black) and from $D_{c_P}(z)$ (grey)

parameter profile (α-profile) of this velocity contrast function. The analysis and the result are visible in Fig. 5.10b-d.

For the comparison of estimates of α from well-log and seismic data, we now compute the velocity contrast functions $D_{\mathrm{R}_{PP}}(z)$ and $D_{\mathrm{R}^{\mathrm{pw}}_{PP}}(z)$ from the data in Fig. 5.8b,c, where the Linearized Zoeppritz inversion for raypa-rameter-dependent P-P reflectivity of Van Wijngaarden (1998) was used. Figure 5.11a shows the estimate of $D_{\mathrm{R}_{PP}}(z)$ from the conventional image $\mathrm{R}_{PP}(z{=}300\mathrm{m})$. Figure 5.12a shows the result acquired from the piecewise constructed image $\mathrm{R}^{\mathrm{pw}}_{PP}$. It is clear from these figures that the $D_{\mathrm{R}^{\mathrm{pw}}_{PP}}(z)$-profile in Fig. 5.12a is much more pronounced than the $D_{\mathrm{R}_{PP}}(z)$ in Fig. 5.11a; it mainly shows the strong reflectors in the finely-layered package, whereas $D_{\mathrm{R}_{PP}}(z)$ in Fig. 5.11a seems to be affected by the multiple arrivals.

Figures 5.11/5.12b-d show the results of performing the multiscale analysis on these data and extracting estimates of α for every modulus maxima line (the black lines in Figs. 5.11/5.12d.) The grey line is the result from Fig. 5.10d, to make it possible to accurately compare the different α-profiles.

The estimates of α from both data sets show a very good match with

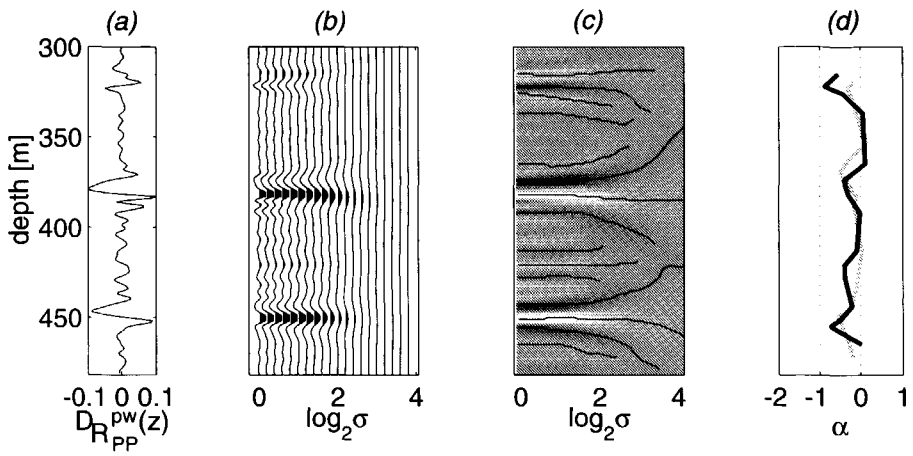

Figure 5.12: *(a) Estimate of $D_{R_{PP}^{pw}}(z)$ from the piecewise constructed image R_{PP}^{pw} in Fig. 5.8c*
(b) Continuous Wavelet Transform of (a)
(c) Position of modulus-maxima lines in wavelet transform
(d) Estimates of α as a function of depth from $D_{R_{PP}^{pw}}(z)$ (black) and from $D_{c_P}(z)$ (grey)

the estimates directly from the velocity contrast function, derived from the well-log. It seems that the estimation of α from velocity contrast functions derived from the images is not very sensitive to the multiple arrivals, however the estimates from velocity contrast function, derived from the piecewise constructed image (Fig. 5.12d) are more accurate than the results of the data constructed from the receiver at 300m depth (Fig. 5.11d). Especially at larger depth, the difference in quality is well visible.

The results of the above novel imaging scheme of rayparameter-dependent synthetic VSP data, have shown that the novel scheme is capable of effectively suppressing the imaged multiple arrivals. It has been shown that inversion for α from velocity contrast functions derived from imaged rayparameter-dependent reflectivity is improved by applying the piecewise imaging scheme. Therefore this technique will be tested on the Boulogne walk-away VSP data set and compared to the results of the conventional imaging and characterization scheme.

5.4 The field data set of Boulogne-sur-Mer

The processing sequence described in Sections 5.1-5.3 is applied to a real walk-away VSP data set, recorded in June 2000 near Boulogne-sur-Mer, France. This VSP experiment is part of a larger research project, led by dr. Guy Drijkoningen and funded by Netherlands Research Centre for Integrated Solid Earth Sciences (ISES). In this project, the objective is to correlate geological, petrophysical and seismic data. The VSP experiment is especially meant for correlating the latter two.

This walk-away VSP experiment was performed in a bore-hole on the tidal flat at the foot of a cliff about 6km north of Boulogne-sur-Mer, in the village Wimereux. Around the position of the bore-hole, it is expected, from geological measurements, that the subsurface is approximately horizontally layered, with an estimated maximum inline dip (with respect to the shotline orientation) of a few degrees. The crossline dip is negligible. The bore-hole is approximately 136m deep and it shows about the same lithology as the cliff about 1 km south of the bore-hole, because of a large monoclinal structure halfway between these two points. From the caliper run, it turned out that there were major wash-outs in the bore-hole at 48m and at 95m depth. At these depths, the geology consisted of unconsolidated clays, which were washed out during the flushing of the bore-hole. In this bore-hole, a string with eight 3-component geophones, with 2m separation, was lowered and a full walk-away VSP was recorded, for every depth, with source-bore-hole offsets ranging from 0 to 75m, with 1.5m spacing, thus making 51 offsets. The string was pulled up from 126m depth to 2m depth, which gives 63 depth locations of the geophones, taking the 2m spacing of the geophones into account.

The source in this experiment was the portable P-wave vibrator of the University of Utrecht, which was developed by drs. Vincent Nijhof, as part of a project funded by the Dutch Science Foundation STW. Every shotposition was covered 4-fold. The sweep of the P-wave vibrator ranged from 50-900Hz. The data were sampled at $250\mu s$; an anti-alias filter in the field was active from 1kHz. It is to be noted that the P-wave vibrator is not a strict P-source, like an airgun or dynamite. It is most accurately described as a 'vertical force' source, which means that it emits S-waves at oblique angles to the surface. From this we can understand that we have S-wave arrivals in the down-going field at all shotpositions, except for normal incidence.

Before the well was cased, the combined monopole/dipole tool of ISES was lowered in the borehole to measure the P-wave and S-wave veloci-

ties. At the time of writing however, no reliable measurements of the P- and S-wave velocities could be acquired. Instead, the P-wave velocities are measured from the recovered core, which was performed by drs. Hendrik Braaksma. Drs. Braaksma measured only the P-wave velocities for every 1cm, using the specialized equipment at the Free University of Amsterdam. Therefore, no S-wave velocity profile is available for the Boulogne VSP data set. In this research we use these core measurements to test the correlation with the walk-away VSP data.

The preprocessing of the walk-away VSP data consisted of two steps. The first step, which was deconvolution of the data by the measured base-plate and reaction mass motion, was performed by drs. Vincent Nijhof of OYO-CAG. We therefore do not have to apply deconvolution to this data set; it is already the band-limited reflection response of the earth.

The second step was the rotation of the two horizontal components, such that at every depth we have the true inline and crossline v_x and v_y components. When we lower a cable with 3-component geophones in the bore-hole, we do not know the rotation of the geophones around the vertical axis. Therefore, we have to use an indirect technique to measure this rotation. To this end, at every depth of the geophones, one recording with a true P-wave source at intermediate offset has to be made. The true P-wave source in the experiment was an airgun, which was hung in a large ($1m^3$) bowl of water, partially dug into the sand of the beach. The airgun was positioned about 70m from the bore-hole, normal to the shotline of the P-wave vibrator. The rotation of the geophones can then be estimated by rotating the first break measured at the two horizontal components in such a way that the v_x component has minimum amplitudes and the v_y has maximum amplitudes. When the same rotation is applied to measurements of the walk-away VSP data, we arrive at the true inline v_x and crossline v_y components of the wave fields. This processing has been performed by dr. Ranajit Ghose.

5.5 Wave field decomposition of the Boulogne VSP data set

The processing sequence of sections 5.2.1 and 5.2.2, which was demonstrated on synthetic VSP data, is applied to the Boulogne VSP data. Figure 5.13 shows the inline (v_x) and vertical (v_z) particle velocity wave field, received by the geophone at 40m depth, in the common-receiver domain. A topmute of 7ms has been applied to remove the noise introduced by the deconvolution process.

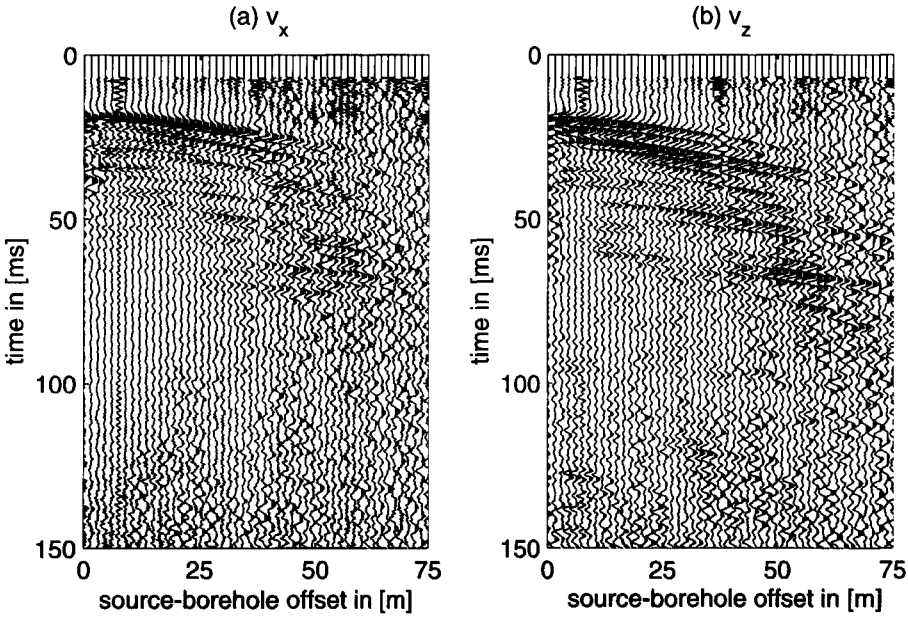

Figure 5.13: *(a) Inline particle motion v_x of the Boulogne VSP data for the receiver at 40m depth.*
(b) Vertical particle motion v_z of the Boulogne VSP data for the receiver at 40m depth.

At first sight, the data has the correct characteristics. The amplitudes in the v_z are stronger than in the v_x, which can be understood from the fact that in first approximation the v_z represent the P-waves and the v_x the S-waves. Furthermore, in both the v_x- and the v_z-data clear reflections are visible, however for VSP data, the quality is not exceptionally high. The main problem in the data is encountered in the near-offset area. From Fig. 5.13 we can see that there is a time-shift and scaling of the seismic events up to a source-offset of 4.5m. Given the almost horizontal layering of the sediments and the non-disturbed flat beach, we suspect that this effect is caused by a residual deformation of the subsurface due the weight of the platform that was built to drill the bore-hole.

The result of applying the decomposition into P- and S-wave potentials, followed by the separation into up- and downgoing wave field potentials is shown in Fig. 5.14. Again a top mute of 7ms was applied to remove some strong anti-causal noise, which was generated by the processing.

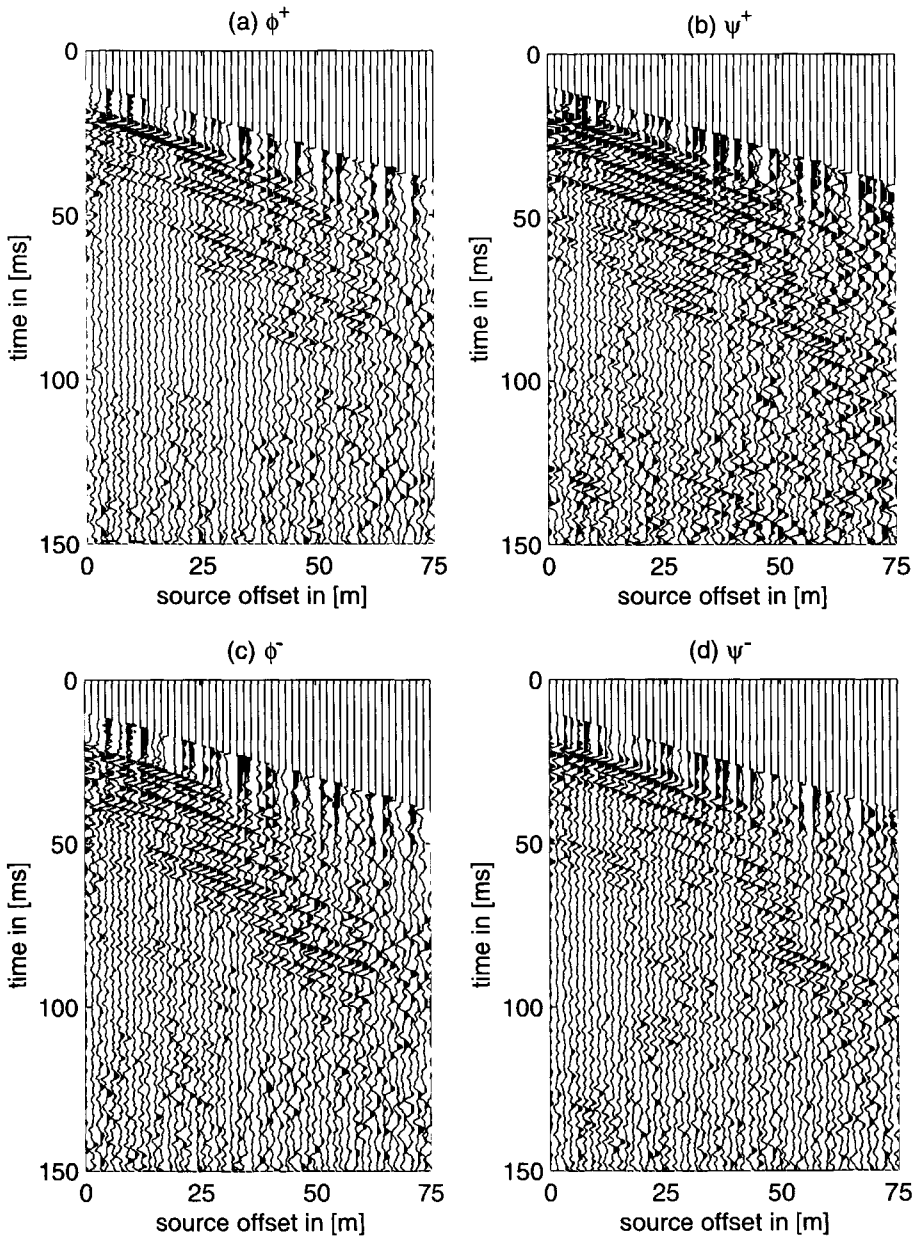

Figure 5.14: *Up- and downgoing P- and S-wave potentials for the receiver at 40m depth, constructed by median filtering. (a) The downgoing P-wave potential ϕ^+ (b) The downgoing S-wave potential ψ^+ (c) The upgoing P-wave potential ϕ^-. (d) The upgoing S-wave potential ψ^-.*

When we look at the results of this processing, we see that the time-shift and scaling in the near-offset range has affected the continuity of the reflections considerably. This problem has to be solved before we can perform the imaging and characterization. In the next section we will apply a homogenization to the near-offset area of the data set.

Outside the near-offset range, comparing the downgoing ϕ^+ and ψ^+ with the upgoing ϕ^- and ψ^-, respectively, we see some clear differences. Notably, the first arrival in the downgoing wave fields is much stronger than in the upgoing wave fields. In the downgoing S-wave (ψ^+) section there is an event at around 40ms, which is absent in the upgoing ψ^+. These are clear evidence that the applied processing has been able to separate at least a major part of the up- and downgoing events.

The separation into P- and S-wave potentials is more difficult to assess. Looking carefully at the upgoing wave fields, we can recognize more and stronger events in the range of $t = [40\text{ms},70\text{ms}]$ in the ϕ^- than in the ψ^-. However, the quality of the decomposition into up- and downgoing wave field potentials can only be assessed quantitatively by applying the proposed imaging and characterization technique of Section 5.3. This will be the topic of the next section.

5.6 Imaging of the rayparameter-dependent upgoing wave field potentials of the Boulogne VSP data

In this section, the two imaging techniques presented in Section 5.3 are applied to the Boulogne walk-away VSP data. The first step is the application of the Radon transform to the upgoing wave field potentials ϕ^- and ψ^-. In this respect we encounter the first problem, as the near-offset range is heavily affected by the time-shift and scaling of the recorded wave fields. This will strongly affect the result of performing the Radon transform, as the near-offset irregularities will smear out over all rayparameters.

To solve this problem, we apply a normal move-out (NMO) correction to the data sets, choosing a move-out velocity of 2000m/s, for both the P- and the S-wave potentials. The data is mirrored to the negative offsets, to arrive at a semi-splitspread data set. For the S-wave potential, the data at negative offset are multiplied by a factor of -1, to take into account the polarity change normally encountered in split-spread S-wave recordings. In

these data sets we mute the affected near-offset ranges. Then we perform a linear interpolation in the muted areas for the P-wave potentials. The muted areas in the S-wave potentials are interpolated by a sine interpolation, to create a smooth transition between the positive and negative offsets. After this muting the data is inverse NMO corrected, to arrive back at the common-receiver gathers.

The second problem is the fact that the data are spatially aliased in the frequency range in which the data is recorded (50-1000Hz). Obviously, the spatial aliasing is caused by the fact that the source spacing is too large (the data were recorded with a source spacing of 1.5m). Referring to Dobrin and Savit (1988), the preferred maximum shot-spacing is given by

$$\Delta x_{\max} = c_{\min}/2f_{\max}, \tag{5.11}$$

where $\Delta x_{\max}$ is the maximum shot-spacing, $f_{\max}$ is the maximum frequency where data is recorded and $c_{\min}$ is the minimum velocity in the subsurface. In our case, where $f_{\max} \approx$ 1000Hz and $c_{\min} \approx$ 1900m/s, this would lead to a preferred maximum shot spacing of $\Delta x_{\max} \approx$.95m. However, this was not feasible in the walk-away VSP experiment. We can however interpolate traces in between the recorded traces, before applying the Radon transform. In our situation this is performed by linear interpolation in the NMO domain, right after the muted zones are interpolated.

After the above interpolation steps have been performed, the data are transformed to the Radon domain. Note that quantitatively analyzing data in the (p, τ)-domain is only valid in the 1-D approximation. Further, in Chapter 2, Section 2.2, it was noted that in applying the Radon transformation to seismic reflection data, we assume a line source in the crossline direction. The data in this experiment is, however, generated by a point source. To correct for this difference, we normally apply a spatial filter to the shotrecords, to put a relative gain to the far offsets. However, as we can see in Figs. 5.13a,b, the noise level at far offsets is quite high. Hence, applying this filter increases the noise level in the data considerably, such that the imaging results are seriously affected. Therefore, we have decided not to apply this filter to the data. The consequence of this is that the contrasts that are estimated in the Linearized Zoeppritz Inversion are generally somewhat larger. However, as only the small offsets are taken into the inversion (maximum angle of incidence of 30 degrees), the error made is only of a few percent. Further, as the multiscale characterization is focused on the relative velocity contrasts, we expect that this does not affect the inversion results.

Because of the fact that the dips in the Boulogne field are very small, we can assume that this approximation is valid for this data set.

The first imaging approach is the construction of depth images $\mathsf{R}_{PP}(p,z)$ and $\mathsf{R}_{SP}(p,z)$. As a background P-wave velocity model, we have used a constant velocity of 2000m/s, as the core velocities are not representative for the actual velocity profile. This choice for the velocity is based on the slope of the down-going P-wave in the common-source gathers at a small offset (9m) from the borehole. The reason for not using the core velocities is that they are measured at surface pressure and not at depth, therefore we expect that the core velocities lack the DC component which should be added because of the ambient pressure at depth. In multiscale characterization, this does not trouble us, as we will perform the analysis on the velocity contrast function $D(z)$, which is insensitive to this DC component. The S-wave velocity is estimated, using some empirical results by Hardage (1983), which gives as a mean for 50% consolidated limestone and 50% non-consolidated clay an S-wave velocity of about 900m/s.

Figures 5.15/5.16b show the results of the conventional imaging approach for the topmost receiver at 2m depth for the P-P and P-S data respectively. This imaging result shows clear horizontal reflections, however they are blurred by many internal multiples and therefore especially the deeper reflections are hidden behind the multiple arrivals. The match between the P-wave velocity profile in Fig. 5.15a and the image R_{PP} in Fig. 5.15b is only visible up to around 50m depth, beyond this depth there is little correlation between the well-log and the image. Next to the $\mathsf{R}_{SP}(p,z)$ in Fig. 5.16b, the P-wave velocity profile is plotted. Because only the P-wave velocity profile is available, a reliable analysis of the match between the well-log and the seismic data is not possible.

The second imaging approach is the application of the piecewise imaging scheme discussed in Section 5.3.1. The 63 depths z_i of the receivers for which the piecewise constructed images $\mathsf{R}^{\mathrm{pw}}_{PP}(p,z)$ and $\mathsf{R}^{\mathrm{pw}}_{SP}(p,z)$ have been created range from 2 to 126m, with a 2m depth spacing. Figures 5.15/5.16c show the results of the piecewise imaging. It is clear that this imaging technique has decreased the amount of imaged internal multiples drastically. At many points were the P-wave velocity changes rapidly, we see reflection events in the piecewise constructed image $\mathsf{R}^{\mathrm{pw}}_{PP}$ (Fig. 5.15c), where in the image R_{PP} in Fig. 5.15b the deeper events do not correlate at all. For both piecewise constructed images, the deeper reflections are stronger than in the conventional imaging results in Figs. 5.15/5.15b.

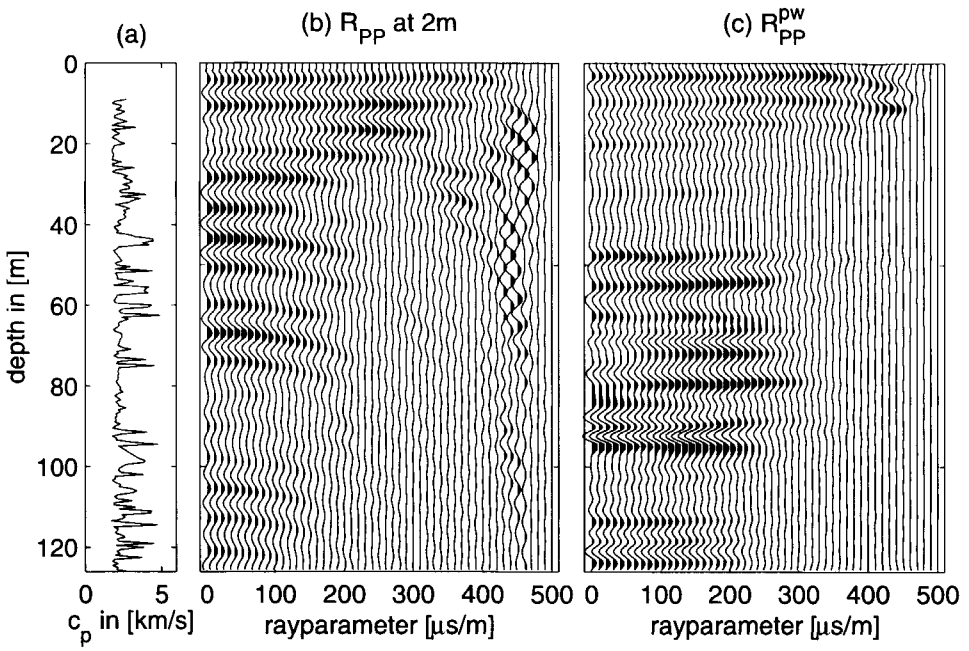

Figure 5.15: *(a) P-wave velocity profile as measured from the core.*
(b) rayparameter-dependent depth image of the P-wave potential ϕ^- from receiver at 2m depth.
(c) rayparameter-dependent piecewise constructed depth image of the P-wave potential ϕ^-.

The next section covers the multiscale analysis of the velocity contrast functions derived from the images acquired by both imaging approaches.

5.7 Multiscale characterization of the Boulogne walk-away VSP data

The multiscale characterization of the rayparameter-dependent images of *P-P* in Figs. 5.15b and c is performed according to the approach discussed in Section 5.3.2.

Figure 5.17a shows the *P*-wave velocity profile, as measured from the core, with a 1cm sampling. Note the interpolated areas in the velocity profile around 48 and around 95m depth. At these points, unconsolidated clays are

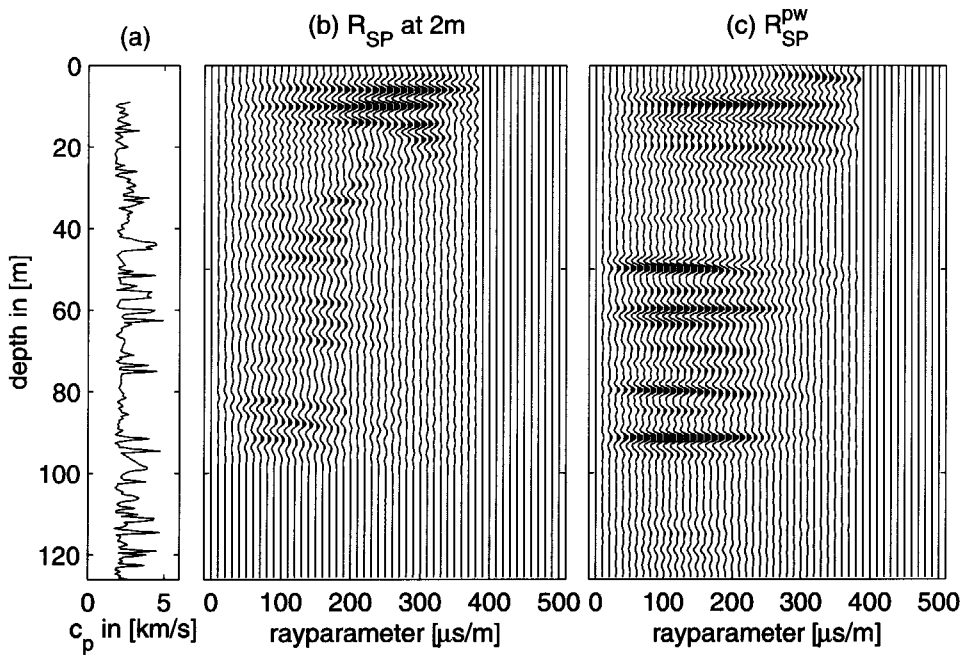

Figure 5.16: *(a) P-wave velocity profile as measured from the core.*
(b) rayparameter-dependent depth image of the S-wave potential ψ^- from receiver at 2m depth.
(c) rayparameter-dependent piecewise constructed depth image of the S-wave potential ψ^-.

present in the Boulogne stratigraphy, which made it impossible to recover the core. Furthermore, from the topmost 8.7m of the borehole the core was also not recovered, most probably because this was the thickness of the sand-layer at the beach. Figure 5.17b shows the same velocity profile, sampled down, after applying a low-pass filter, to a spatial sampling of $\frac{1}{2}$ feet (i.e. .1524m). This down-scaling makes it easier to recognize the reflecting boundaries in this well-log. Figure 5.17c shows the velocity contrast function derived from the velocity profile in Fig. 5.17b. The background velocity $\bar{c}_P(z)$ was taken at a constant value of 2000m/s. This velocity contrast function will be referred to as $D_{c_P}(z)$.

Following, the velocity contrast functions are derived from $R_{PP}(p,z)$ with the receiver at 2m depth and from $R^{pw}_{PP}(p,z)$, by applying the Linearized Zoeppritz Inversion of Van Wijngaarden (1998). These velocity contrast

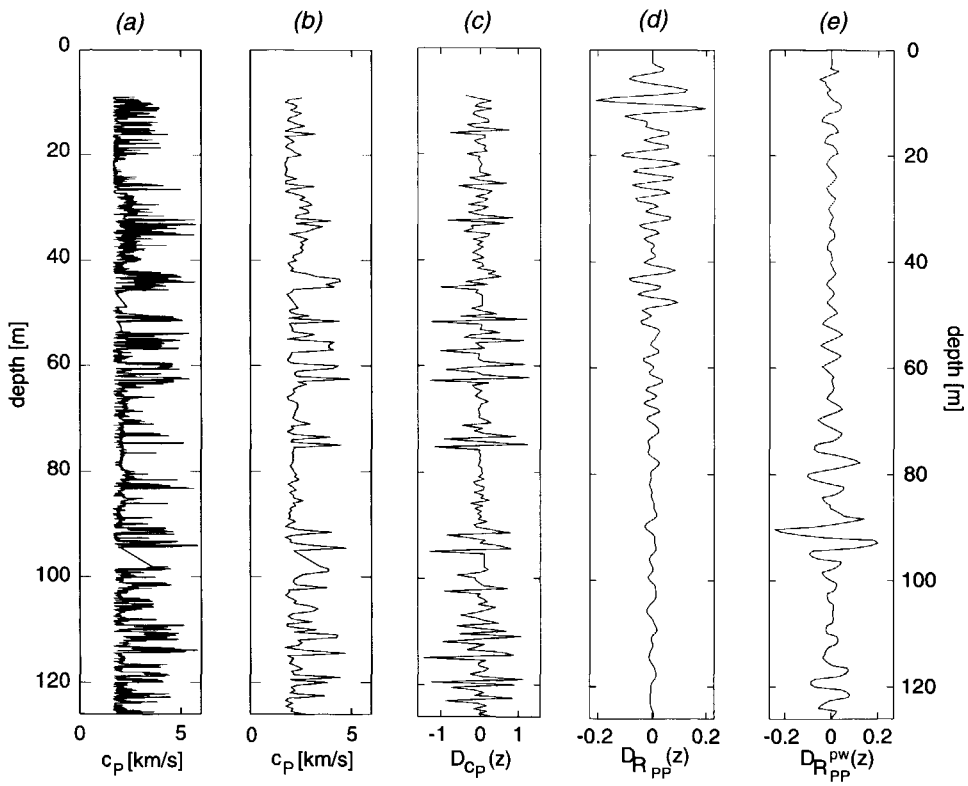

Figure 5.17: *(a) The P-wave velocity profile, as measured from the core.*
(b) The P-wave velocity profile, sampled down to a spatial sampling of 0.1524m.
(c) The velocity contrast function $D_{c_P}(z)$, constructed from the velocity profile in (b).
(d) The velocity contrast function $D_{R_{PP}}(z)$, derived from $R_{PP}^{pw}(z_{rcc} = 2m)$ depth.
(e) The velocity contrast function $D_{R_{PP}^{pw}}(z)$, derived from R_{PP}^{pw}.

functions are referred to as $D_{\mathsf{R}_{PP}}(z)$ and $D_{\mathsf{R}^{\mathrm{pw}}_{PP}}(z)$, respectively. Both velocity contrast functions, together with the $D_{c_P}(z)$ derived from the core velocities are shown in Fig. 5.17c-e. It is clear that the velocity contrast function $D_{c_P}(z)$ in Fig. 5.17c has a higher spatial frequency content than the $D_{\mathsf{R}^{\mathrm{pw}}_{PP}}(z)$ and $D_{\mathsf{R}_{PP}}(z)$ derived from the images. In multiscale analysis this is corrected for by taking the same scale range in the analysis for both types of velocity contrast functions. Already the quality of the piecewise constructed image shows off: many strong events (e.g. around 75 and 90m) in $D_{c_P}(z)$ are also visible in $D_{\mathsf{R}^{\mathrm{pw}}_{PP}}(z)$, but not in $D_{\mathsf{R}_{PP}}(z)$. The inversion results are further assessed by applying a multiscale analysis to these velocity contrast functions.

For the comparison between estimates of α from well-log and seismic data, the semi-continuous α-profiles are computed by multiscale analysis (cf. Section 5.3.2). Figure 5.18a shows the estimates of α from the depth image R_{PP}, the estimates of α from the depth image $\mathsf{R}^{\mathrm{pw}}_{PP}$ are displayed in Fig. 5.18b; both are depicted by the black line. The grey lines represent the estimates of α from the velocity contrast function $D_{c_P}(z)$, derived from the core velocities (Fig. 5.17a-c). The black double-headed arrows depict the areas in which the velocity contrast function $D_{c_P}(z)$ shows strong contrasts. We expect that in these areas the estimates of α from the images are more reliable than in the areas where there are only weak contrasts, because the signal-to-noise ratio is higher.

If we look at Fig. 5.18a, we see that the estimates of α from the image $\mathsf{R}_{PP}(z_{\mathrm{rec}}{=}2\mathrm{m})$ (the black line), show hardly any correlation with the estimates from the core velocities (the grey line) in the supposed reliable areas. Only the general trend of the α-profiles seems to be similar. This shows that the multiple events in the VSP data affect the multiscale behavior of the R_{PP} considerably.

If we compare the results of Fig. 5.18a with those from Fig. 5.18b, we see that the estimates of α from the image $\mathsf{R}^{\mathrm{pw}}_{PP}$ show a much better correlation with the α-estimates from the core velocities, within the areas depicted by the double-headed arrows. Only some minor depth-shifts are present, when we compare the α-profile from the piecewise constructed image to the estimates of α from the core velocities. This can be explained by taking into account the simple background velocity model ($\bar{c}_P(z) = 2000\mathrm{m/s}$), which was used for imaging the VSP data. Generally speaking, the piecewise imaging scheme has supplied us with a much more reliable image of the subsurface than the conventional scheme.

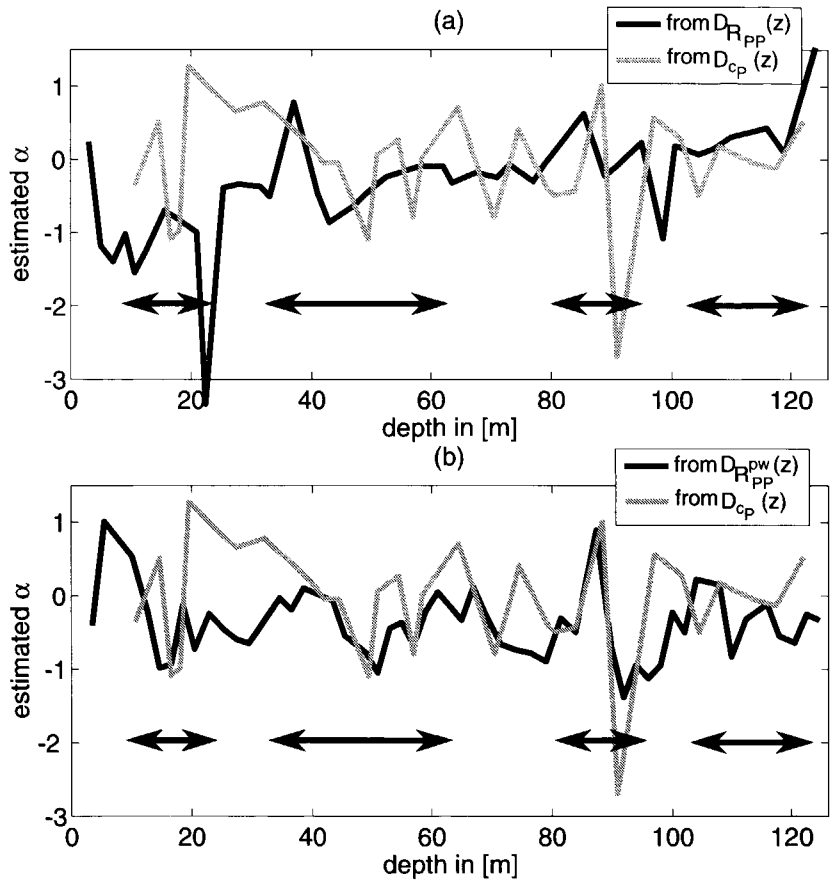

Figure 5.18: *(a) Profile of α as a function of depth, derived from the velocity contrast functions $D_{R_{PP}}(z)$ (black) and from $D_{c_P}(z)$ (grey).*
(b) Profile of α as a function of depth, derived from the velocity contrast functions $D_{R_{PP}^{pw}}(z)$ (black) and from $D_{c_P}(zz)$ (grey).

5.8 Conclusions

A multiangle, multiscale imaging and characterization method for walk-away VSP data has been proposed and was performed on synthetic and real data.

It was shown that from particle velocity wave fields v_x and v_z, the up- and downgoing P- and S-wave potentials $\phi^{\pm}(x,z,t)$ and $\psi^{\pm}(x,z,t)$ can be constructed. First a decomposition in ϕ and ψ is performed, by applying an explicit polarization scheme, followed by a separation into up- and downgoing fields, by means of a median filter technique.

These data sets have been the input of two imaging schemes. The first scheme is a conventional approach to construct depth images $\mathsf{R}_{PP}(p,z)$ and $\mathsf{R}_{SP}(p,z)$ for each receiver. The second approach combines the images from each receiver, to construct piecewise constructed depth images $\mathsf{R}^{\mathrm{pw}}_{PP}(p,z)$ and $\mathsf{R}^{\mathrm{pw}}_{SP}(p,z)$ that contain less internal multiples than the images constructed from the data received at only one receiver. Furthermore, the amplitudes are better preserved in these piecewise constructed images, as the upgoing transmission paths are shorter.

The depth images $\mathsf{R}_{PP}(p,z)$ (from the topmost receiver) and $\mathsf{R}^{\mathrm{pw}}_{PP}(p,z)$ have been analyzed by a multiangle, multiscale characterization method. To this end, velocity contrast functions were derived from both images, by applying Linearized Zoeppritz Inversion. Also from the P-wave velocity profile, a velocity contrast function was constructed. Following, a multiscale analysis was applied to construct singularity parameter (α) profiles for each of these velocity contrast functions. It was shown that the multiscale behavior of the P-wave velocity profile, for these data, could be recovered from accurately imaged seismic reflection data.

Further, by comparing the estimates of α derived from the conventional and the piecewise constructed image with the ones derived from the P-wave velocity profile, we found a better correlation for the piecewise constructed image. This confirms that the novel imaging scheme preserves the rayparameter-dependent reflectivity better than the conventional scheme.

Chapter 6

Multiscale characterization of shallow S-wave data and CPT data

The work reported in this chapter is the result of a fruitful cooperation between dr. Ranajit Ghose and the author of this thesis. The method of multiscale analysis of velocity contrast functions is applied to shallow S-wave reflection data, and is correlated with results of applying the method to Cone Penetration Test (CPT) cone resistance. It is shown that singularity parameters, estimated from CPT q_c show a good correlation with singularity parameters, estimated from velocity contrast functions, constructed from shallow S-wave reflection seismics. In this chapter, the primary goal is to use the singularity parameter α to recognize lateral variation of soil strength along a boundary. The results presented show that an application in geotechnical site characterization is possible.

6.1 Introduction

A good knowledge of the subsoil is crucial in any underground utilization project. In particular, the distribution of the in-situ soil strength is an important requisite in all foundation and stability problems. With growing demand for underground space utilization, there is also an increasing number of incidences of structural damages accompanied by other collateral losses due to improper engineering design and planning, resulting from insufficient knowledge of the subsoil condition.

A major concern in soil characterization is whether the soil is tested in its natural physical, chemical and biological environment. Soil samples are usually collected in boreholes and tested in laboratories. However, because of the basic nature of soil, soil samples are often significantly disturbed from their in-situ condition. Common causes of disturbances to the sample are

mechanical disturbance during drilling, sampling, transportation, storage and handling in the laboratory, changes in water content and stress conditions, possible chemical changes, and mixing and segregation of the soil constituents. In particular, where cohesionless (sandy) soils are encountered, it is not possible to obtain reliable soil characteristics using conventional sampling and laboratory testing methods.

To ascertain the in-situ, geomechanical properties of the soil, the two common approaches are, (a) the use of the seismic methods, and (b) direct probing using static and dynamic penetration devices. Seismic tests are among the few in-situ tests that produce little or no soil disturbances, and provide information of the mechanical properties of the soil, important to the engineers. Seismic methods measure the very-small strain elastic properties of the soil that are important in response analysis for small-strain dynamic loads. However, the large-strain failure properties of the soil, such as shear strength (S_u), relative density (D_R), and friction angle (ϕ) of sand, are not directly addressed by seismic methods. These strength properties are essential in foundation engineering (bearing capacity estimation) and in all problems involving earth pressure, landslides, liquefaction due to earthquakes, and stability of slopes in cuts and fills. For such purposes, the penetration tests are best suited. Penetration methods involving direct push technology are the most rapidly developing geotechnical site characterization techniques. The direct push devices produce little overall disturbance. The most widely used static and dynamic penetration tests are respectively cone penetration test or CPT (for soft soils) and standard penetration test or SPT (for relatively hard soils).

The most popular test for geotechnical investigation in soil is CPT. In recent years the use of CPT has dramatically increased. For instance, only in the Netherlands (including the offshore territory) there are nearly 100,000 CPTs carried out each year [Barends et al. (1999)]. In CPT, a cone at the end of a series of rods is pushed into the ground at a constant rate and measurements are made of the resistance to the penetration of the cone, also known as 'cone resistance' or q_c, which is the total force (Q_c) acting on the cone divided by the projected area (A_c) of the cone. The cone resistance, q_c is a direct indicator of the strength of the soil at a given depth. Cost-efficiency, speed, simplicity, reliability, and the ability to provide near-continuous information of the soil properties with depth are the important reasons for the increasing popularity of CPT. The primary significance of CPT comes from the fact that it represents a miniature driven pile or foundation in soil, and

hence the pile bearing capacity (pressure between a foundation and the soil which will produce shear failure in the soil) can be directly estimated from q_c. CPT provides, thus, valuable constraints for all settlement and stability calculations for soil. CPT q_c responds to soil changes within 5 to 10 times the cone diameter (standard diameter 35.6 mm) above and below the cone, the distance increasing with increasing soil stiffness [Meigh (1987)]. The three main applications of CPT are: (i) to determine the soil stratigraphy and identify soil composition (using charts), (ii) to estimate important geotechnical parameters like S_u, D_R, or ϕ of sand (unfortunately none measured directly by CPT, but is derived indirectly using empirical relations that are limited in the range of applicable soils), and (iii) to provide results (such as bearing capacity) for direct geotechnical designing.

With regard to uncertainties inherent to the process of engineering design, those related to soil properties are among the most notorious ones. Prediction of displacement, deformation, stress-distribution, and failure of a structure are all subject to these uncertainties, because of the spatial variability of the relevant geomechanical parameters. A realistic soil model is, thus, of great importance to any engineering evaluation. Models of geomechnical parameters can be process-based, stochastic, or probabilistic; also various hybrid forms are in use. Both the non-linear behavior and the high spatial variability make it impossible to predict the exact behavior of soil in time and space, and therefore call for adoption of a factor of safety that ensures an adequate margin against unexpected deviations in the predicted performance.

In particular, the lateral variability of the geomechanical parameters is of prime concern. Lateral variability of soils is determined by the geological processes during deposition of the sediment and the diagenesis afterwards.

Although CPT provides valuable information of the strength of the soil as a function of depth, the information is restricted to the CPT location. CPTs are commonly measured several tens to hundreds of meters apart. Large lateral variations in soil generally take place within a significantly shorter distance. It is obvious that soil models based on sparse CPT information contain unrealistically large errors. Recently, field tests using horizontal CPTs have uncovered the striking fact that horizontal variability in soil strength can be comparable in magnitude to the vertical variability [Van Deen et al. (1999)]. Soil models based on lateral interpolation of CPT data collected at a few locations at a given site obviously contain large uncertainties, which translates into large risk in the design of an engineering structure.

To overcome this problem, in recent years there have been attempts to check whether shallow, high-resolution, seismic reflection methods, particularly those using shear waves, can be used to define the lateral continuity or variability of the soil layers of different strengths as seen by CPT, [e.g., Ghose et al. (1996, 1998); Brouwer et al. (1997)]. The relevance of shear waves for prospecting soft soils is well-known. Unlike compressional waves, shear waves are sensitive mainly to the solid grains and their interaction, which control the mechanical behavior of soil. Namely, the shear modulus is not influenced by the pore-filling if its shear modulus is zero. For increasing fluid saturation, we do have an increase in density, which mildly decreases the shear wave velocity [see Schön (1996)]. Shear wave velocity, c_S has indeed been found to correlate better with the engineering properties of the soil than the compressional wave velocity, c_P [e.g., Imai and Tonouchi (1982)]. Further, since the c_P/c_S ratio in the soft soil is generally high (5$\sim$7), for the same observed frequency, shear waves have much shorter wavelength than the compressional waves, and thus offer higher resolution. On the other hand, the penetration depth of shear-waves is generally less than that of compressional waves. However, the observed penetration depths of shear waves ($>$ 40 m) are more than sufficient for geotechnical applications.

Possible extraction of the fine-scale nature of variation of the soil strength as seen by CPT from the S-wave seismic reflection data holds the key to the derivation of a 2-D distribution of soil strength along an interface which is of vital interest to the geotechnical engineers.

In order to achieve this, the first requirement is a valid, quantitative means to relate seismic reflections to CPT data. In this chapter, we propose a new concept to relate the shallow, S-wave reflections to CPT data by means of the multiangle, multiscale analysis of both CPT and velocity contrast functions, derived from S-wave seismic reflection data. Further, we extend this approach to map the fine-scale *lateral* variability of a subsoil interface, and present results of extensive field experiments, including multiple CPTs.

6.2 Relating S-wave reflection to CPT: physics and earlier observations

Seismic methods measure the small strain response of a relatively large volume of the ground, whereas the penetration of the cone measures locally the large strain response of the ground, since the average stress levels around

the cone approximately equals failure of the soil. Thus, seismic and CPT represent respectively very different soil properties that correspond to very different levels of strain. Figure 6.1 schematically illustrates the order of strains corresponding to various measurements, including seismic and CPT, and the nonlinear strain-dependency of soil deformation. Seismic S-wave

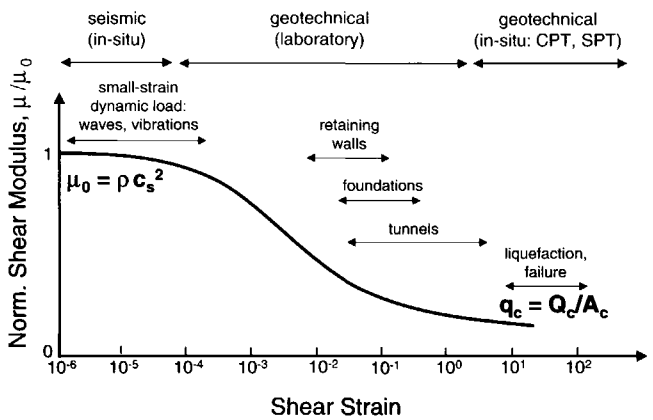

Figure 6.1: *Schematic illustration showing various soil testing approaches corresponding to various strain levels and various problem areas. Note that seismic and CPT represent, respectively, two extreme ends of this very large range of strain, and hence they indicate very different soil properties. Here, μ_0 is the very small strain (elastic) shear modulus, μ is the shear moduls at larger strains, and q_c is the CPT cone resistance.*

velocity c_S relates to the very-small strain ($10^{-5} - 10^{-6}$) elastic properties of the soil, specifically the rigidity or the small-strain shear modulus (denoted by μ by the geophysicists and by G_0 by the engineers), while CPT q_c represents the failure or strength properties of the same soil at very large strain (> 10) - thus a strain difference in the order of a million.

The physics relating c_S to q_c is not straight-forward. There are two main lines of reasoning which address the physics of the relation between c_S and q_c. The first indirect indication comes from the theory of critical state soil mechanics [e.g., Schofield and Wroth (1968); Roscoe and Burland (1968);

Sladen et al. (1985); Muir Wood (1990); Collins (1990); Jefferies (1993); Yu (1994, 1998); Robertson et al. (1995); Fear and Robertson (1995)]. Small-strain shear modulus μ and CPT q_c are both independent of stress and strain history. According to critical state theory, at critical state (when a soil deforms without any volume change) and assuming undrained shear and no pore pressure redistribution (generally a valid assumption for CPT, considering the speed of penetration of the cone - 2 cm/s) and hence no change in void ratio, the strength (and hence CPT q_c) of a sandy soil of a given compressibility is controlled by the initial void ratio or porosity, which, in turn, defines the soil state parameter [Been and Jefferies (1985)]. For a given soil type, the soil state parameter and the effective stresses determine c_S [Sasitharan (1994); Cunning et al. (1995); Robertson et al. (1995)]. For (approximately) normal-incidence shear waves, horizontal stresses are important [e.g. Dillen (2000)]. Now, there is evidence that CPT q_c is also more strongly dependent on horizontal stress than mean stress [Baldi et al. (1986); Houlsby and Hitchman (1988)]. These arguments indirectly explain the relationship between c_S and q_c. However, while compressibility does not significantly affect c_S, it greatly affects q_c, and hence there cannot be a unique relationship between c_S and q_c, but the relationship will be soil-specific, as it is indeed observed on field data. The second explanation comes from the modeling of the cone penetration process using the cavity expansion theory [see Salgado et al. (1997); Yu (2000)]. The theory describes the penetration process in terms of an expanding cavity in soil, with plastic deformation in the immediate vicinity of the penetrating cone, followed successively by the non-linear elastic and the elastic zones of deformation, radially outwards from the axis of the cone [see Salgado et al. (1997)]. The soil properties in each of these three zones contribute to the observed q_c. Since c_S represents an important intrinsic property of the soil in the elastic zone of deformation, it will have influence on q_c, which can be estimated [Ghose and Drijkoningen (2000)]. Modeling in the free-field condition, constrained by real field data, has shown that for a given sandy soil a relative increase of c_S by 9% [165 m/s to 180 m/s] corresponds to an relative increase of q_c by slightly more than 10%.

Despite the fact that c_S and q_c are physically very different quantities and the physics behind their relation is complex, with the advent of seismic CPT (where both c_S and q_c are measured by the same cone containing a 3-component geophone in addition to the pressure transducers), in recent years there have been a number of careful and extensive field experiments

at very different locations, which consistently show the existence of a power-law relation between c_S and q_c [e.g., Eslaamizaad and Robertson (1998); Goutbeek and Muijs (1999); Simonini and Cola (2000)]. Based on these observations, a number of empirical relationships has been proposed. These relationships depend greatly on the nature of the soil (sandy or clayey) and the state of compaction, and are site-specific. Characterization of the fine-scale nature of interfaces in q_c and c_S fields will enable one to relate the two observations, and can be used to resolve variation in soil strength over an interface.

6.3 Mapping lateral variability of a strength interface in soil: geotechnical importance

In all projects pertaining to large infrastructures and buildings, like underground storage and transportation facilities, tunnels, roads, railways, subways, airports, harbors, and underground city expansion, a knowledge of the distribution of the soil layers of various strengths is of vital importance. The presence of various weak and compressible layers at shallow depths, particularly peat and clay, is problematic from the stability and construction points of view. The thickness and lateral continuity of these cohesive layers, interspersed between sand and gravel layers, are important constraints in site and safety evaluations. As a well-known example, the leaning of the Tower of Pisa in Italy is attributable to the distribution and the lateral variations of the thickness and properties of the clay and sand layers in the subsoil [Rampello and Callisto (1998)]. The design and construction of subways and other large underground tunnels also largely depend on the lateral continuity and the thickness distribution of the soil layers of varying strengths [e.g.,Schiphouwer et al. (1999); Van Kessel et al. (1999)].

The distribution of shear strength over a subsoil interface varies laterally, as can generally be seen in CPT data [e.g., Lunne et al. (1997); Rampello and Callisto (1998)]. Often the transition of shear strength over a given interface is gradual; however along this interface this nature of transition can change from gradual to a step-like one, or sometimes even a thin layer of unexpectedly low or high strength may appear at the interface.

Lateral variations in cohesion and pore-pressure along a subsoil interface, commonly associated with strength variations, can be significant, and have important implications on engineering design and risk analysis. The knowledge of such lateral variation of the interfacial nature is important for three

primary reasons:

1. Critical decisions regarding foundation and safety are made based on the estimated depth and thickness of a layer of given strength. However, the estimates of the depth and thickness depend on the vertical and lateral definition of the layer, which is by itself characterized in terms of its strength.

2. Lateral variation in the fine-scale nature of a subsoil interface indicates variation in the processes of sedimentation and diagenesis, which is important information in any process-based, spatial soil modeling.

3. Information of the fine-scale lateral variation of the nature of the interface is important for interpolating sparsely sampled information such as CPT q_c.

6.4 Integrating S-wave reflection to CPT: the multiangle, multiscale approach

The highest resolution obtained from conventional, high-frequency reflection surveys on soft soils is in the range of 0.75 m to 1.0 m. Such resolutions are normally evaluated on seismic trace data. But it is the fine-scale c_S variation that is expected to correlate with the observed variation of q_c, and not the amplitude variation in the CMP stacked traces, where high frequency events are often not visible for their small amplitudes. The tangibility of the correlation between the depth distribution of c_S and that of q_c calls for a fine definition of the c_S field so as to bring the latter as close as possible to the high resolution of the CPT q_c data (q_c sampling being at every 2 cm). From the results of modeling of the cone penetration process in the free-field condition and from field-observed empirical relations it is clear that in order to relate shallow, shear-wave reflection data to CPT, based on a quantitative criterion (and not empirically), one needs to extract the fine-scale velocity information present in the reflection data as detailed as possible. Seismic reflection data usually have frequencies higher than those resolved by the semblance velocity analysis. The resolution of the c_S field obtained from the conventional techniques of velocity analysis for stacking is low (Fig. 6.2). Therefore, this velocity information is generally not useful for geotechnical applications. Further, the variation of q_c at an interface is generally not steplike, as can be seen in Fig. 6.2b, e.g. at 4 and 9m depth. We recognize the

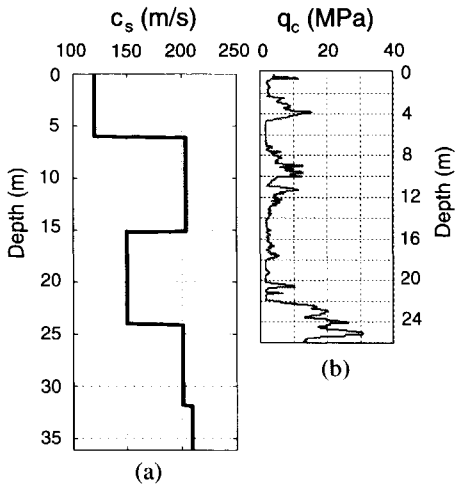

Figure 6.2: *Illustration showing the large disparity in resolution between (a) the RMS velocity field obtained by conventional velocity analysis of seismic reflection data, and (b) CPT cone resistance, q_c. High q_c indicates sandy soil, low q_c implies clayey soil. One needs to extract any fine-scale velocity information present in the seismic reflection data in order to relate it reliably to the higher-resolution CPT data.*

strong resemblance of q_c with well-logs of seismic velocities (e.g. Fig. 4.2 in Chapter 4). Although the CPT q_c exhibits a power-law relation with c_S, we can, for relatively small q_c contrasts, approximate this by a linear relation. Therefore, the multiscale analysis of well-logs, as presented in Chapter 2 is applied to the CPT q_c functions to estimate singularity parameters α for its singular points. These estimates are then used to correlate the local scaling behavior of CPT q_c with velocity contrast functions, derived from S-wave seismic reflections, applying the method presented in Chapter 4.

The method is set up as follows. First the lateral course of a reflector in the stacked and depth-converted seismic section is identified. Then, for every CMP location, the identified depth in the stacked section is marked in the c_S contrast field, which is constructed from the field data by Linearized Zoeppritz Inversion [see Chapter 4, Section 4.3]. The corresponding modulus maxima lines in the wavelet transform of the c_S contrast function at the specific CMP is picked, along which the local singularity exponent α for the seismic data is measured. Any change of the nature of the interface is thus characterized by a change of the value of the singularity parameter α, where

the lateral resolution is now far better than the CPT spacing. However, the CMP spacing in shallow seismic reflection surveys is usually smaller than the width of the Fresnel zone. Hence, we can not expect that the resolution of the c_S contrast field is identical to the CMP spacing. Given the observed relation between CPT and seismic (which may be confirmed in the field), one can now use the distribution of the α parameter to determine the lateral variation of CPT q_c along a subsoil interface, and hence can deterministically interpolate the CPT q_c in the lateral direction.

6.5 Tests on field data

In this section, we apply the above technique to two field datasets that are acquired at sites with marked lateral variations in the subsoil.

6.5.1 Experiment 1: Field setting and acquisition parameters

Field experiments involving both shallow, shear-wave reflection profiling and a CPT were carried out at a site located in the western part of the Netherlands, near Rotterdam. The site was grass-covered with the water-table at less than a meter depth. The geology of this site is known from earlier borehole measurements and is comprised of flat, alternating layers of Holocene clay and sand continuing up to a depth of 22-25 m where stiff, Pleistocene sand is encountered. The Pleistocene sand is relatively homogeneous. In the topmost part, the appearance of sand layers at around 1-2 m, 4-5 m and 7-12 m depths has been marked in a number of boreholes. Table 6.1 shows the acquisition parameters for the first experiment.

The CPT was carried out close to the beginning of the seismic line, but for practical reasons it could not be located exactly on the seismic line. Hence, the analysis performed for the first experiment is more focused on the stability of the multiscale analysis with respect to multiple CMP locations, than on the actual correlation of seismic reflection data with CPT q_c. In experiment 2, the CPTs were measured right on the seismic line, such that a quantitative correlation could be performed.

Figure 6.2b shows the CPT cone resistance (q_c) in MPa. The distance between the CPT measurent and the seismic line is about 100 m. The soil layers at this site are known to be almost horizontal, and hence the main features seen in the CPT data are representative of the entire site. High q_c represents sand layers and low q_c represents clay/peat layers. The presence of various

Shallow shear-wave seismic reflection	
S-wave source:	sledgehammer
Receivers:	10 Hz* crossline horiz. geophones, 48 ch.
Vertical stack:	2
Shot interval:	2.0 m
Receiver interval:	0.5 m
Min. S-R distance:	0.5 m
Data sampling:	0.5 ms
Total profile length:	$\sim$ 190m
Cone Penetration Test: 1 measurement	
Depth:	26 m
Location:	$\sim$ 100 m away from the seismic line

*This is the natural (or resonance) frequency of the geophone

Table 6.1: *Acquisition parameters of experiment 1*

thin sand lenses at shallow depths (depth $<$ 13 m) is clear in the CPT data; at the Holocene-Pleistocene boundary at around 22-25 m depth, the CPT q_c sharply increases (Fig. 6.2b), representing the major change in soil strength. It is also evident that this primary interface in the subsoil does not represent a step-like change in strength, but it is a composite interface composed of a number of thin sand layers of progressively increasing strength.

6.5.2 Preprocessing of S-wave reflection data

Careful amplitude-preserved preprocessing was carried out on the S-wave reflection data. Preprocessing involved primarily trace-editing (kill/reverse), deconvolution, surface wave elimination, and multiple removal. Surface waves are dispersive and they have linear moveout in the shot gather. At first linear moveout (LMO) correction was applied using the phase velocities of the surface wave events, and then careful (f, k)-filters (polygons) were designed and applied to eliminate these nearly infinite-velocity (after LMO) surface-wave events. A subsequent inverse (f, k)-filter restored the filtered shot gathers, that contained now primarily the S-wave reflections. This processing was carried our interactively to tackle the spatially varying surface waves and to prevent any artifacts or distortion. This approach was found quite effective in removing the surface waves, which have different velocity

than the shallow, S-wave reflection events. Special attention was then paid to the removal of any multiple energy present in the data, and for this purpose, the approach of Verschuur (1991) was employed. We acknowledge the help of Eric Verschuur in applying this method to the data. Figure 6.3a illustrates two typical raw shot gathers (shot # 153 and 156) from the middle of the profile; Fig. 6.3b shows the result of preprocessing involving deconvolution, trace-editing and band-pass filtering; Fig. 6.3c shows the result after surface wave and multiple removal. The entire multiangle, multiscale analy-

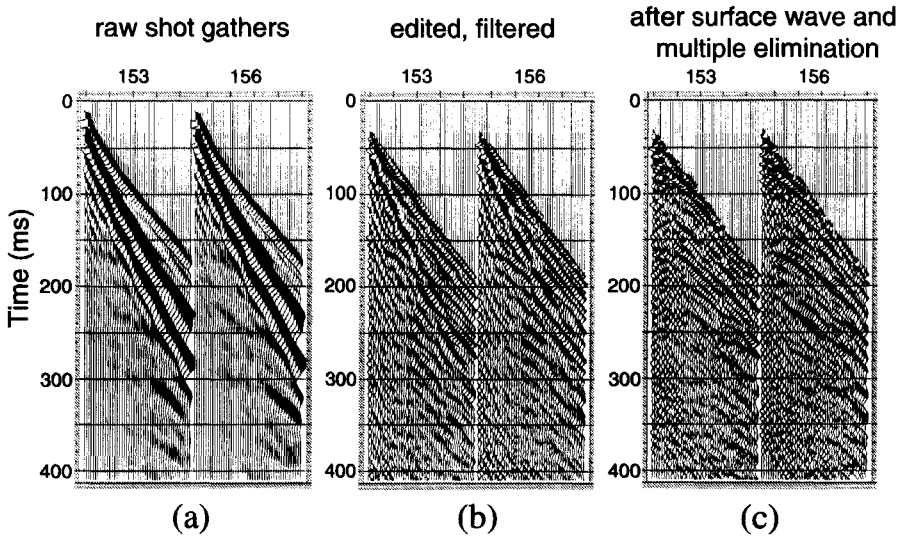

Figure 6.3: *S-wave reflections on soil. Two typical shot gathers: (a) raw data, (b) after trace editing and band-pass filtering, (c) after surface wave and multiple suppression.*

sis is next carried out on pre-stack data, but for the purpose of interpretation and for checking the lateral continuity, a stacked section was prepared. From interactive velocity analysis, a simple, 1-D RMS velocity (c_S) function, with velocity increasing with depth, was found and used to stack the data; lateral velocity variation was ignored for this purpose. Figure 6.4 shows the stacked time section containing 142 CMPs. The total lateral extent of the seismic section in Fig. 6.4 is 35.25 m. An approximate estimate of the interval velocity field was deduced from the RMS velocity function, and was used to create a tentative depth section, which is shown in Fig. 6.5. For comparison, the CPT q_c is also displayed in Fig. 6.5. The distinct S-wave reflection events at around 3-4 m and 6-12 m correspond to the Holocene sand-clay

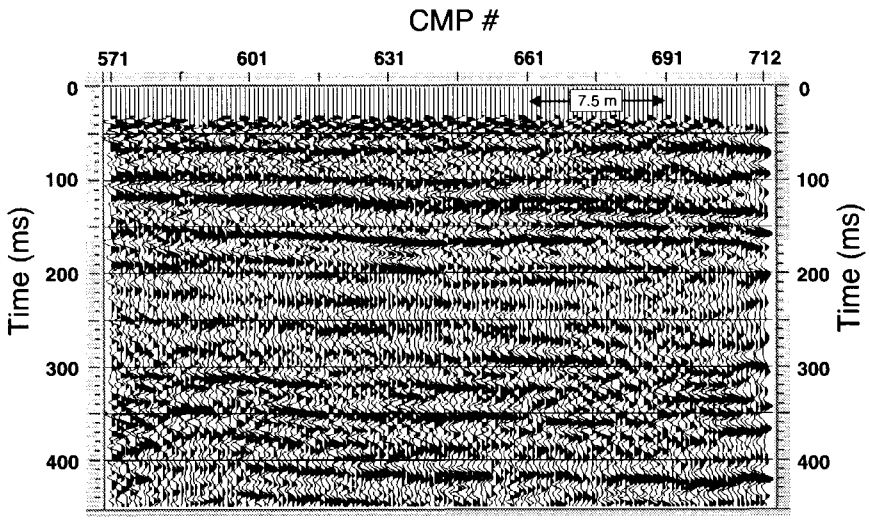

Figure 6.4: *S-wave reflection data: stacked time section.*

boundaries and match well with the sharp changes in the CPT data. In the seismic section we notice also clear events at around 23-25 m, which is the Holocene-Pleistocene boundary evident in the CPT data.

6.5.3 Multiangle, multiscale analysis of field data

To test the proposed method for multiscale correlation of seismic reflection data with CPT q_c, we first give a detailed analysis for only a small number of CMPs. Following, the full seismic reflection data set is treated, to analyze the tangibility of the characterization of the lateral change of a soil interface.

For multiangle, multiscale analysis five equally spaced (lateral separation 7.5 m) CMP gathers were chosen. The locations of these CMPs are marked by black triangles in Fig. 6.5. Linearized Zoeppritz Inversion (LZI) was car-

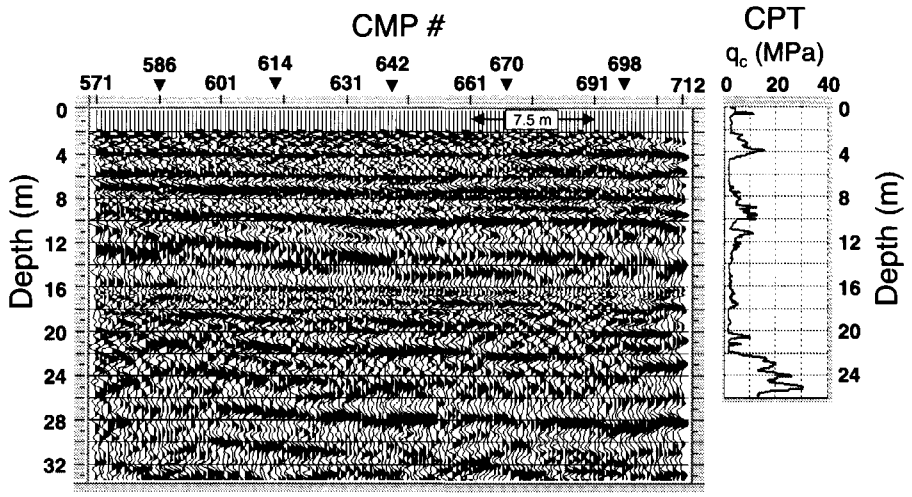

Figure 6.5: *S-wave reflection data: stacked depth section. The measured CPT cone resistance at this site (same as in Fig. 6.2) is also displayed, for comparison.*

ried out to obtain the local c_S contrast functions for these five CMPs. The result is depicted in Fig. 6.6. Due to transmission and scattering losses, the velocity contrast functions show strongly decreasing amplitudes with depth. Note that the estimates of the singularity parameter α are insensitive to the absolute strength of an event, but only to its relative strength within a small window around this event (i.e. the wavelength of the broadest analyzing wavelet in the wavelet transformation [see Appendix A]). Therefore, in multiscale analysis, no correction for these losses is applied to the velocity contrast functions. However, to highlight the deeper events, in Fig. 6.6 an exponential gain with depth has been applied to the trace plots. Note the good resolution of a number of events in the local velocity contrast functions. The contrast functions estimated by LZI (Fig. 6.6) clearly have much higher frequency content than the RMS velocity field obtained from conventional velocity analysis (Fig. 6.2a). Reliable estimation of such high-frequency, local velocity contrast information is vital to the proposed approach of integration of seismic reflection and CPT data. Some of the events in the contrast functions can be followed laterally (Fig. 6.6). The contrast functions in the first three CMP locations (CMP 586, 614 and 642) show similar nature; but the events have a slightly different appearance in the last two traces (CMP 670 and 698).

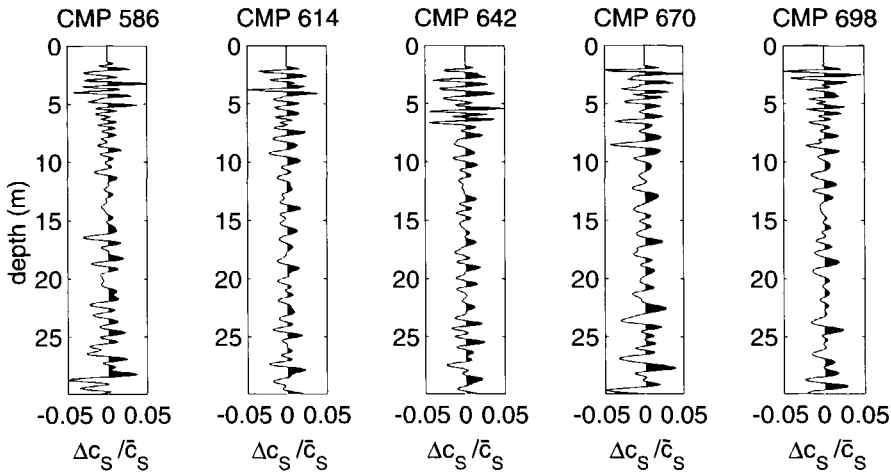

Figure 6.6: *Results of LZI: local c_S contrast functions estimated for CMPs 586, 614, 642, 670 and 698.*

In the next stage, we carry out the multiscale analysis of both CPT data and the local c_S contrast functions. The two strongest events in CPT (Fig. 6.7a) corresponding to the clay-sand interface at around 5 m depth and the Holocene-Pleistocene boundary at around 22 m depth were chosen. These events represent sharp changes in soil strength. For these two events, Fig. 6.7 illustrates the result of the multiscale analysis. We have chosen the result for CMP 642 (see also Fig. 6.6) because it is centrally located in our profile and it represents well the most prominent reflectors at this site. Figure 6.7a shows the velocity contrast function (CMP 642); Fig. 6.7b shows the wavelet transform of this function; Fig. 6.7c illustrates the modulus maxima lines, the two high-lighted events are nearly at the same depth as the prominent CPT events; Figure 6.7d shows the amplitude-versus-scale (AVS) plots for these two events, and the value of α estimated from the slope of these AVS curves. The estimated α values are -1.50 and 0.30 for the events at around 5 m and 22 m, respectively. The same analysis was carried out on CPT q_c; the results are shown in Fig. 6.7a to Fig. 6.7d. The estimated α for the corresponding two events in CPT are respectively -1.39 and 0.26, and hence are very close to those estimated from the local c_S contrast function. As the CPT was measured about 100 m away from the seismic line, these results should be interpreted with care. We can expect from local geology that the

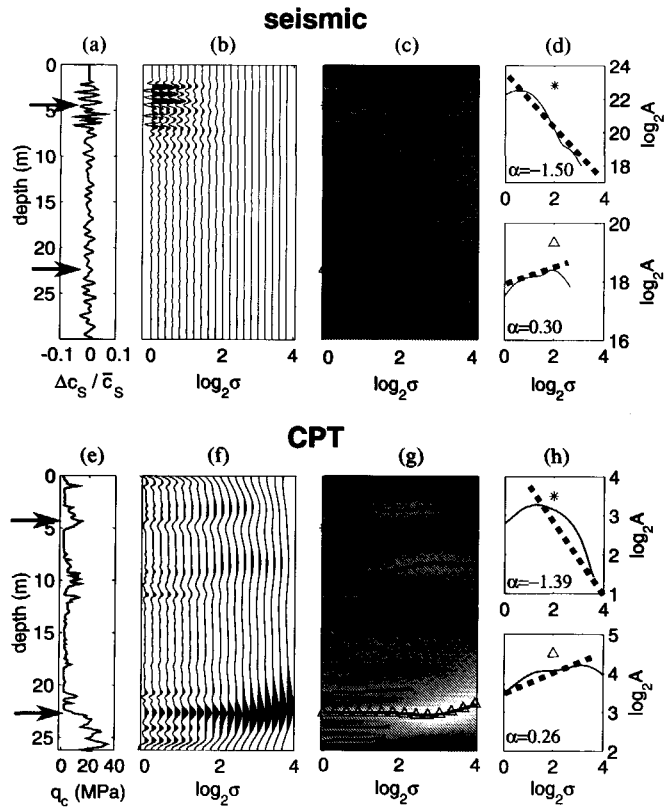

Figure 6.7: *Relating seismic to CPT based on the local scaling behavior: multiscale analysis of the velocity contrast function at CMP #642 ((a) to (d)) and for CPT q_c ((e) to (h), for two prominent subsoil interfaces (highlighted). The arrows depict the events that are analyzed. Note that the estimated α is remarkably close between seismic and CPT.*

Holocene-Pleistocene boundary is continuous for this distance. The continuity of the thin high-strength sand-layer over a large distance is improbable. The correlation that is found for the event at five meters depth shows only that thin sand-layers, which are present throughout the whole area, have similar behavior in multiscale analysis.

6.5.4 Lateral continuation of the singularity parameter along a reflector

The result presented in Fig. 6.7 is significant, as it clearly indicates that the nature of variation of the strength properties of soil over these two subsoil boundaries, as seen by CPT, is very similar to the nature of variation of the local c_S contrast, as seen by S-wave reflections. In other words, by characterizing the local scaling behavior of the c_S and q_c variation over an interface, it has been possible to find a relation between the soil strength and small-strain soil stiffness, both measured in-situ. The relatively small slope of the AVS curve at 22 m indicates that it can approximately be described as a step-like boundary (which can indeed be visually verified on the CPT data), and this is observed almost identically by both seismic and CPT. The high negative value of α (-1.50 and -1.39 for seismic and CPT, respectively) for the interface at around 5 m suggests the presence of a thin high-c_S or thin high-q_c layer at this interface, and this is also similarly observed by the local c_S contrast and CPT data. This illustrates that the α-parameter does have the potential to serve as a reliable indicator of the nature of the change over an interface of the soil-physical properties, and that the approach of multiscale analysis serves as a promising tool to delineate this fine-scale interfacial nature. The detected good correlation between the fine-scale nature of variation of c_S and CPT q_c over an interface can be justified by the fact that both our measurements (local c_S and CPT c_S) are in-situ ones, and as said earlier, they both are primarily determined by the in-situ void ratio and the horizontal stress in soil.

To check if the α-estimates are robust enough, we have carried out automatic multiscale analysis for all the five CMPs shown in Fig. 6.6, for which we derive, at first, the local c_S contrast functions through LZI. At each of these five CMP locations, all strong events which can be followed over a wide scale range (with $\log_2\sigma_{\min} > 1.8$) were chosen and α was estimated automatically. The result is shown in Fig. 6.8. The derived α values as a function of depth at these five CMPs are shown; the α values for the CPT events are also calculated and presented there, for comparison. In Fig. 6.8, the two gray lines

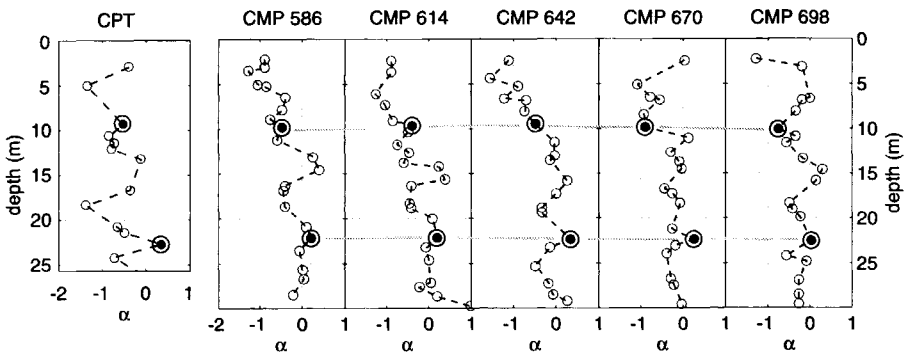

Figure 6.8: *α-profiles for CPT q_c and for local c_S contrast functions for the CMPs shown in Fig. 6.6. The two highlighted events correspond to two important subsoil interfaces (see in Figure 6 the strong events both in CPT and seismic at around 10 and 22 m) at this site. The estimated α values for these two events show good lateral consistency in the seismic data, and closeness with the α values in CPT q_c.*

connecting the events at round 10 and 22 m depths, respectively, correspond to the two strong, laterally continuous, seismic reflection events as seen in the stacked section (Fig. 6.5); the bottom one also corresponds to the one shown in Fig. 6.7. It is evident that the α-estimates are consistently very close to each other for the first three CMPs (CMP# 586, 614, 642) and then the α-value slightly changes. Further, when we compare with the CPT, we see that for the main events the α-estimates are fairly close to those of the first three CMPs, giving an indication for similar geology for both locations. This clearly shows the possibility of using the singularity parameter α as a means to integrate seismic reflection and CPT data.

6.5.5 Application to field data: mapping lateral variability along a reflector

To further check the possibility of using the singularity parameter α for mapping the lateral change of a reflector, the local c_S contrast functions for each CMP location were computed. Figure 6.9 shows the resulting, local c_S contrast field. At first sight it is clear that the resolution in the derived velocity contrast field is quite high, much higher than the resolution in the RMS velocity (Fig. 6.2). Although the inversion is carried out for each CMP independently, we notice good lateral continuity of the contrast magnitude for many

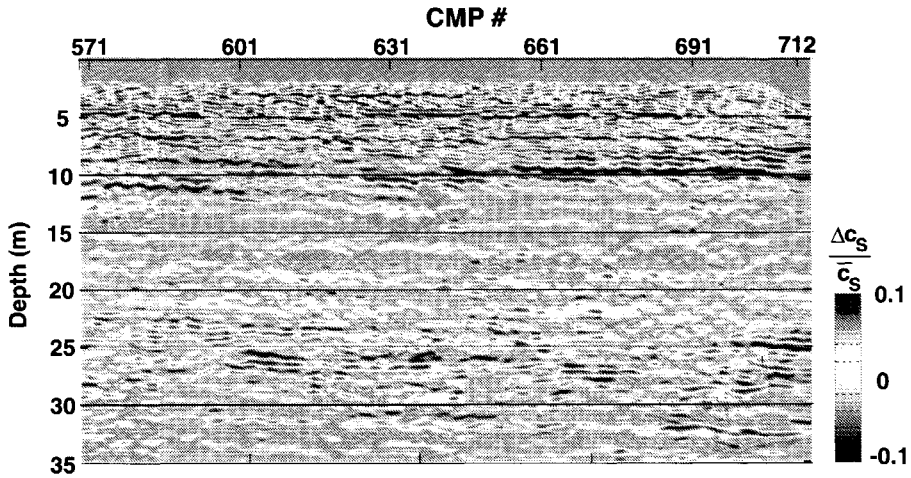

Figure 6.9: *c_S contrast field constructed by Linearized Zoeppritz Inversion, for experiment 1.*

distinct reflections. Multiscale analysis was then performed to the entire c_S contrast field and also to the CPT q_c. The result is illustrated in Fig. 6.10. Only events, that are visible over a wide scale range in the wavelet transform have been used. Next, all events in the velocity contrast field which exhibit a given α value (the chosen small range is shown on the left side) are plotted (small white dashes) in Figures 6.10b and 6.10c. An estimate of the singularity parameter α around 0 (Fig. 6.10b) indicates a step-like change at the interface, whereas an estimate of α of about -0.5 (Fig. 6.10c) indicates the presence of a thin high-velocity layer at the interface. The result of applying the multiscale analysis to CPT q_c is shown on the right-hand side of Figures 6.10b,c. At first sight, Figures 6.10b,c may appear like scatter-plots: a result of inevitable noise in real, field data. However, a careful look reveals a very interesting feature. In Fig. 6.10b between CMP 592 and 634, there is a clear lateral alignment of events around 10 m depth (which corresponds to a prominent reflection event from the sand-clay layer boundary as seen in Fig. 6.10a), but this continuity stops at around CMP 634. However when we change the α from around 0.0 to around -0.5 (Fig. 6.10c), we see a clear lateral alignment again around 10 m depth between CMP 640 and CMP 702. In Fig. 6.10a the reflection at around 10 m appears as a continuous event, however its scaling properties remain unknown. On the other

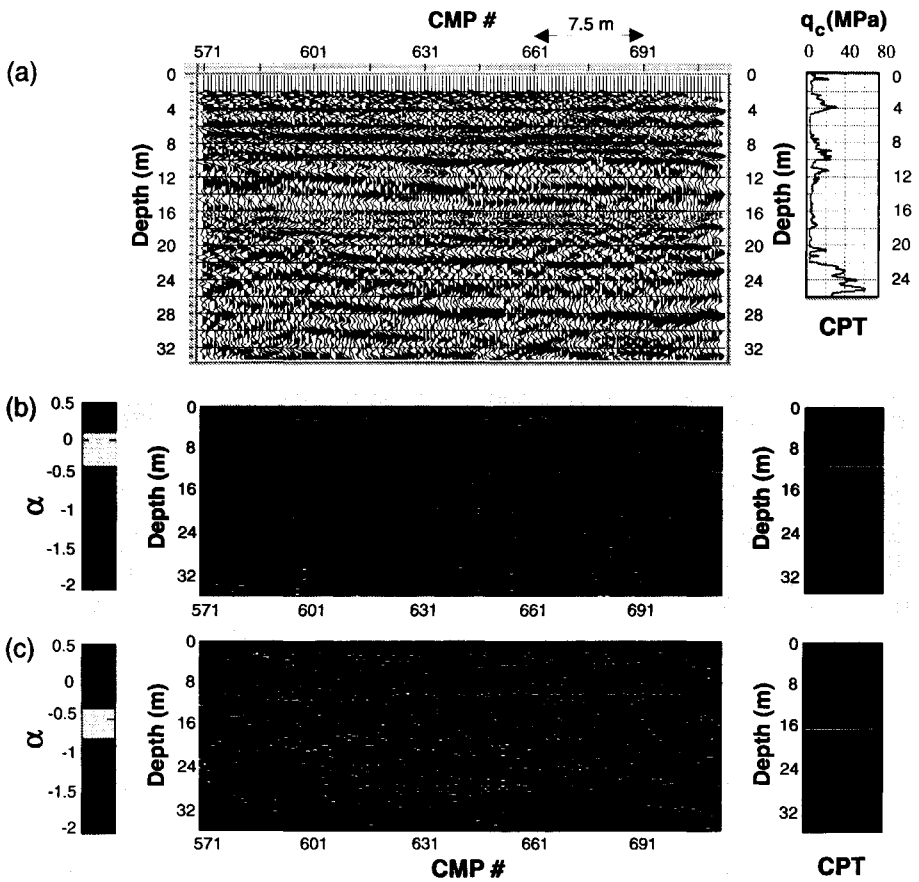

Figure 6.10: *Experiment 1: Multiscale analysis revealing subtle lateral variation of a subsoil interface, that can be related to CPT data: (a) stacked depth section of the seismic data (left) and CPT q_c (right), (b) position of points with singularity parameter α around 0, (c) position of points with singularity parameter α around -0.5.*

hand, the multiscale analysis reveals that the nature of this transition is not laterally constant. While it seems to behave as a step-like change in c_S between CMP 592 and CMP 634, the transition behaves more like a thin high velocity layer at the interface between CMP 640 and CMP 702. We mark that there is indeed a slight change in apparent dip of this reflector occurring at around CMP 639 (Fig. 6.10a).

The multiscale analysis has succeeded to detect the lateral variation of the nature of the interface at around 10 m depth. We have checked this result in relation to the CPT data at this site. Note that the CPT was located closer to the left part of the seismic line. However, due to the relatively large distance between the CPT location and the seismic line, we should be careful in the interpretation of the results above. The right panels in Figures 6.10b,c plot the CPT events that exhibit a certain value for the singularity parameter α. We see a clear CPT event at around 10 m depth with α around 0 (the upper one), that matches in depth with the alignment that we notice between CMP 592 and CMP 634 in the α estimates of the seismic data (Fig. 6.10b). However, for α around -0.5, we find no relation for this event between CPT and seismic. This indicates that, for this interface at around 10 m depth, the details of the CPT data are similar to those of the fine-scale c_S information present in the left-half of the seismic reflection data, but for the right-half of the seismic profile (CMP 640-702), the nature of the boundary appears to be different. In absence of any CPT in this part, the multiscale analysis has revealed this variation. Such variations are important information for geotechnical evaluations.

6.5.6 Experiment 2

The second, extensive field experiment was carried out at a site where multiple CPTs were measured right on the seismic line, and hence any subtle variation at an interface can be directly compared between seismic and CPT data. Table 6.2 shows the acquisition parameters for the second experiment. The seismic source was a small, electromagnetic, horizontal vibrator source, developed by OYO CAG for the controlled generation of high-frequency S-waves, for shallow engineering applications [Ghose et al. (1996)]. As is typical to the western Netherlands, the geology at this site is composed of alternating sand and clay layers. At the shallowest part, there are peat layers, which act as important cap soil from environmental consideration. The Holocene-Pleistocene boundary is situated at around 21-22 m depth. Figure 6.11 shows a detailed soil profile at this site, exactly below our seismic

Shallow shear-wave seismic reflection	
S-wave source:	horizontal vibrator (OYO CAG) sweep: 30-500 Hz sweep length: 7500 ms record length: 8190 ms
Receivers:	28 Hz crossline horiz. geophones, 48 ch.
Vertical stack:	4
Shot interval:	2.0 m
Receiver interval:	0.5 m
Min. S-R distance:	2.0 m
Data sampling:	0.25 ms
Total profile length:	$\sim$ 330 m
Cone Penetration Test: many measurements	
Depth:	30-35 m
Location:	measurements right on the seismic line

Table 6.2: *Acquisition parameters of experiment 2*

line. This profile is derived from multiple CPTs (see CPT q_c Fig. 6.11), supplemented by data of testing of soil samples in a few boreholes.

Figure 6.12 shows three typical seismic reflection shot gathers at this site. The data appear quite different from those of experiment 1. Because the horizontal vibrator was used as the seismic source, generated surface waves were much less (as the sweep started at 30 Hz). Most importantly, the frequency content is clearly much higher (Fig. 6.13) for the vibrator data (experiment 2) compared to the sledgehammer data (experiment 1). Distinct S-wave reflection events can already be identified in the raw shot gathers for two-way-times exceeding 500 ms.

Amplitude-preserved processing was carried out very carefully. Suppression of surface waves and multiple energy from the shot gathers turned out to be the biggest challenge. Surface wave energy was eliminated using the same approach as in Experiment 1. Again, multiple energy was suppressed using the algorithm of Verschuur (1991). Many clear primary reflection events can be seen in the preprocessed shot gathers. Because of the use of the higher frequency content of the vibrator data a wider range of scale could be addressed in the multiscale analysis. The use of a wider scale range does increase the quality of the inversion for the singularity parameter α.

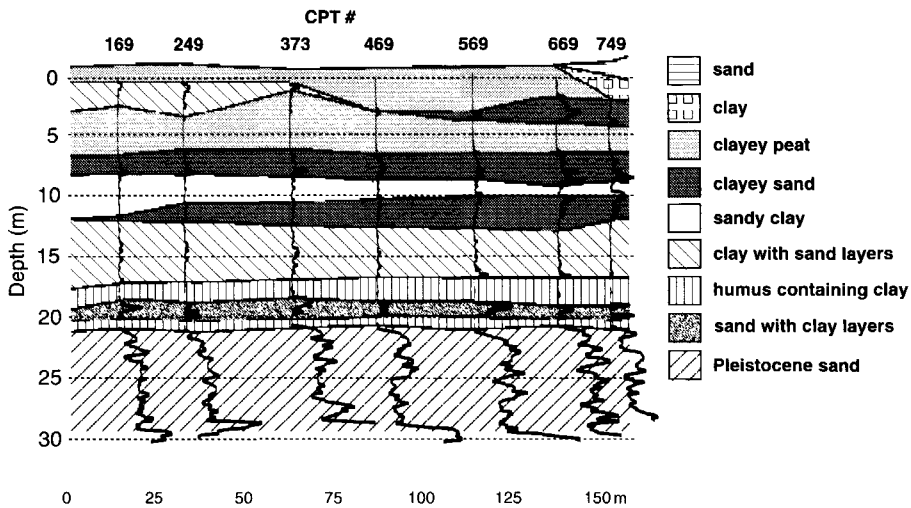

Figure 6.11: *Soil profiles derived from CPT data and continuous soil sampling in a number of boreholes. CPT q_c data (in overlay) defined the layer boundaries, while soil sampling results determined the composition/type of the soil. Note distinct lateral variations in the fine-scale CPT data along the boundary of two layers. The location of this profile corresponds exactly to the location of our seismic line for experiment 2.*

Figure 6.14a shows the stacked time section. The strong reflection at around 330-350 ms is interpreted as the Holocene-Pleistocene boundary, as the depths of these events obtained using realistic velocity models are close to the known depth of this Holocene-Pleistocene boundary. Many shallower reflections, between 75 ms and 200 ms are from various shallow sand-clay and peat-clay interfaces as seen in the soil profile (Fig. 6.11).

Figure 6.14b shows the result of applying LZI to all the CMPs shown in Fig. 6.14a. The local c_S contrast field shows quite high resolution and remarkable lateral continuity along prominent reflectors. This confirms the stability of LZI.

Figure 6.15a shows the depth section obtained using a simple 1-D velocity structure derived from the smoothed RMS velocity field. In Fig. 6.15b, cone resistance (q_c) data from 7 CPTs located right on the seismic line are shown. CPT locations are shown by black triangles on the top. It is clear that the S-wave reflections follow remarkably well strong q_c interfaces. However, the fine-scale nature of the interface, that varies laterally and can be seen clearly in the CPT data, cannot be discriminated in the stacked seismic data. We have

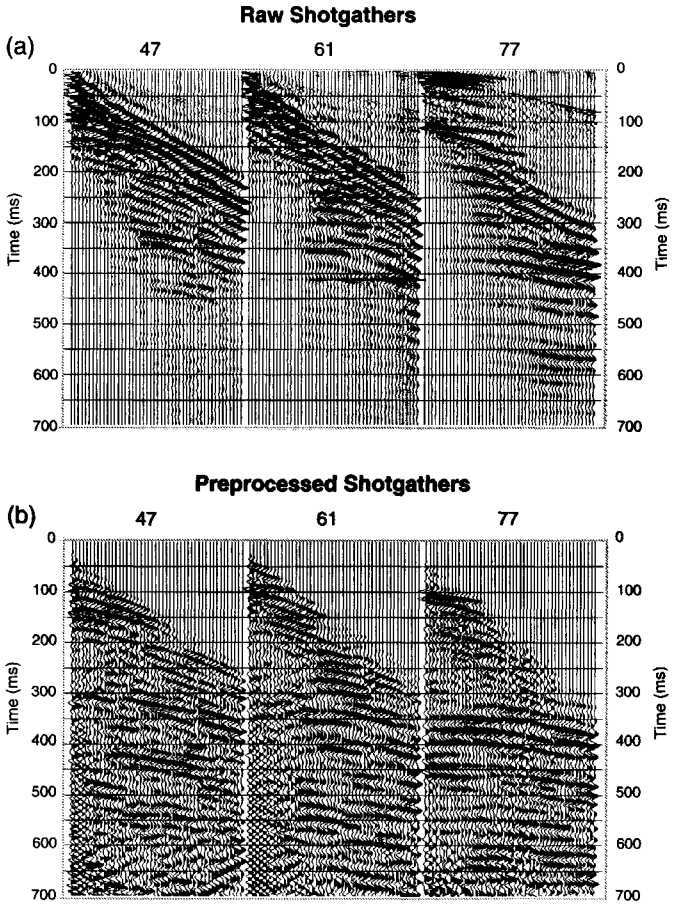

Figure 6.12: *Experiment 2: typical shot gathers, (a) raw field data, (b) data after preprocessing, including surface wave and multiple elimination. Note in the raw data that the surface waves are spatially varying.*

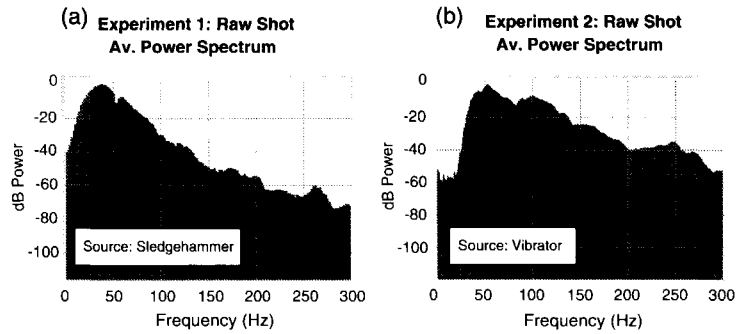

Figure 6.13: *Average amplitude spectrum of raw shot gathers: (a) experiment 1: sledgehammer source (shot# 153), (b) experiment 2: horizontal vibrator source (shot# 47). The vibrator data clearly have more high frequencies. The peak spectral amplitude in the raw data corresponds to surface waves. In case of the vibrator, surface waves were relatively suppressed by starting the sweep at 30 Hz (see shot gathers); such control is not possible for the sledgehammer.*

chosen 2 prominent boundaries in the CPT data: one at around 7.5-9.0 m depth corresponding to a sand-clay boundary, and another at around 22 m depth corresponding to the Holocene-Pleistocene boundary. Then we have interpreted the corresponding events in the stacked seismic data. In absence of a VSP here, the depth of the shallow event shows some discrepancy with the depth of the CPT event. We attribute this to the frozen condition of the top soil during the second half of the field data acquisition, which made it difficult to assign a reasonable velocity for time-to-depth conversion in the shallow part.

The two chosen events are marked in Figures 6.15a and 6.15b. For these two strong, laterally continuous events we perform the multiscale analysis to verify if the fine-scale, lateral variation in CPT data along a boundary can be extracted from the local c_S contrast field.

Figure 6.16a shows the chosen shallow event in the CPT data. Figure 6.16b shows the α values derived from the c_S contrast field and from the CPTs. We find that the estimates of the singularity parameter α for seismic and CPT are remarkably close. This result illustrates that it is possible to extract the lateral variation information of the CPT data from local c_S information implicit in the S-wave reflection data.

Figure 6.17b illustrates the result of applying the multiscale analysis to

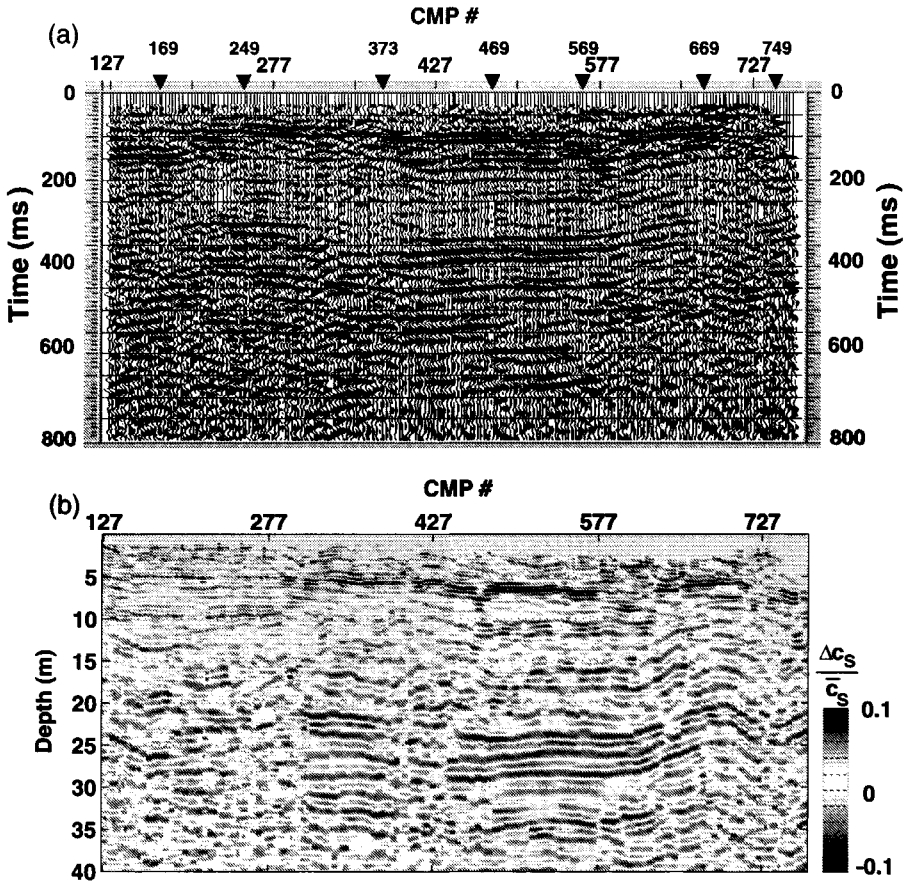

Figure 6.14: *(a) Time section of Experiment 2. (b) c_S contrast field constructed by Linearized Zoeppritz Inversion.*

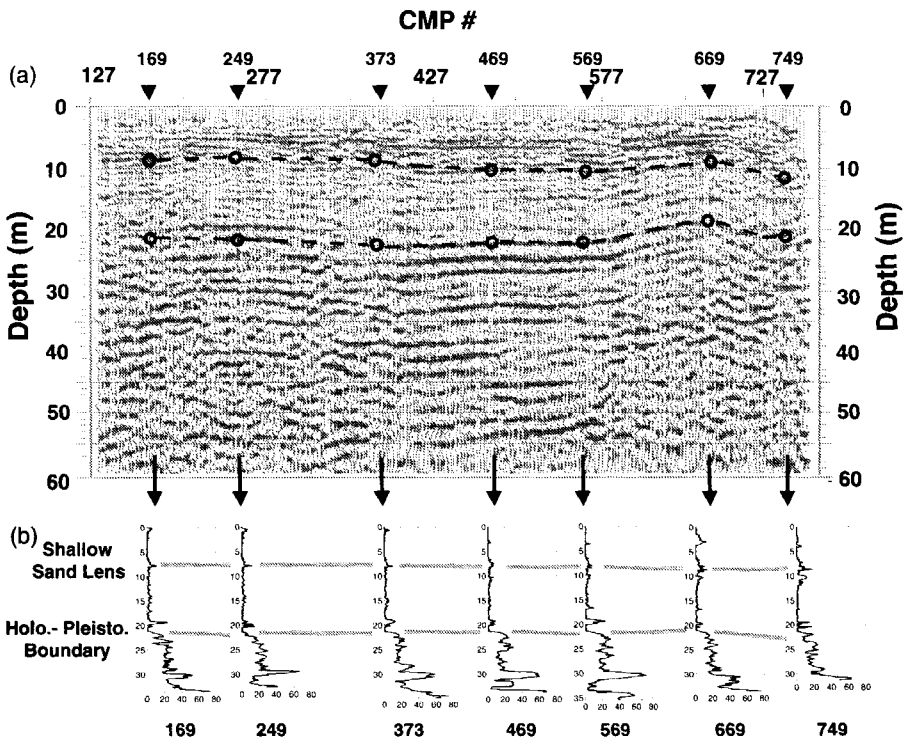

Figure 6.15: *Experiment 2: (a) depth section, (b) CPT data at 7 locations right on the seismic line. Two strong events identified both on CPT (denoted by the gray lines) and seismic data (denoted by the black lines) are the ones for which the multiscale analysis was performed, to check the relation between CPT and seismic.*

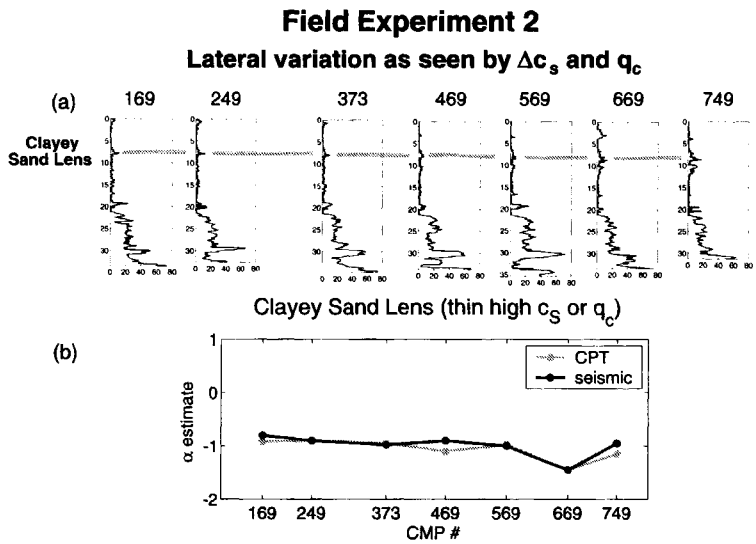

Figure 6.16: *Comparison of α values between CPT and S-wave seismic data, for the clayey sand lens at 7.5-9.0 m depth: (a) the chosen shallow event in the CPT data, (b) estimated α for CPT (gray) and seismic (black).*

CPT and seismic data for the chosen deep event - the prominent Holocene-Pleistocene boundary (Fig. 6.17a). Again we find a remarkable similarity of the α-estimates between CPT and seismic.

These results are striking, because they clearly demonstrate that S-wave reflection data contain information on the local scaling behavior of the soil strength that can be quantitatively correlated with the local scaling behavior of CPT.

6.6 Discussion

The approach of multiscale analysis of true-amplitude, prestack seismic reflection data, that we have applied to a laterally continuous S-wave reflector, proves to be capable of extracting and quantifying the local scaling behavior over an interface. The lateral variation information thus extracted from the S-wave seismic data correlates very well with the lateral variation of soil strength as monitored by CPTs. Our results suggest that with this approach it is possible to extract the continuous information of lateral variation of soil

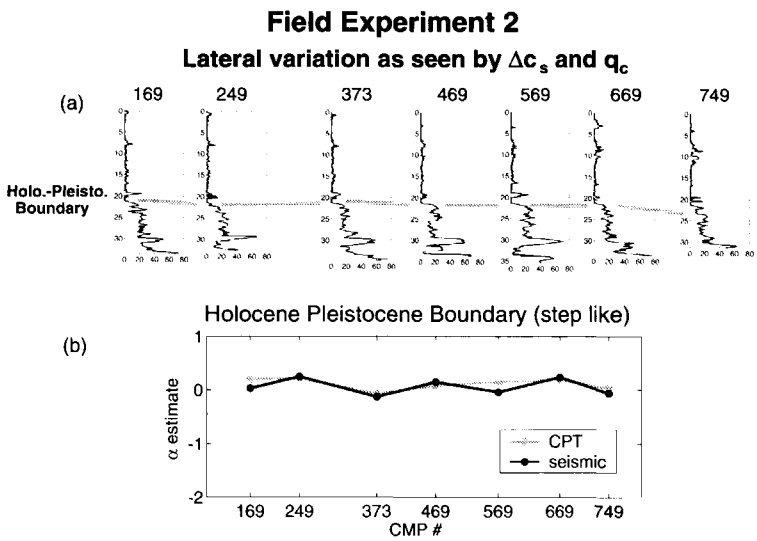

Figure 6.17: *Comparison of α values between CPT and S-wave seismic data, for the Holocene-Pleistocene boundary at about 21-22 m depth: (a) the chosen deep event in the CPT data, (b) estimated α for CPT (gray) and seismic (black).*

strength, without digging holes or trenches. This is of great practical value, as it is often not feasible to excavate the soil, particularly in urban environments.

The success of this approach relies on the ability of LZI to reliably estimate the local, fine-scale velocity contrast information at a subsoil interface. Unless such local velocity information is accurately and stably derived from the seismic reflection data, the correlation with CPT (which is a local, in-situ measurement) can not be justified.

The performance of this approach diminishes if the data contain unreasonably high noise levels; careful preprocessing preserving correct amplitude information of all primary reflections is, thus, an important requisite. Further, lateral consistency in the quality of noise elimination is important in order to obtain meaningful lateral variation information. This is due to the fact that various kinds of noise, particularly the source coherent noise, like surface waves and multiples, often show large lateral variation.

The multiscale analysis has shown its strength to characterize the fine-scale lateral variation along a subsoil layer boundary. The singularity parameter α can indeed be a meaningful indicator of the nature of an interface.

Having a wider range of frequency and hence a wider range of scale available in the reflection data enables one to estimate α more reliably. Use of high-frequency vibratory sources, and careful data processing causing no reduction of the maximum available frequency bandwidth, are very important to obtain accurate α estimates.

6.7 Conclusions

For integrating shallow, S-wave reflection data to CPT, we have presented a new concept, based on the characterization of the local scaling behavior of both data types. The fine-scale, local c_S contrast information present in the seismic reflection data can be reliably extracted by the Linearized Zoeppritz Inversion of the preprocessed, true-amplitude, pre-stack S-S reflection data. Based on the assumption that the extracted c_S contrast function and the CPT q_c obey locally a similar scaling behavior, we have characterized the nature of fine-scale variation over an interface in terms of the singularity parameter α, which is obtained by multiscale analysis.

Though CPT and seismic represent the soil properties at very different levels of strain, our results clearly show a close similarity between their nature of variation over a subsoil interface, in terms of the local singularity parameter. This may serve as a method to relate the lateral variation of the local c_S information to that of the strength properties of the soil, as estimated in-situ by CPT.

From testing this approach on two extensive field data sets containing both S-wave seismic reflection and CPT data, some significant results could be obtained. LZI can provide stable and reliable estimates of the local c_S contrast functions. Most importantly, the lateral variation of the nature of the c_S distribution over an interface was found to correlate remarkably well with the lateral variation of the CPT q_c at the same point of the interface. To analyze the lateral variation objectively, multiscale analysis has proven to be a reliable tool. Our finding on field data shows the possibility of this approach to find lateral variations in soil strength over an interface without boring holes.

Appendix A

The wavelength of the analyzing wavelet

In this appendix, the link between the scale parameter σ in the continuous wavelet transformation and the effective wavelength $\lambda_{\vartheta}^{\text{eff}}$ of the analyzing wavelet is derived. The continuous wavelet transform of a function $f(z)$ as used in multiscale analysis is given by

$$\{\mathcal{W}_{\vartheta} f\}(\sigma, z) = \check{f}(\sigma, z) = \frac{1}{\sigma^{\mu}} \int_{-\infty}^{\infty} f(z')\vartheta(\frac{z'-z}{\sigma})dz', \tag{A.1}$$

in which $\mu = 1$ for reasons given in section 2.6.
We have chosen as the analyzing wavelet $\vartheta(z)$, the n-th order derivative of a Gaussian, which is given in the wave-number domain by

$$\Theta(k) = (jk)^n \Gamma(k) = (jk)^n e^{-k^2}, \tag{A.2}$$

which transforms to the depth-domain as

$$\vartheta(z) = \frac{1}{2\sqrt{\pi}} \frac{d^n}{dz^n} e^{-(\frac{z}{2})^2}. \tag{A.3}$$

When we change variables $z \rightarrow \frac{z}{\sigma \Delta z}$, in which Δz is the sampling interval of the log and σ the scale of the analyzing wavelet, we find a generic expression of the analyzing wavelet, given by $\vartheta(\frac{z}{\sigma \Delta z})$ in the depth domain

$$\vartheta(\frac{z}{\sigma \Delta z}) = \frac{(\sigma \Delta z)^n}{2\sqrt{\pi}} \frac{d^n}{dz^n} e^{-(\frac{z}{2\sigma \Delta z})^2}, \tag{A.4}$$

or equivalently for $\Theta(\sigma k \Delta z)$ in the wave-number domain

$$\Theta(\sigma k \Delta z) = \sigma \Delta z (jk\sigma \Delta z)^n e^{-(\sigma k \Delta z)^2}. \tag{A.5}$$

We now identify the effective wavelength of the analyzing wavelet by the wave-number k_ϑ^{eff}, the k-value for which $\Theta(\sigma k \Delta z)$ is maximum. We can easily verify that this wave-number k_ϑ^{eff} for the n-th order derivative is located at

$$k_\vartheta^{\text{eff}} = \frac{1}{\sigma \Delta z} \sqrt{\frac{n}{2}}. \tag{A.6}$$

This wave-number is connected to the effective wavelength of the analyzing wavelet in a straightforward way according to

$$\lambda_\vartheta^{\text{eff}} = \frac{2\pi}{k_\vartheta^{\text{eff}}} = 2\pi\sigma\Delta z \sqrt{\frac{2}{n}}, \tag{A.7}$$

which shows that the higher order the derivative of the analyzing wavelet, the smaller the effective wavelength.

Bibliography

Aki, K. and Richards, P. G. (1980). *Quantitative seismology, Vol. I.* W.H. Freeman and Company, San Fransisco.

Aussem, A., Campbell, J. and Murtagh, F. (1998). Wavelet-based feature extraction and decomposition strategies for financial forecasting. *Journal of Computational Intelligence in Finance*, 6 (2), pp. 5–12.

Baldi, G., Bellotti, R., Ghionna, V., Jamiolkowski, M. and Pasqualini, E. (1986). Interpretation of CPTs and CPTUs Part 2: drained penetration of sands. *Proc. of the Fourth Int. Geotech. Sem. Field instumentations and in situ measurements, Singapore*, pp. 143–156.

Barends, F. B. J., Jonker, A., van Niekerk, A. J., Pachen, H. M. A., Post, M. L., Termaat, R. J. and Welling, R. J. (1999). Geotechnics in The Netherlands. *Geotechniek, Special Issue*, Hannink, G., ed., pp. 11–23.

Been, K. and Jefferies, M. G. (1985). A state parameter for sands. *Géotechnique*, 35 (2), pp. 99–112.

Bracewell, R. N. (2000). *The Fourier transform and its applications*. McGraw-Hill International Editions, 3rd edition.

Brouwer, J., Ghose, R., Helbig, K. and Nijhof, V. (1997). The improvement of geotechnical subsurface models through the application of S-wave reflection seismic exploration. *Proc. of the EEGS-ES Mtg., Aarhus*.

Butkov, E. (1968). *Mathematical Physics*. Addison-Wesley.

Canny, J. (1986). A computational approach to edge detection. *IEEE Trans. Pattern Anal. Machine Intell.*, 36, pp. 961–1005.

Clayton, R. W. and McMechan, G. A. (1981). Inversion of refraction data by wave field continuation. *Geophysics*, 6, pp. 860–868.

Cohen, L. (1995). *Time-frequency analysis*. Prentice-Hall, Englewood Cliffs.

Collins, I. F. (1990). On the mechanics of state parameter models for sands. *Proc. of the 7^{th} Int. Conf. Comp. Methods and Adv. Geomech.*, volume 1, pp. 593–598.

Cunning, J. C., Robertson, P. K. and Sego, D. C. (1995). Shear wave velocity to evaluate in situ state of cohesionless soils. *Can. Geotech. J.*, 32, pp. 848–858.

Daubechies, I. (1992). *Ten lectures on wavelets*. SIAM, Philadelphia.

De Haas, J. C. (1992). *Elastic stratigraphic inversion, an integrated approach*. Ph.D. thesis, Delft University of Technology.

Dessing, F. J. (1997). *A wavelet transform approach to seismic processing*. Ph.D. thesis, Delft University of Technology.

Dillen, M. W. P. (2000). *Time-lapse seismic monitoring of subsurface stress dynamics*. Ph.D. thesis, Delft University of Technology.

Dobrin, M. B. and Savit, C. H. (1988). *Introduction to geophysical prospecting*. McGraw-Hill International Series, 4th edition.

Donoho, D. L. and Johnstone, I. M. (1994). Ideal spatial adaptation by wavelet shrinkage. *Biometrika*, 81, pp. 425–455.

Eshelby, J. D. (1957). The determination of the elastic field of an ellipsoidal inclusion and related problems. *Proc. R. Soc. London*, A (221), pp. 376–396.

Eslaamizaad, S. and Robertson, P. K. (1998). Cone penetration resistance of sand from seismic tests. *Geotechnical site characterization*, Robertson and Mayne, eds., pp. 1027–1032. Balkema.

Fear, C. E. and Robertson, P. K. (1995). Estimating the undrained strength of sand: a theoretical development. *Can. Geotech. J.*, 32, pp. 859–870.

Fokkema, J. T. and Van den Berg, P. M. (1993). *Seismic applications of acoustic reciprocity*. Elsevier, Amsterdam.

Friedberg, S. H., Insel, A. J. and Spence, L. E. (1989). *Linear Algebra*. Prentice-Hall International Series, 2nd edition.

Gabor, D. (1946). Theory of communication. *J. Inst. Elect. Eng. (London)*, 93, pp. 429–457.

Ghez, J. M. and Vaienti, S. (1989). On the wavelet analysis for multifractal sets. *J. Stat. Physics.*, 57, pp. 415–420.

Ghose, R., Brouwer, J. and Nijhof, V. (1996). A portable S-wave vibrator for high-resolution imaging of the shallow subsurface. *Proc. of the* 58^{th} *EAGE Ann. Mtg., Amsterdam*, p. M037.

Ghose, R. and Drijkoningen, G. G. (2000). Towards a constrained integration of seismic to CPT parameters in sand. *Proc.* 62^{nd} *EAGE Ann. Mtg., Glasgow.*

Ghose, R., Nijhof, V. and Brouwer, J. (1998). Shallow, high-resolution, shear-wave reflection imaging: extended potential in geotechnical surveys. *Proc. of the EEGS-ES Mtg., Barcelona.*

Goudswaard, J. C. M., Ten Kroode, A. P. E., Snieder, R. K. and Verdel, A. R. (1998). Detection of lateral velocity contrasts by crosswell traveltime tomography. *Geophysics*, 63 (2), pp. 523–533.

Goupillaud, P., Grossmann, A. and Morlet, J. (1984). Cycle-octave and related transforms in seismic signal analysis. *Geoexploration*, 23, pp. 85–102.

Goutbeek, F. and Muijs, R. (1999). The investigation of correlations between CDP- VSP- and CPT-datasets. Tech. report, Utrecht University.

Grossmann, A. and Morlet, J. (1984). Decomposition of Hardy functions into square integrable wavelets of constant shape. *SIAM J. Math.*, 15, pp. 723–736.

Hardage, B. A. (1983). *Vertical seismic profiling*. Geophysical Press.

Hatton, L., Worthington, M. H. and Makin, J. (1986). *Seismic Data processing Theory and Practice*. Blackwell Scientific Publications.

Herrmann, F. J. (1997). *A scaling medium representation*. Ph.D. thesis, Delft University of Technology.

Hoekstra, E. V. (1996). *Multiscale analysis of seismic data by the wavelet transform*. MSc thesis. Master's thesis, Delft University of Technology.

Houlsby, G. T. and Hitchman, R. (1988). Calibration chamber test of a cone penetrometer in sand. *Géotechnique*, 38 (1), pp. 39–44.

Imai, T. and Tonouchi, K. (1982). Correlation of N-value with S-wave velocity. *Proc. of the 2nd Europ. Symp. on Penetration Testing*, pp. 67–72.

Jefferies, M. G. (1993). Nor-sand: a simple critical state parameter for sand. *Geotechnique*, 43 (1), pp. 91–103.

Kennett, B. L. N. (1983). *Seismic wave propagation in stratified media*. Cambridge University Press.

Knott, C. G. (1899). Reflection and refraction of elastic waves with seismological applications. *Phylosophical Magazine*, 5 (48), pp. 64–97.

Kumar, P. and Foufoula-Georgiou, E. (1994). Wavelets in geophysics: an introduction. *Wavelets in Geophysics*, Kumar, P. and Foufoula-Georgiou, E., eds., pp. 1–43. Academic Press, Inc.

Lunne, T., Robertson, P. K. and Powell, J. J. M. (1997). *Cone penetration testing in geotechnical practice*. Blackie Academic & Professional, London.

Mallat, S. and Zhang, Z. (1993). Matching pursuit with time frequency dictionaries. *IEEE Trans. Signal Process.*, 41 (12).

Mallat, S. G. and Hwang, W. L. (1992). Singularity detection and processing with wavelets. *IEEE Trans. Inform. Theory*, 38 (2), pp. 617–643.

Mandelbrot, B. B. (1974). Intermittent turbulence in self-similar cascades: divergence of high moments and dimension of the carrier. *J. Fluid. Mech.*, 62 (2), pp. 331–358.

McCowen, D. W. and Brysk, H. (1989). Cartesian and cylindrical slant stacks. *Tau-p, a plane wave approach to the analysis of seismic data*, P. L. Stoffa, ed., pp. 1–33. Kluwer Academic Publishers.

Meigh, A. C. (1987). *Cone penetration testing: methods and interpretation*. Butterworths.

Menke, W. (1984). *Geophysical data analysis: Discrete inverse theory*. Academic Press Inc.

Mindlin, R. D. (1949). Compliance of elastic bodies in contact. *J. Appl. Mech.*, 19, pp. 259–268.

Morlet, J., Arens, G., Fourgeau, E. and Giard, D. (1982). Wave propagation and sampling theory. *Geophysics*, 47, pp. 203–236.

Muir Wood, D. (1990). *Soil behavior and critical state soil mechanics.* Cambridge University Press.

Peacock, K. L. and Treitel, S. (1969). Predictive deconvolution: theory and practice. *Geophysics*, 34 (2).

Rampello, S. and Callisto, L. (1998). A study on the subsoil of the Tower of Pisa based on results from standard and high-quality samples. *Can. Geotech. J.*, 35, pp. 1074–1092.

Reuss, A. (1929). Die berechnung der Fliessgrenze von Mischkristallen auf Grund der Plastizitätsbedingungen für Einkristalle. *Z. Angew. Math. Mech.*, 9, pp. 49–58.

Robertson, P. K., Sasitharan, S., Cunning, J. C. and Sego, D. C. (1995). Shear wave velocity to evaluate in situ state parameter of Ottawa sand. *J. Geotech. Eng.*, 121 (3), pp. 249–261.

Roscoe, K. H. and Burland, J. B. (1968). On generalised stress strain behaviour of wet clay. *Engineering Plasticity*, Heyman and Leckie, eds., pp. 535–609. Cambridge University Press.

Rüger, A. (1996). *Reflection coefficients and azimuthal AVO analysis in anisotropic media.* Ph.D. thesis, Colorado School of Mines.

Salgado, R., Mitchell, J. K. and Jamiolkowski, M. (1997). Cavity expansion and penetration resistance in sand. *J. Geotech. and Geoenv. Eng.*, 123 (4), pp. 344–354.

Sasitharan, S. (1994). *Collapse behaviour of very loose sand.* Ph.D. thesis, University of Alberta, Edmonton, Alberta.

Schiphouwer, R. A., Van Kessel, A. J., Netzel, H., Kaalberg, F. J. and Theunissen, E. A. H. (1999). GIS-data base for urban infrastructural projects. *Geotechniek, Special Issue*, Hannink, G., ed., pp. 72–73.

Schofield, A. N. and Wroth, C. P. (1968). *Critical state soil mechanics.* McGraw-Hill, England.

Schön, J. H. (1996). *Physical properties of rocks, fundamentals and principles of petrophysics.* Elsevier.

Schultz, P. S. and Claerbout, J. F. (1978). Velocity estimation and downward continuation by wavefield synthesis. *Geophysics*, 43, pp. 691–714.

SETI (2000). The search for extra-terrestrial intelligence. `http://www.setiathome.ssl.berkeley.edu`.

Sheriff, R. E. (1984). *Encyclopedic Dictionary of Exploration Geophysics*. Society of Exploration Geophysics.

Simonini, P. and Cola, S. (2000). Use of piezocone to predict maximum stiffness of Venetian soils. *J. of Geotech. and Geoenv. Eng.*, 126, pp. 378–382.

Sladen, J. A., D'Hollander, R. D. and Krahn, J. (1985). The liquefaction of sands, a collapse surface approach. *Can. Geotech. J.*, 22, pp. 564–578.

Sneddon, A. I. (1951). *Fourier Transforms*. McGraw-Hill.

Spangenberg, E. (1998). A fractal model for physical properties of porous rock: Theoretical formulations and application to elastic properties. *J. Geoph. Res.*, 103 (B6), pp. 12269–12289.

Taner, M. T., Koehler, F. and Sheriff, R. E. (1979). Complex seismic trace analysis. *Geophysics*, 44, pp. 1041–1063.

Van Deen, J. K., Greeuw, G., Van den Hondel, R., Van Staveren, M. T., Hoefsloot, F. J. M. and Vanhout, B. (1999). Horizontal CPTs for reconnaissance before the TBM front. *Geotechnical Engineering for transportation infrastructure*, Barends et al., ed., pp. 2023–2030. Balkema.

Van Kessel, A. J., Schiphouwer, R. A. and Van Capelleveen, P. A. (1999). Toepassing van geotechnische database en 3D-grondmodel. *Geotechniek*, 3 (4), pp. 12–16.

Van Spaendonck, R. L. C. (2002). *Wavelet based volume attributes (preliminary title)*. Ph.D. thesis, Delft University of Technology.

Van Wijngaarden, A. J. and Berkhout, A. J. (1995). Constrained linear AVO inversion. *Eur. Ass. of Expl. Geoph., Extended Abstracts, E034*.

Van Wijngaarden, A. J. (1998). *Imaging and characterization of angle-dependent seismic reflection data*. Ph.D. thesis, Delft University of Technology.

Verhelst, F. J. P. C. M. G. (2000). *Integration of seismic data with well-log data*. Ph.D. thesis, Delft University of Technology.

Verschuur, D. J. (1991). *Surface-related multiple elimination: an inversion approach*. Ph.D. thesis, Delft University of Technology.

Voigt, W. (1910). *Lehrbuch der Kristallphysik*. Teubner-Verlag.

Wapenaar, C. P. A. (1999). Amplitude-variation-with-angle behavior of self-similar interfaces. *Geophysics*, 64, pp. 1928–1938.

Wapenaar, C. P. A. and Berkhout, A. J. (1989). *Elastic wave field extrapolation*. Elsevier Amsterdam.

Widess, M. B. (1973). How thin is a thin bed? *Geophysics*, 38, pp. 1176–1180. previously published in Proceedings of the Geophysical Society of Tulsa 1957-58.

Yoshida, H., Keserci, B., Casalino, D. D., Coskun, A., Ozturk, O. and Savranlar, A. (1998). Segmentation of liver tumors in ultrasound images based on scale-space analysis of the continuous wavelet transform. *Proceedings of the IEEE Ultrasonics symposium*, volume 2, pp. 1713–1716. IEEE.

Yu, H. S. (1994). State parameter from self-boring pressuremeter tests in sand. *J. Geotech. Eng.*, 120 (12), pp. 2118–2135.

Yu, H. S. (1998). CASM: a unified state parameter model for clay and sand. *Int. J. Num. Anal. Geomech.*, 22, pp. 621–653.

Yu, H. S. (2000). *Cavity expansion methods in geomechanics*. Kluwer Academic Publishers.

Ziolkowski, A. (1984). *Deconvolution*. D. Reidel Publishing Company, 1st edition.

Zoeppritz, K. (1919). Erdbebenwellen VIIIB, On the reflection and propagation of seismic waves. *Göttinger Nachrichten*, 1, pp. 66–84.

List of publications

Goudswaard, J.C.M. and Wapenaar, C.P.A., 1997, Resolving well log singularities from seismic data, SEG International Exposition and 67th Annual meeting, Expanded Abstracts, AVO 1.3

Goudswaard, J.C.M. and Wapenaar, C.P.A., 1998, Characterization of reflectors by multi-scale amplitude and phase analysis of seismic data, SEG International Exposition and 68th Annual meeting, Expanded Abstracts, ST 9.3

Goudswaard, J.C.M., 1999, Multi-scale characterization of seismic reflection data, 61st EAGE Conference and Technical Exhibition, Helsinki, Extended Abstracts, 4-56

Goudswaard, J.C.M., Dillen, M.W.P. and Wapenaar, C.P.A., 2000, Multiangle processing and multiscale characterization of walkaway VSP data, SEG International Exposition and 70th Annual Meeting, Expanded Abstracts, pp. 178-181

Goudswaard, J.C.M. and Wapenaar, C.P.A., Scale and angle dependent reflection properties of self-similar interfaces, Journal of Computational Acoustics, accepted

Goudswaard, J.C.M. and Dillen, M.W.P., Imaging and multi-scale characterization of walk-away VSP data, Journal of Seismic Exploration, accepted

Goudswaard, J.C.M. and Ghose, R., Multi-scale analysis detecting lateral variation of soil strength from S-wave reflection data, Geophysics, submitted

Wapenaar, C.P.A., Van Geloven, W.J.F., *Goudswaard, J.C.M.*, Van Wijngaarden, A.J. and Dessing, F.J. AVA migration and multiscale characterization in finely layered media, 1997, Journal of Seismic Exploration **6**, pp. 181-198

Van Geloven, W.J.F., Wapenaar, C.P.A. and *Goudswaard, J.C.M.*, 1997, Improved AVA imaging and characterization in complex media: Karlsruhe Workshop on amplitude preserving seismic reflection imaging.

Wapenaar, C.P.A., Van Geloven, W.J.F., and *Goudswaard, J.C.M.*, 1997, Modelling, imaging and characterization of self-similar interfaces, 59th EAGE Conference and Technical Exhibition, Extended Abstracts E017

Wapenaar, C.P.A., *Goudswaard, J.C.M.*, Van Geloven, W.J.F. and Fokkema, J.T., 1997, Multi-scale analysis of well-logs and of seismic reflection data, 5th International Meeting of the Brazilian Geophysical Society, Expanded Abstracts

Wapenaar, C.P.A., *Goudswaard, J.C.M.* and Van Wijngaarden, A.J., 1999, Multiangle, multiscale inversion of migrated seismic data, The Leading Edge, Volume 18, No. 8, pp. 928 – 945

Wapenaar, C.P.A. and *Goudswaard, J.C.M.*, 1999, Reflection and transmission coefficients of self-similar interfaces., ICTCA '99 Fourth International Conference on Theoretical and Computational Acoustics, Proceedings

Ghose, R. and *Goudswaard, J.C.M.*, 2000, Relating shallow, S-wave seismic to cone penetration testing (CPT) in soft soil: a multi-angle, multi-scale approach, SEG International Exposition and 70th Annual Meeting, Expanded Abstracts, pp. 1331-1334

Ghose, R. and *Goudswaard, J.C.M.*, 2000, Shear modulus versus strength: a multi-angle, multi-scale approach to relate shallow, s-wave seismic to cone penetration testing, EEGS Bochum, Proceedings, nr. EG03

Dillen, M.W.P., Wapenaar, C.P.A. and Goudswaard, J.C.M., 2001, Generalised primary propagator estimation from walk-away VSP, Karlsruhe workshop on seismic true amplitude reflections, Proceedings

Ghose, R. and *Goudswaard, J.C.M.*, 2001, Multiscale analysis revealing the lateral variation of soil strength from S-wave reflection data, EAGE Conference and Technical Exhibition, Extended Abstracts N-028

Ghose, R. and *Goudswaard, J.C.M.*, 2001, Detecting laterally varying soil strength from the scaling behaviour of shear wave velocity changes, EEGS Birmingham, Proceedings, nr. EGSI04

Ghose, R. and *Goudswaard, J.C.M.*, Integrating S-wave seismic reflection data and CPT using a multi-angle, multi-scale approach, Geophysics, submitted

Samenvatting

Hoek- en schaalafhankelijke karakterisering van seismische reflectiemetingen

Het is bekend dat boorgatmetingen van de golfvoortplantingssnelheden een multi-fractaal, ofwel lokaal zelfgelijkend, gedrag vertonen over een groot schaalbereik. Dit gedrag wordt gekarakterizeerd door een singulariteitsparameter, die de lokale fractale dimensie van een boorgatmeting kwantificeert. Dit proefschrift behandelt methodieken om dit lokaal zelfgelijkende gedrag van deze boorgatmetingen te schatten uit seismische reflektiemetingen.

In Hoofdstuk 2 wordt een overzicht van gangbare transformaties van seismische reflectiemetingen gegeven. Het gebruik van de continue wavelet transformatie in de schaalanalyse van boorgatmetingen van de golfvoortplantingssnelheid wordt behandeld. Om consistent met dit multifractaal gedrag van deze boorgatmetingen te zijn wordt een snelheidsfunctie geïntroduceerd, die een generalizatie is van een Zoeppritz grensvlak naar een zelfgelijkende representatie.

Hoofdstuk 3 behandelt een impliciete relatie voor de straalparameterafhankelijke reflectiviteit van de zelfgelijkende snelheidsfuncties van Hoofdstuk 2. Synthetische seismische reflectiemetingen zijn gemodelleerd in snelheidsfuncties die zelfgelijkende reflectoren bevatten. Gebruik makend van deze impliciete relatie worden deze reflectiemetingen geïnverteerd voor de singulariteitsparameter.

De eerste methode is het analyseren van de contouren van constante reflectieamplitudes in modulus maxima vlakken. De toepassing van deze methode op metingen, gemodelleerd in zowel synthetische als echte boorgatmetingen van de voortplantingssnelheid, laat zien dat een schatting van de singulariteitsparameter gevonden kan worden, die consistent is met schattingen van deze parameter voor reflectoren in deze boorgatmetingen.

Verdere analyse van de reflectiecoëfficiënt voor de zelfgelijkende snelheidsfunctie geeft een expliciete uitdrukking voor de instantane fase van een

verticaal invallende gereflecteerde golf. Instantane fase en schaalafhankelijke amplitudes van een seismische reflectie worden gebruikt om te inverteren voor zowel een snelheidscontrast-ratio en de singulariteitsparameter.

Bovendien wordt aangetoond dat de instantane fase van een specifieke reflectie informatie bevat, complementair aan de schaalafhankelijke reflectieamplitudes. Dit kan worden gebruikt voor het schatten van de singulariteitsparameter en een snelheidscontrast-ratio van seismische reflectiemetingen. Een Gauss-Newton inversieschema wordt geïntroduceerd hetgeen het theoretisch mogelijk maakt om te inverteren voor deze parameters, gebruik makend van een kostfunctionaal gebaseerd op deze schaalafhankelijke amplitudes en instantane fases. Echter, de convergentiesnelheid van dit inversieschema is onvoldoende om een toepassing op echte seismiek mogelijk te maken.

In Hoofstuk 4 wordt een alternatieve methode voor hoek- en schaalafhankelijke analyse van zowel akoestische als elastische seismische reflectiemetingen voorgesteld. Deze methode bestaat uit twee stappen.

Als eerste voeren we een geLineariseerde Zoeppritz Inversie (LZI) op straalparameterafhankelijke reflectiviteitssecties uit, om snelheidscontrastfuncties, welke schattingen zijn van de golfvoortplantingssnelheidscontrasten op elke beeldvormingsdiepte, te verkrijgen. Een test op gemodelleerde metingen toont aan dat de snelheidscontrastfuncties, geschat uit de straalparameterafhankelijke reflectiviteitssecties, over het algemeen goede schattingen zijn van de daadwerkelijke snelheidscontrastfuncties.

De tweede stap is een schaalafhankelijke analyse van deze snelheidscontrastfuncties. Een techniek die lijkt op de techniek om de singulariteitsparameter te schatten uit boorgatmetingen wordt gebruikt om de singulariteitsparameter te schatten uit de snelheidscontrastfuncties. Deze methode is toegepast op zowel snelheidscontrastfuncties verkregen door middel van LZI als op snelheidscontrastfuncties die afgeleid zijn van de golfvoortplantingssnelheden. Het wordt aangetoond dat de schattingen van de singulariteitsparameter uit beide snelheidscontrastfuncties consistent met elkaar zijn. Hogere orde termen in de expliciete Zoeppritz vergelijkingen die niet meegenomen worden in de LZI en interne meervoudige reflecties zijn de voornaamste oorzaak van fouten binnen deze inversietechniek.

Hoofdstuk 5 is het eerste van twee hoofdstukken waarin de methode voor schaalafhankelijke analyse van snelheidscontrastfuncties wordt toegepast op echte metingen. Het hoofdstuk behandelt de toepassing van deze methode op VSP metingen met meervoudige bronposities, waarbij de bronnen aan het

oppervlak zijn gesitueerd en de ontvangers in een boorput.

Aangetoond wordt dat van golfvelden van deeltjessnelheden v_x en v_z, gemeten door de ontvangers in de boorput, de op- en neergaande P- en S-golfpotentialen kunnen worden geconstrueerd. Eerst wordt een decompositie in P- en S-golfpotentialen uitgevoerd door middel van een expliciet polarisatieschema, gevolgd door de scheiding in op- en neergaande golfvelden door middel van een mediaanfiltertechniek. De toepassing van deze techniek op gemodelleerde metingen toont aan dat dit tot een hoogwaardige decompositie leidt.

De opgaande golfveldpotentialen zijn de invoer van twee beeldvormingsschema's. Het eerste schema is een conventionele aanpak om diepteafbeeldingen van de straalparameterafhankelijke P-P en P-S reflectiviteiten voor iedere ontvangerdiepte te construeren. De tweede aanpak combineert de afbeeldingen van iedere ontvangerdiepte, waardoor stuksgewijs geconstrueerde diepteafbeeldingen worden verkrijgen, waarin zich minder interne meervoudige reflecties bevinden dan in de afbeeldingen van slechts één ontvanger. Tevens worden de amplitudes beter behouden in deze stuksgewijs geconstrueerde diepteafbeeldingen, omdat de upgaande transmissiepaden korter zijn.

De conventionele diepteafbeelding van de bovenste ontvanger en de stuksgewijs geconstrueerde diepteafbeelding, beide voor de P-P reflectiviteit worden geanalyseerd met de hoek- en schaalafhankelijke karakteriseringsmethode van Hoofdstuk 4. Hiervoor worden snelheidscontrastfuncties geschat uit beide afbeeldingen door LZI toe te passen. Ook van het P-golfsnelheidsprofiel wordt een snelheidscontrastfunctie geconstrueerd. Hierop volgend wordt de schaalafhankelijke analyse toegepast om singulariteitsparameterprofielen voor elk van deze snelheidscontrastfuncties te verkrijgen. Het wordt aangetoond dat het schaalafhankelijke gedrag van het P-golfsnelheidsprofiel kan worden teruggevonden uit nauwkeurig afgebeelde echte seismische reflectiemetingen, wat overeenkomt met de resultaten verkregen uit het toepassen van deze techniek op gemodelleerde metingen.

Door de schattingen van de singulariteitsparameter, verkregen uit de conventionele diepteafbeelding en de stuksgewijs geconstrueerde diepteafbeelding te vergelijken met die verkregen uit het P-golfsnelheidsprofiel, vinden we de beste correlatie voor de stuksgewijs geconstrueerde diepteafbeelding. Dit bevestigt dat de nieuwe beeldvormingstechniek een betere representatie van de straalparameterafhankelijke reflectiviteit geeft dan het conventionele schema.

In Hoofdstuk 6 wordt een toepassing op ondiepe S-golf seismiek gepresenteerd. In geotechnische toepassingen is Conus Penetratie Test (CPT) het meest gebruikte middel voor de karakterisering van grondlagen. Een poging wordt gedaan om ondiepe seismische reflectiemetingen te correleren met CPT conusweerstand. Hoewel CPT en seismische metingen de grondeigenschappen voor zeer verschillende schuifspanningsniveaus weergeven, wordt door vele auteurs gemeld dat CPT conusweerstand goed correleert met S-golf reflectiemetingen.

Dientengevolge stellen we voor om onze schaalafhankelijke analyse toe te passen als een techniek voor de integratie van S-golf reflectiemetingen en CPT conusweerstand. We schatten, voor sterke reflecties, de singulariteitsparameter verkregen uit snelheidscontrastfuncties van de S-golf reflectiemetingen en vergelijken deze met singulariteitsparameters die geschat zijn voor sterke veranderingen in de CPT conusweerstand.

Door deze methode toe te passen op de metingen van twee experimenten waarin zowel S-golf reflectieseismiek als CPT conusweerstand zijn gemeten, hebben we significante resultaten kunnen verkrijgen. Het eerste experiment is uitgevoerd op een lokatie waar laterale variaties in de ondergrond aanwezig waren. De toepassing van de schaalafhankelijke analyse op de seismische metingen geeft een goede indicatie van de laterale positie waar een specifieke grondlaag een veranderend schaalafhankelijk gedrag vertoont. Dit kan worden geïnterpreteerd als een verandering van grondsterkte langs een grondlaag.

Het tweede experiment betreft meervoudige CPT metingen langs een seismische lijn, zodanig dat de correlatie op verschillende laterale posities in de seismische lijn kan worden uitgevoerd. De laterale variatie van de fijnschalige karakteristieken van de S-golfsnelheidsdistributie correleert opmerkelijk goed met de laterale variatie in de CPT conusweerstand. Schaalafhankelijke analyse is dientengevolge een waardevolle toevoeging aan de bestaande geotechnische karakteriseringstechnieken.

Jeroen Goudswaard

Summary

Multiangle multiscale characterization of seismic reflection data

It has been found that well-logs of the local wave-velocities exhibit multifractal, or local self-similar, behavior of a wide range of scales. This behavior is characterized by a singularity parameter, that quantifies the local fractal dimension of a well-log. The thesis is focused on the recovery of this local self-similar behavior of well-logs from seismic reflection data.

In Chapter 2 an overview of the transformations that are commonly applied to seismic reflection data is given. The use of the continuous wavelet transformation is treated for multiscale analysis of well-log data. To be consistent with the local self-similar behavior of well-logs, a velocity function describing a reflector is introduced, that is a generalization of a Zoeppritz boundary to a self-similar interface.

Chapter 3 presents an implicit relation for the rayparameter-dependent reflectivity of the self-similar velocity functions from Chapter 2. Synthetic seismic reflection data are modeled in velocity functions, containing self-similar reflectors. Using the aforementioned implicit relation, these reflection data are inverted for the singularity parameter. The first method is by analyzing the contours of constant reflection amplitudes in modulus maxima planes. From the application of this method to synthetic data, modeled in both synthetic and real well-logs, it is shown that an estimate of the singularity parameter can be found that is consistent with the one derived from reflectors in these well-logs.

Further analysis of the reflection coefficient of the self-similar velocity function, gives an explicit expression for the instantaneous phase of a normal incident reflected wave. Instantaneous phase and scale dependent amplitudes of a seismic event are used to invert for both a velocity contrast ratio and the singularity parameter.

Furthermore, it is shown that the instantaneous phase of a specific reflection event contains information complimentary to the multiscale reflection

amplitudes. This can be used to resolve both the singularity parameter and a velocity contrast ratio from seismic reflection data. A Gauss-Newton inversion scheme is proposed that is theoretically able to solve for these parameters using a penalty function based on a combination of these multiscale amplitudes and instantaneous phases. However, the rate of convergence of this inversion scheme is not sufficient for applying it to field data.

Following, in Chapter 4, an alternative method for multiangle, multiscale analysis of both acoustic and elastic seismic reflection data is proposed. The method consists of two steps.

First, we perform a Linearized Zoeppritz Inversion (LZI) to imaged rayparameter-dependent reflectivity gathers, to acquire velocity contrast functions, which are estimates of the velocity contrasts at each imaging depth. A test on synthetic data shows that the velocity contrast functions derived from the rayparameter-dependent reflectivity gathers are generally good estimates of the actual velocity contrast functions.

The second step is a multiscale analysis of these velocity contrast functions. A technique, similar to the technique used to estimate the singularity parameter from well-logs, is used to estimate the parameter from velocity contrast functions. This method is applied to both the velocity contrast functions constructed by LZI and the velocity contrast functions derived directly from the velocity fields. It is shown that the estimates of singularity parameters derived from both velocity contrast functions give consistent results. Higher order terms in the explicit Zoeppritz equations that are not accounted for in LZI and internal multiples are the main causes of errors in this inversion.

Chapter 5 is the first of two chapters in which the method for multiscale analysis of velocity contrast functions is applied to real data sets. The chapter treats the application of the method to walk-away VSP data, in which the sources are located at the surface and the receivers in a borehole.

It is shown that from particle velocity wave fields v_x and v_z, measured by the receivers in the borehole, the up- and downgoing P- and S-wave potentials can be constructed. First a decomposition in P- and S-wave potentials is performed, by applying an explicit polarization scheme, followed by a separation into up- and downgoing fields, by means of a median filter technique. The application of this technique shows a high-quality decomposition, in which events of other modes are hardly visible.

The upgoing wave field potentials are the input of two imaging schemes. The first scheme is a conventional approach to construct depth images of the

rayparameter-dependent P-P and P-S reflectivity for every receiver depth. The second approach combines the images from each receiver depth, to construct piecewise depth images that contain less internal multiples than the images constructed from the data received by only one receiver. Furthermore, the amplitudes are better preserved in these piecewise constructed images, as the upgoing transmission paths are shorter.

The conventional depth image from the topmost receiver and the piecewise constructed image, both for the P-P reflectivity, are analyzed by the multiangle, multiscale characterization method of Chapter 4. To this end, velocity contrast functions are derived from both images, by applying LZI. Also from the P-wave velocity profile, a velocity contrast function is constructed. Following, the multiscale analysis is applied to construct singularity parameter profiles for each of these velocity contrast functions. It is shown that the multiscale behavior of the P-wave velocity profile can be recovered from the accurately imaged real seismic reflection data, in accordance with the results of applying this to synthetic data.

Further, by comparing the estimates of the singularity parameter derived from the conventional and the piecewise constructed image with the ones derived from the P-wave velocity profile, we find the best correlation for the piecewise constructed image. This confirms that the novel imaging scheme gives a better representation of the rayparameter-dependent reflectivity than the conventional scheme.

In Chapter 6 an application to shallow S-wave seismics is given. In geotechnical applications, the most used tool for soil characterization is the Cone Penetration Test (CPT). An attempt is made to correlate shallow seismic reflection data with CPT cone resistance. Though CPT and seismic data represent the soil properties for very different levels of strain, it has been reported by many authors that CPT cone resistance correlates well with S-wave reflection data.

Therefore, the multiscale analysis is proposed as a technique to integrate the S-wave reflection data with CPT cone resistance by applying this to both data types. We estimate, for strong reflections, the singularity parameter, derived from velocity contrast functions that are constructed from the S-wave reflection data, and compare this with singularity parameters estimated from sharp changes in CPT cone resistance.

From testing this approach on two extensive field data sets containing both S-wave seismic reflection and CPT data, some significant results could be obtained. The first data set under consideration was recorded at a site

where lateral variations of the subsoil are present. The application of multiscale analysis to the seismic data gives a good indication of the lateral position where a specific soil layer shows some changing multiscale behavior. This can be interpreted as a change in soil strength along a soil boundary.

The second data set contains multiple CPTs along the seismic line, such that the correlation can be tested at different lateral positions in the seismic section. The lateral variation of the fine-scale nature of the S-wave velocity distribution over an interface is found to correlate remarkably well with the lateral variation of the CPT cone resistance. Multiscale analysis is shown to be a valuable addition to the existing geotechnical characterization techniques.

Jeroen Goudswaard

Dankwoord

Hoewel dit proefschrift slechts één auteur heeft, hebben veel mensen bijgedragen tot de realizatie ervan, die ik graag wil bedanken voor hun medewerking.

Als eerste wil ik graag mijn dank uitspreken aan het adres van mijn promotoren Kees Wapenaar en Jacob Fokkema. Vooral Kees heeft zich gedurende de afgelopen vijf jaar bijzonder hard ingespannen om mij te allen tijde gemotiveerd te houden voor het onderzoek, door mij te steunen zowel op het onderzoeks- als het persoonlijke vlak. Jacob ben ik voornamelijk dankbaar voor zijn aanbod om de laatste tweeëneenhalf jaar op het gebouw van Technische Aardwetenschappen voor mij plaats te maken.

Op het onderzoeksvlak ben ik tevens veel dank verschuldigd aan Menno Dillen, zonder wie Hoofdstuk 5 niet had kunnen worden geschreven en aan Ranajit Ghose, met wie ik de afgelopen anderhalf jaar een goede persoonlijke en bijzonder vruchtbare wetenschappelijke relatie heb opgebouwd. Samen met Eric Verschuur is hij de pijler achter het onderzoek beschreven in Hoofdstuk 6. Hierbij moet de medewerking van Rotterdam Gemeentewerken voor het beschikbaar stellen van de data in Hoofdstuk 6 en OYO CAG BV, met name Jan Brouwer, niet ongenoemd blijven.

Het onderzoek is gesteund door de leden van de STW gebruikerscommissie die elk half jaar weer nieuwe ideeën hebben aangedragen voor verder onderzoek.

Verder heb ik altijd veel plezier gehad met mijn kamergenoten door de jaren heen: Karin Schalkwijk, Ewoud van Dedem, Johan Vos, Remco Romijn, Ruud Prein, Arthur Denneman, Sevgi Tiğrek, Michiel van Kempen, Rob Hegge, Jan van der Kruk en Gerrit Toxopeüs. Met verontschuldigingen voor mijn uitgebreide en hoogstwaarschijnlijk niet altijd relevante discussies die ik altijd aanzwengelde.

Tevens heb ik goede herinneringen aan het samenwerken met Alexander Koek, die mij onder andere de basis van mijn huidige UNIX kennis heeft gege-

ven en met Wim van Geloven, Aart-Jan van Wijngaarden en Frank Dessing, zonder wie het onderzoek duidelijk minder voorspoedig zou zijn verlopen. Als laatste onder deze noemer bedank ik Guy Drijkoningen, voor zijn altijd aanwezige enthousiasme voor onderzoek en vooral veldwerk.

Ook wil ik graag mijn buurtjes in Rotterdam bedanken. Vooral Renske, waarmee ik jarenlang een goede band heb gehad zal ik gaan missen, maar natuurlijk ook Michiel met zijn bijzonder goede drankenkast, die ik ook graag voor zijn hulp met het ontwerp van de kaft en zijn bereidwilligheid om op te treden als paranimf, wil bedanken. Verder Nicole en Martine die altijd klaar stonden met lekkere hapjes en open voor een goed gesprek. En als laatste Aart, die belangrijk is geweest als rustpunt voor dit buurtje en als intermediair voor mijn sociaal leven in Rotterdam. In één adem met de buurtjes noem ik dan ook Jannie, die mij in de Big Snack vaak en met goed eten in leven heeft weten te houden. Ik denk dat de Bergpolderstraat altijd een apart plaatsje in mijn hart zal blijven houden.

Ik eindig graag met mijn familie. Als eerste bedank ik Kees-Jan, omdat hij zijn ruim vijf jaar langere levenservaring altijd met mij heeft willen delen en als paranimf heeft willen optreden. Verder natuurlijk ook Cleo die, door haar eigenwijze gedrag, mij vooral in de laatste paar weken van het schrijven van dit proefschrift de broodnodige afleiding heeft gegeven. Als laatste wil ik graag mijn ouders Jan en Heleen bedanken voor het mij motiveren om altijd het beste uit mezelf te halen. Niet voor niets is dit boekje aan jullie opgedragen. Ik hoop nog lang bij jullie langs te kunnen komen.

About the author

Jeroen Christiaan Martijn Goudswaard was born in Utrecht, The Netherlands, on June 21, 1973. From 1985 to 1991 he attended secondary school (VWO) at the "Christelijke Scholengemeenschap Walcheren" in Middelburg, The Netherlands. In September 1991, he started his university studies in Geophysics at the University of Utrecht, Faculty of Earth Sciences. For his MSc thesis, he carried out research in the field of crosswell traveltime tomography. This was done during a nine-months stage at what is currently known as Shell E&P Technology and Applications Research in Rijswijk. He was supervised by prof dr R.K. Snieder from the University of Utrecht and drs A.R. Verdel and dr A.P.H. ten Kroode from SEPTAR. On October 24, 1996 he graduated from Utrecht University. On October 1, 1996 he has started a PhD research on transmission and reflection properties of self-similar interfaces under the supervision of prof. dr. ir. C.P.A. Wapenaar from the Faculty of Applied Physics of Delft University of Technology. This research led to the present PhD thesis.